Performancestudie von Transitionsmodellen mit den CFD Codes LINARS und TRACE

Performance Study of Transition Models with LINARS and TRACE CFD Codes

Roland Burgstaller
Diplomarbeit

Ao. Univ.-Prof. Dipl.-Ing. Dr.techn. Wolfgang Sanz
Dipl.-Ing. (FH) Maria Elisabeth Kelterer
Betreuer

Technische Universität Graz

Institut für Thermische Turbomaschinen
Univ.-Prof. Dipl.-Ing. Dr.techn. Franz Heitmeir
Vorstand

Graz, am 1.10.2010

Mache die Dinge so einfach wie möglich - aber nicht einfacher.
Albert Einstein

Abstract

The accurate simulation of the flow through a turbomachine often depends on the correct prediction of boundary layer transition. The development of a transition model that is compatible with modern general purpose CFD codes has led to the correlation based $\gamma - Re_\theta$ transition model. It is strictly based on local variables and relies on empiric correlations. In this work, correlations found by different authors (Menter, Langtry, Malan and Kelterer) are used and compared against each other.

Two CFD codes are used to validate the correlations. The LINARS (inhouse code of the Institute for Thermal Turbomachinery and Machine Dynamics of Graz University of Technology) and TRACE (developed by DLR and MTU) codes are Reynolds-averaged Navier-Stokes solvers. While LINARS uses the $k - \omega$ and SST turbulence models, TRACE only uses the $k - \omega$ turbulence model.

The correlations were tested on three flat plate test cases (ERCOFTAC test cases T3A, T3C2 and T3C4) and two cascade test cases (T160 and T106). All correlations performed well for the T3A and T3C4 flat plate test cases, only the DLR correlation (Menter correlation to predict the start of transition, Malan correlations to control the start of the intermittency production and the length of the transition zone) produced a too long separation bubble in the T3C4 test case. On the other hand, only the Kelterer correlation (Menter correlation to predict the start of transition, Kelterer correlations to control the start of the intermittency production and the length of the transition zone) achieved good results for the T3C2 test case. For the cascade test cases, the Kelterer correlation produced a too short separation bubble. The Malan correlation (Langtry correlation for start of transition, Malan correlations for start of the intermittency production and the length of the transition zone) and the DLR correlation are able to predict a long separation bubble similar to the experiments. Both correlations are very sensitive to inlet turbulent boundary conditions (Malan more than DLR correlation).

Since no correlation yielded sufficiently accurate results for a wide range of test cases, further developments and refinements of the correlations and perhaps even the $\gamma - Re_\theta$ model itself are recommended.

Zusammenfassung

Die genaue numerische Simulation der Strömungen in einer Turbomaschine bedarf oft der korrekten Modellierung des laminar-turbulenten Umschlags in der Grenzschicht. Die Entwicklung eines Transitionsmodells, welches den Standards moderner CFD Codes genügt und ausschließlich lokale Variablen verwendet, brachte das auf empirischen Korrelationen beruhende $\gamma - Re_\theta$ Transitionsmodell hervor. Es beruht auf empirisch ermittelten Korrelationen, welche die physikalischen Vorgänge abbilden. In dieser Arbeit werden Korrelationen von verschiedenen Autoren verwendet (Menter, Langtry, Malan und Kelterer).
Zur Validierung der Korrelationen wurden die RANS-CFD-Codes LINARS (Inhouse CFD Code des Instituts für Thermische Turbomaschinen an der Technischen Universität Graz) und TRACE (entwickelt von DLR und MTU) verwendet. TRACE verwendet das $k - \omega$ Turbulenzmodell, LINARS enthält zusätzlich noch das SST-Turbulenzmodell.
Die Korrelationen wurden anhand drei ebener Plattentestfälle (ERCOFTAC-Testfälle T3A, T3C2 und T3C4) und zwei Kaskadentestfällen (T160 und T106) evaluiert. Für die ebenen Plattentestfälle T3A und T3C4 liefern alle Korrelationen zufriedenstellende Ergebnisse, lediglich die DLR Korrelation (Menter Korrelation zur Bestimmung des Transitionsbeginns, Malan Korrelationen zur Berechnung des Produktionsbeginns der Intermittenz und der Transitionslänge) liefert für den T3C4 Testfall eine zu lange Ablöseblase. Für den T3C2 Testfall brachte nur die Kelterer Korrelation (Menter Korrelation zur Bestimmung des Transitionsbeginns, Kelterer Korrelationen zur Berechnung des Produktionsbeginns der Intermittenz und der Transitionslänge) befriedigende Ergebnisse. Für die Kaskadentestfälle berechnet die Kelterer Korrelation eine zu kurze Ablöseblase. Die Malan Korrelation (Langtry Korrelation zur Bestimmung des Transitionsbeginns, Malan Korrelationen zur Berechnung des Produktionsbeginns der Intermittenz und der Transitionslänge) und DLR Korrelation erlauben durch entsprechende Wahl der Randbedingungen die Vorhersage einer langen Ablöseblase entsprechend der Messung. Es zeigt sich, dass beide Korrelationen sehr sensibel auf Änderungen der turbulenten Eintrittsrandbedingungen reagieren, wobei die Malan Korrelation sensibler ist als die DLR Korrelation.
Mit keiner Korrelation gelang es, zufriedenstellende Ergebnisse für alle Testfälle zu erzielen. Somit zeigt diese Arbeit die Notwendigkeit einer Weiterentwicklung und Verfeinerung der bestehenden Korrelationen und eventuell des $\gamma - Re_\theta$ Transitionsmodells selbst.

EIDESSTATTLICHE ERKLÄRUNG

Ich erkläre an Eides statt, dass ich die vorliegende Arbeit selbstständig verfasst, andere als die angegebenen Quellen/Hilfsmittel nicht benutzt, und die den benutzten Quellen wörtlich und inhaltlich entnommenen Stellen als solche kenntlich gemacht habe.

Graz, am ....

(Unterschrift)

Danksagung

Die vorliegende Diplomarbeit wurde im Studienjahr 2009/2010 am Institut für Thermische Turbomaschinen und Maschinendynamik an der Technischen Universität Graz verfasst.

Mein besonderer Dank gilt meinen Betreuern, Herrn Professor DI. Dr.techn. Wolfgang Sanz und Frau DI. (FH) Maria Elisabeth Kelterer, die mir die Arbeit an einem interessanten Themengebiet ermöglichten und mir in zahlreichen Diskussionen in einer sehr angenehmen Atmosphäre stets neue Denkanstöße für meine Arbeit gaben.

Ganz herzlich danke ich meinen Eltern, ohne deren Unterstützung ein Studium nicht möglich gewesen wäre und die mir grenzenloses Vertrauen in dieser Zeit entgegengebracht haben.

Schließlich danke ich allen Freunden und Studienkollegen, die mein Studium in Graz und Göteborg zu einer schönen, unvergesslichen Zeit gemacht haben und allen Freunden in meiner Heimat, die großes Verständnis für meine oft wochenlange Abwesenheit aufbrachten. Möge unser zukünftiger Lebensweg uns noch oft zusammenführen!

Roland Burgstaller

Contents

List of Figures

List of Tables

Nomenclature

c_f skin friction coefficient, $\frac{2\tau_W}{\rho U_\infty^2}$

c_p pressure coefficient, $\frac{p_{wall}-p_2}{p_{tot\infty}-p_2}$

F_{length} parameter that controls length of transition

F_{onset} parameter that controls start of transition

H shape factor

I intermittency function

K flow acceleration parameter, $(\nu/U^2)dU/dx$

l_m turbulence length scale, mixing length, $l_m \propto \frac{k^{1/2}}{\omega}$

$n\hat{\sigma}$ dimensionless turbulent sport production rate

p pressure

$R\tilde{e}_{\theta t}$ local transition onset momentum thickness Reynolds number (obtained from a transport equation)

Re_θ momentum thickness Reynolds number, $\frac{\rho\theta U_0}{\mu}$

Re_L Reynolds number, $\frac{U_\infty L\rho}{\mu}$

Re_x local Reynolds number, $\frac{xU\rho}{\mu}$

$Re_{\theta c}$ critical momentum thickness Reynolds number where intermittency first starts to increase

$Re_{\theta E}$ momentum thickness Reynolds number where transition ends (Abu-Ghannam and Shaw [1980] algebraic transition model)

$Re_{\theta S}$ momentum thickness Reynolds number where transition starts (Abu-Ghannam and Shaw [1980] algebraic transition model)

$Re_{\theta t}$ transition onset momentum thickness Reynolds number (obtained from empiric correlations) where c_f first starts to increase

Re_v vorticity Reynolds number, $\frac{\rho y^2}{\mu}\Omega$

S Sutherland temperature

t time

Tu turbulent intensity, $\frac{\sqrt{\frac{2}{3}k}}{U_\infty} \cdot 100$ [%]

Tu_∞ reference turbulence intensity at inlet

U velocity

u', v', w' fluctuating velocities in x, y, z direction

U, V, W mean velocities in x, y, z direction

U_0 local free stream velocity

U_∞ inlet reference velocity

u_τ friction velocity, $\sqrt{\frac{\tau_{wall}}{\rho}}$

Greek symbols

ϵ turbulent dissipation rate

γ near wall intermittency factor

λ_θ pressure gradient parameter, $(\theta^2/\nu)dU/dx$

μ molecular viscosity

μ_t turbulent viscosity

ν kinematic viscosity

Ω absolute value of vorticity, $(2\Omega_{ij}\Omega_{ij})^{1/2}$

ω turbulent frequency, $\frac{\epsilon}{k}$

Ω_{ij} vorticity tensor, $0.5\left(\frac{\partial u_i}{\partial x_j} - \frac{\partial u_j}{\partial x_i}\right)$

ρ density

τ_{ij} Reynolds stresses

θ momentum thickness

ζ	total pressure loss coefficient
ζ_l	local pressure loss coefficient

Abbreviations

APG	adverse pressure gradient
DNS	direct numerical simulation
FPG	favorable pressure gradient
LGS	Line Gauß-Seidel
$RANS$	Reynolds-averaged Navier-Stokes equations
$S\&K$	Schubauer and Klebanoff test case
$SSOR$	Symmetric Successive Over Relaxation
ZPG	zero pressure gradient

Subscripts

2	parameter at measurement layer, defined by test case
∞	reference property at inlet
c	critical point
ref	reference property
t	transition onset
tot	total

1 Introduction

Thermal turbomachines play a mayor role in energy production. Increasing their efficiency leads to a tremendous reduction of costs and also carbon dioxide emissions, for these reasons it has been a major engineering challenge for decades. For an engineer working in this field, it is essential to know about the flow features of a machine, which are traditionally obtained from experiments. This is expensive and takes a great deal of time and as computational power has become cheaper over the last few decades, it seemed reasonable to use computer simulations to perform optimization tasks more quickly and cheaply.
Whereas, in the past, a significant amount of progress has been made in the development of reliable turbulence models to simulate a wide range of fully turbulent flows, the crucial effects of laminar-turbulent transition still can not be captured due to the absence of transition models. There are a number of reasons for this circumstance. First, there are several modes of transition which lack a mathematical description. The first transition models were limited to specific geometries and contained numerous nonlocal operations that are difficult to implement into a modern Computational Fluid Dynamics (CFD) environment. Another complication arises from the fact that most CFD codes are based on Reynolds averaged Navier-Stokes (RANS) equations. The averaging process eliminates the effects of linear disturbance growth and is therefore difficult to apply to the transition process. Menter et al. [2004] formulated the $\gamma - Re_\theta$ transition model that only uses local variables. It can be implemented into a general RANS environment. Due to proprietary reasons some correlations, which were required by this model, were published later. Since then the scientific community has developed their own correlations.
In this work two different CFD codes are tested against each other, the LINARS and TRACE CFD code, in test cases, where different modes of transition occur. TRACE and LINARS use the same transition model, the $\gamma - Re_\theta$ transition model. Unlike TRACE, LINARS has implemented different correlations for the transition model, which are also compared against each other, to point out their strengths and weaknesses.
In the first part of this work some basic concepts of flow modelling and the need for turbulence models are discussed, followed by a brief introduction to two commonly used turbulence models, the Wilcox $k - \omega$ model and the Menter SST model, which are used in the calculation of the test cases. Then an introduction to the $\gamma - Re_\theta$ transition model is given, where the different correlations are discussed.
The main part of this work was to carry out the simulations on the test cases. Five different

test cases, three flat plate (T3A, T3C2, T3C4) and two cascade test cases (T160, T106) are used to validate the TRACE and LINARS code. Their results are compared with experimental data. Both codes run on a LINUX workstation. They produce data that can be imported to Tecplot and converted to ASCII data files. MatLab is then used to evaluate and visualize the data.

2 Introduction to Flow and Turbulence Modelling

In Computational Fluid Dynamics (CFD), there are three key elements:

- Grid Generation
- Algorithm Development
- Turbulence Modelling

Whereas for grid generation and algorithm development very precise mathematical theories have evolved, turbulence models are still unable to accomplish acceptable accuracy for a wide range of problems. Since most flow problems of practical engineering interest are turbulent, this leaves us in a less than satisfactory situation. The root of the problem lies in its complexity.
If the Reynolds number, i.e. the ratio of inertia forces to viscous forces, of a flow exceeds a certain threshold, it becomes turbulent. Thus the velocity and other flow properties vary rapidly in a random and chaotic way. Even with constant imposed boundary conditions, the motion of a turbulent flow becomes intrinsically unsteady. These instabilities are a result of the interaction between nonlinear inertial terms and viscous terms in the Navier-Stokes equations (see equation 2.2).
In principle, the time dependent, three dimensional Navier-Stokes equations contain all of the physics of a given turbulent flow. For an incompressible flow, the instantaneous continuity (2.1) and Navier-Stokes (2.2) equations

$$\text{div } \mathbf{u} = 0 \tag{2.1}$$

$$\frac{\partial u}{\partial t} + \operatorname{div}(u\mathbf{u}) = -\frac{1}{\rho}\frac{\partial p}{\partial x} + \nu \operatorname{div}(\operatorname{grad}(u)) \tag{2.2a}$$

$$\frac{\partial v}{\partial t} + \operatorname{div}(v\mathbf{u}) = -\frac{1}{\rho}\frac{\partial p}{\partial x} + \nu \operatorname{div}(\operatorname{grad}(v)) \tag{2.2b}$$

$$\underbrace{\underbrace{\underbrace{\frac{\partial w}{\partial t}}_{\substack{\text{Unsteady}\\ \text{acceleration}}} + \underbrace{\operatorname{div}(w\mathbf{u})}_{\substack{\text{Convective}\\ \text{acceleration}}}}_{\text{Inertial terms}}}_{} = \underbrace{-\frac{1}{\rho}\frac{\partial p}{\partial x}}_{\substack{\text{Pressure}\\ \text{gradient}}} + \underbrace{\nu \operatorname{div}(\operatorname{grad}(w))}_{\text{Viscosity}} \tag{2.2c}$$

form a closed set of four equations, with four unknown u, v, w and p. This can be solved using DNS (Direct Numerical Simulation), which is considered to be the most accurate method for a flow simulation, since no assumptions are made in the continuity and Navier-Stokes equations.

The drawback, however, is that the grid size for a DNS simulation must be sufficiently small, to resolve turbulent eddies even at their smallest scale, the Kolmogorov scale, where turbulent energy dissipates to heat. To meet the requirements of an accurate numerical simulation, a DNS simulation must be fully time dependent and three dimensional, all physically relevant scales must be resolved.

Due to these conditions, DNS simulations are not only the most accurate, but also the most resource-intensive simulations and thus only a few problems have been solved with DNS to date.

This dilemma leads us to the development of turbulence modelling, where additional equations are used to calculate turbulence properties.

2.1 Reynolds Decomposition

From an engineering point of view, it is not necessarily required to know every single detail of turbulent fluctuations. Users are generally satisfied with information on the mean properties of the flow. This basic premise leads to the classical turbulence models approach, wherein an instantaneous flow property is decomposed into a time-averaged mean value and a fluctuating component. Figure 2.1 illustrates a typical point velocity measurement in a turbulent flow and shows its mean and fluctuating velocity.

This leads to the Reynolds decomposition

$$u(t) = U + u'(t) \tag{2.3}$$

where U is the steady mean velocity and u' is the statistical property of its fluctuation.

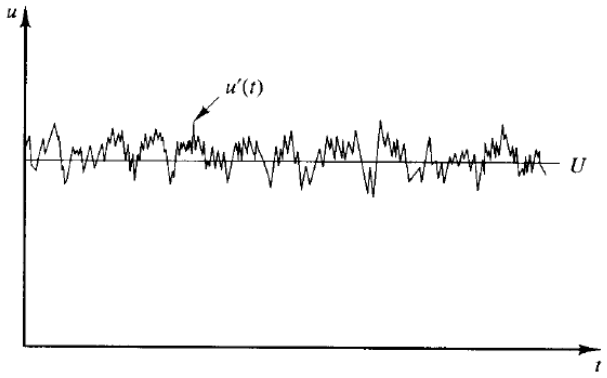

Figure 2.1: Typical point velocity measurement in turbulent flow [Versteeg and Malalasekra, 2007]

The same procedure can be applied to decompose the instantaneous pressure:

$$p(t) = P + p'(t) \tag{2.4}$$

Using vector notation, equation 2.3 can be written as:

$$\mathbf{u}(t) = \mathbf{U} + \mathbf{u}'(t) \tag{2.5}$$

2.2 Reynolds-Averaged Navier-Stokes Equations and Classical Turbulence Models

We can investigate the effects of turbulent fluctuations on the mean flow by replacing the variables $\mathbf{u}$ (hence u, v, w) and p in the continuity (2.1) and Navier-Stokes (2.2) equations using Reynolds decomposition and taking the time average [Versteeg and Malalasekra, 2007, pg. 63].
This yields the continuity equation for the mean flow

$$\mathrm{div}\mathbf{U} = 0 \tag{2.6}$$

and the time averaged Navier-Stokes equations:

$$\frac{\partial U}{\partial t} + \mathrm{div}(U\mathbf{U}) = -\frac{1}{\rho}\frac{\partial P}{\partial x} + \nu\,\mathrm{div}(\mathrm{grad}(U)) + \frac{1}{\rho}\left[\frac{\partial(-\rho\,\overline{u'^2})}{\partial x} + \frac{\partial(-\rho\,\overline{u'v'})}{\partial y} + \frac{\partial(-\rho\,\overline{u'w'})}{\partial z}\right] \tag{2.7a}$$

$$\frac{\partial V}{\partial t} + \mathrm{div}(V\mathbf{U}) = -\frac{1}{\rho}\frac{\partial P}{\partial y} + \nu\,\mathrm{div}(\mathrm{grad}(V)) + \frac{1}{\rho}\left[\frac{\partial(-\rho\,\overline{u'v'})}{\partial x} + \frac{\partial(-\rho\,\overline{v'^2})}{\partial y} + \frac{\partial(-\rho\,\overline{v'w'})}{\partial z}\right] \tag{2.7b}$$

$$\frac{\partial W}{\partial t} + \mathrm{div}(W\mathbf{U}) = -\frac{1}{\rho}\frac{\partial P}{\partial z} + \nu\,\mathrm{div}(\mathrm{grad}(W)) + \frac{1}{\rho}\left[\frac{\partial(-\rho\,\overline{u'w'})}{\partial x} + \frac{\partial(-\rho\,\overline{v'w'})}{\partial y} + \frac{\partial(-\rho\,\overline{w'^2})}{\partial z}\right] \tag{2.7c}$$

This set of equations is called the Reynolds-averaged Navier-Stokes equations (RANS).

The extra stresses that appear on the right hand side are what are known as Reynolds stresses, they can be distinguished into normal stresses

$$\tau_{xx} = -\rho\,\overline{u'^2} \qquad \tau_{yy} = -\rho\,\overline{v'^2} \qquad \tau_{zz} = -\rho\,\overline{w'^2} \tag{2.8a}$$

and shear stresses

$$\tau_{xy} = \tau_{yx} = -\rho\,\overline{u'v'} \qquad \tau_{xz} = \tau_{zx} = -\rho\,\overline{u'w'} \qquad \tau_{yz} = \tau_{zy} = -\rho\,\overline{v'w'} \tag{2.8b}$$

While the time averaged fluctuating velocity becomes zero $\overline{\mathbf{u}'} = 0$, the Reynolds stresses are always non-zero due to the structure of vortical eddies. In turbulent flows they are usually very large compared to viscous stresses.
Wilcox [2006, pg.16] states, that herein lies the fundamental problem of turbulence for the engineer, because before computing the mean flow properties, a prescription of $\overline{u'v'}$ is needed.
As yet, we have obtained no additional equations for the incompressible three-dimensional flow. Instead, we found four unknown mean flow properties (pressure P and mean velocity $\mathbf{U}$, hence U, V, W) and six additional Reynolds stress components, which leaves us with four equations and ten unknowns. This system is yet unclosed. In order to solve it, we must find additional equations.

The Closure Problem

To obtain additional equations one can take moments of the Navier-Stokes equation [Wilcox, 2006, pg. 17], leading to what is known as the Reynolds-Stress Equation that produces six additional equations but results in 22 additional independent unknowns. This illustrates the closure problem. Additional unknowns are generated at every level, as higher and higher moments are taken due to the nonlinearity of the Navier-Stokes equations. This shows the need to develop approximations for the unknown correlations so that a sufficient number of equations exist.

Additional Transport Equations

The turbulence models are normally classified by the number of additional transport equations that must be solved along with the RANS flow equations. These additional transport equations are derived from the general transport equation. The time-averaged transport equation for any scalar $\varphi = \Phi + \varphi'$ reads as

$$\frac{\partial \Phi}{\partial t} + \operatorname{div}(\Phi \mathbf{U}) = \frac{1}{\rho}\operatorname{div}(\Gamma_\Phi \operatorname{grad}\Phi) + \left[-\frac{\partial\,\overline{u'\varphi'}}{\partial x} - \frac{\partial\,\overline{v'\varphi'}}{\partial y} - \frac{\partial\,\overline{w'\varphi'}}{\partial z}\right] + S_\Phi \tag{2.9}$$

Table 2.1 lists common RANS models. The computational effort rises with the number of additional transport equations to be solved. So the Reynolds stress model is the most expensive, while the Spalart-Allmaras model is very simple, stable and still useful.

No. of extra transport equations	Name
Zero	Mixing length model
One	Spalart-Allmaras model
Two	k-ϵ model
	k-ω model
	Menter SST model
Seven	Reynolds stress model

Table 2.1: Overview of RANS models

Eddy Viscosity

Zero-, One- and Two-Equation Models retain the Boussinesq assumption, which introduces the concept of an eddy viscosity. It is based on the assumption that there is an analogy between the action of viscous stresses and Reynold stresses on the mean flow (see equation 2.10). It proposes the introduction of a virtual viscosity, the eddy viscosity or turbulent viscosity μ_t, which accounts for the effects of turbulence on the flow. The main effect of turbulence is to cause the fluid to move normal to the main flow direction. However, this transports momentum from one layer to another, causing the other layers to decelerate or to accelerate.

$$\tau_{ij} = -\rho\overline{u_i' u_j'} = \mu_t \left(\frac{\partial U_i}{\partial x_j} + \frac{\partial U_j}{\partial x_i} \right) \tag{2.10}$$

The treatment of the turbulent viscosity is one major difference of the turbulence models.

2.2.1 Wilcox $k - \omega$ Turbulence Model

Whereas the one-equation models are incomplete due to the fact that they relate the turbulence length scale to typical flow dimensions, the two-equation models provide an additional equation for the turbulence length scale and are therefore complete [Wilcox, 2006, pg. 73]. The Wilcox $k - \omega$ turbulence model uses two additional transport equations, one for the kinematic energy k and one for the turbulence frequency $\omega = \frac{\epsilon}{k}$.
The eddy viscosity is given as:

$$\mu_t = \frac{\rho k}{\omega} \tag{2.11}$$

The Reynolds stresses are computed using the Boussinesq assumption (see equation 2.10).

The transport equation for the turbulence kinetic energy reads as:

$$\underbrace{\frac{\partial}{\partial t}(\rho k)}_{\substack{\text{Rate of change}\\ \text{in time}}} + \underbrace{\operatorname{div}(\rho k \mathbf{U})}_{\substack{\text{Transport}\\ \text{by convection}}} = \underbrace{\operatorname{div}\left[\left(\mu + \frac{\mu_t}{\sigma_k}\right) grad(k)\right]}_{\substack{\text{Transport by}\\ \text{turbulent diffusion}}} + \underbrace{P_k}_{\substack{\text{Rate of}\\ \text{production}}} - \underbrace{\beta_k \rho k \omega}_{\substack{\text{Rate of}\\ \text{dissipation}}} \tag{2.12}$$

The transport equation for the specific dissipation rate is as follows:

$$\frac{\partial}{\partial t}(\rho\omega) + \operatorname{div}(\rho\omega\mathbf{U}) = \operatorname{div}\left[\left(\mu + \frac{\mu_t}{\sigma_\omega}\right) grad(\omega)\right] + P_\omega - \beta_\omega \rho \omega^2 \tag{2.13}$$

The production terms of the k and ω transport equations are defined as:

$$P_k = \left(2\mu_t S_{ij} \cdot S_{ij} - \frac{2}{3}\rho k \frac{\partial U_i}{\partial x_j}\delta_{ij}\right) \tag{2.14}$$

$$P_\omega = \gamma\left(2\rho S_{ij} \cdot S_{ij} - \frac{2}{3}\rho\omega \frac{\partial U_i}{\partial x_j}\delta_{ij}\right) \tag{2.15}$$

Here γ, β_k, β_ω, σ_k and σ_ω are model constants.
One of the advantages of this model is that it does not require wall-damping functions in low Reynolds number applications as k is set to zero and ω tends to infinity near the wall. [Versteeg and Malalasekra, 2007, pg. 91] Turbulent boundary conditions have to be given at the inlet (normally turbulent intensity and mixing length) to determine k and ω. This model is known to be too sensitive to these turbulent boundary conditions, which is an issue since these conditions are not precisely known for many cases. Equation 2.11 in this model is problematic when boundary conditions are set to $k \to 0$ and $\omega \to 0$, which is common in external aerodynamics and aerospace applications.

2.2.2 Menter SST Model

Menter's SST Model is a modified $k-\omega$ model which attempts to avoid the issues of the $k-\omega$ model (as discussed before) by transforming the ϵ transport equation into the ω transport equation ($\epsilon = k\omega$). Moreover, Menter added blending functions and limiters to the eddy viscosity and production term. Menter endeavours to add some of the advantages of the $k-\epsilon$ model (not discussed here), which lie in the treatment of fully turbulent regions far from the wall. This yields

$$\frac{\partial\rho\omega}{\partial t} + \operatorname{div}(\rho\omega\mathbf{U}) = \operatorname{div}\left[\left(\mu + \frac{\mu_t}{\sigma_{\omega,1}}\right) grad(\omega)\right] + P_\omega - \beta\rho\omega^2 + \underbrace{2\frac{\rho}{\sigma_{\omega,2}}\frac{\partial k}{\partial x_k}\frac{\partial\omega}{\partial x_k}}_{\text{cross-diffusion term}} \tag{2.16}$$

When comparing this equation to equation 2.13, an extra term, the cross-diffusion term is

added, arising from the transformation of ϵ into the ω transport equation. During the calculation of the k equation, the ω production term P_ω and the Reynolds stress computation do not change compared to Wilcox $k-\omega$ model, aside for some slight adjustments of model constants. Limiting functions are added to the eddy viscosity

$$\mu_t = \frac{a_1 \rho k}{\max(a_1 \omega, S F_2)} \tag{2.17}$$

where a_1 is a constant, $S = \sqrt{2 S_{ij} \cdot S_{ij}}$ and F_2 is a blending function to achieve a smooth transition between near wall ($k-\omega$ characteristics) and far flow ($k-\epsilon$ characteristics) regions.
And the k production term is

$$P_k = \min\left(10 \beta_k \rho k \omega, 2 \mu_t S_{ij} \cdot S_{ij} - \frac{2}{3} \rho k \frac{\partial U_i}{\partial x_j} \delta_{ij}\right) \tag{2.18}$$

3 Transition Modelling

Although several improvements were achieved with the Menter SST turbulence model in regions near the wall, no turbulence model is capable of predicting transitional boundary layer. While for a wide range of engineering applications the effects of a transitional boundary layer are negligible, they must be considered e.g. in the airfoil and blade design of a thermal turbomachine as the location and mode of transition have a huge impact on their efficiency (see figure 3.1). On the other hand a precise prediction of the location of transition on an airfoil can help the blade designers to realize a strong deflection without separation of the flow, which can lead to the development of turbines with fewer stages.

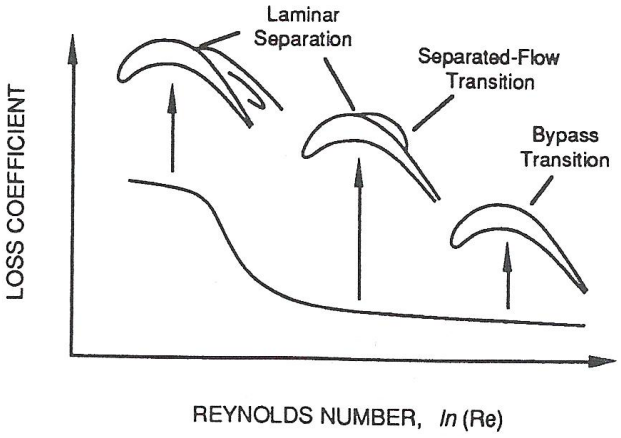

Figure 3.1: Transition on an airfoil and its influence on losses [Mayle, 1991]

3.1 Modes of Transition

Natural Transition

In flows with a low free stream turbulence intensity ($Tu_\infty < 0.5\%$), instabilities can occur in the laminar boundary layer causing disturbances that might eventually result in structures called Tollmien-Schlichting waves. These waves can amplify and lead to a formation of turbulent spots, which can merge to obtain a fully turbulent boundary layer. This mode of transition is called natural transition. Figure 3.2 shows all stages of this mode of transition. In a thermal turbo engine this kind of transition mode is rarely seen due to the high turbulence intensity of the flow.

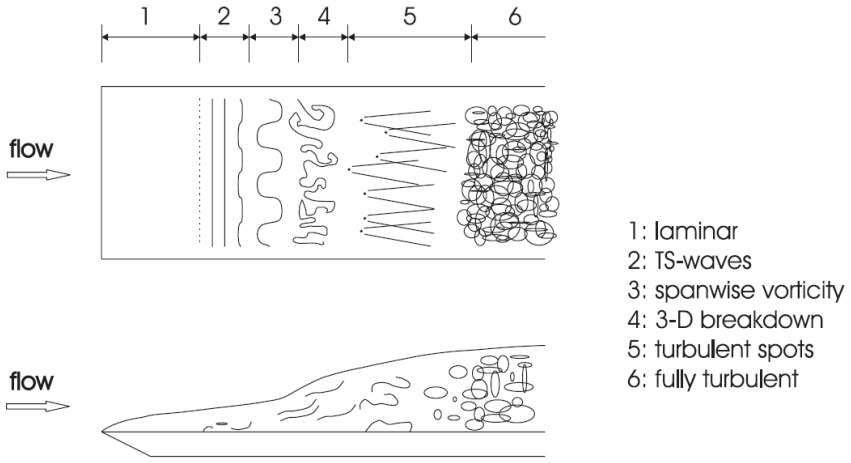

Figure 3.2: Process of natural transition in boundary layer flow over a flat plate [Schlichting and Gersten, 2000]

Bypass Transition

In flows with a high free stream turbulence intensity ($Tu_\infty > 0.5\%$), the production of the Tollmien-Schlichting waves can be bypassed, so that the turbulent spots are directly produced in the laminar boundary layer by the influence of the free stream disturbances, causing what is known as the bypass transition. Since the process of transition in this mode does not involve Tollmien-Schlichting waves, a model of this mode would only be required to describe the production, growth and convection of turbulent spots.

Separation-Induced Transition

Due to a strong adverse pressure gradient a laminar boundary flow may separate from the wall and contact a turbulent layer, which causes the separated flow to become turbulent so that it may reattach as a turbulent flow. The surface bubble, formed in this manner, is called separation bubble. The length of the separation bubble depends on the transition process of the separated laminar layer. It is possible that the flow undergoes all stages of natural transition. A long bubble produces large losses.

In the test cases used in this work, only bypass and separation-induced transition occurs.

Wake-Induced Transition

A wake, produced by a blade, usually has a high turbulent intensity. The wake of an upstream blade can promote a quick transition when penetrating a laminar boundary layer. While this is an important transition mode in actual turbo machines, this mode does not occur in our test cases, since no multistage test cases were considered.

3.2 Empirical Transition Modelling

Measurements have shown that a flow in the transitional zone has partly turbulent and partly laminar characteristics (see figure 3.3).

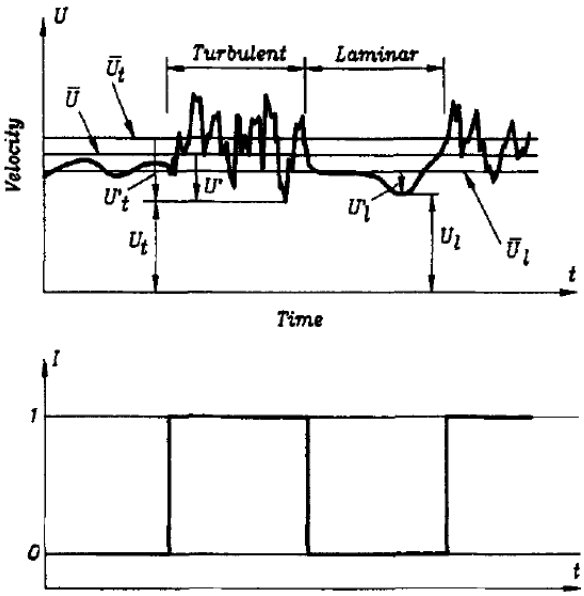

Figure 3.3: Typical point velocity measurement in transitional flow [Steelant and Dick, 1996]

Therefore, it seems reasonable to describe transition by an intermittency factor γ, which gives the fraction of time when the flow is turbulent. Emmons [1951] claims, that a boundary layer flow related quantity f in the transitional flow is a blend of that quantity at a fully laminar and turbulent flow respectively.

$$f = (1 - \gamma) f_L + \gamma f_T \tag{3.1}$$

The intermittency factor can easily be derived from the intermittency function $I(t)$, which can be best described as a Boolean variable, which becomes one if the flow becomes turbulent and zero if the flow is laminar. The intermittency factor is defined as the time averaged intermittency function.

$$I(t) = \begin{cases} 1 & \text{turbulent} \\ 0 & \text{nonturbulent} \end{cases} \tag{3.2}$$

$$\gamma = \lim_{T \to \infty} \frac{1}{T} \sum_{t}^{t+T} I(t) d(t) \tag{3.3}$$

The intermittency factor can then be used to trigger turbulence in a Navier-Stokes Code.

There are two basic ideas to implement the intermittency:

$$\mu_{eff} = \mu_l + \gamma\mu_t \tag{3.4}$$

$$P_{k,eff} = \gamma P_k \tag{3.5}$$

The first possibility is to compute the turbulent viscosity with the intermittency to obtain the effective viscosity. The other concept is to trigger the turbulent energy production term in the k transport equation of the turbulence model (see equation 2.12) so that P_k is set to zero in the laminar boundary layer.

3.2.1 Algebraic Transition Modelling

Dhawan and Narasimha [1958] formulated an algebraic transition model along a fixed wall. In dimensionless form it is given as

$$\gamma = \begin{cases} 1 - e^{-\hat{n}\sigma(Re_x - Re_{xt})^2} & x \geq x_{tr} \\ 0 & x < x_{tr} \end{cases} \tag{3.6}$$

where $\hat{n}\sigma$ is the turbulent spot production rate and Re_{xt} is the local Reynolds number at onset of transition. At a flat plate with zero pressure gradient (ZPG, $\frac{dp}{dx} = 0$) $\hat{n}\sigma_{ZPG}$ is only a function of the turbulence intensity Tu. Mayle [1991] collected measurement data of different authors (see figure 3.4) and calculated $\hat{n}\sigma_{ZPG}$ as

$$\hat{n}\sigma_{ZPG} = 1.5 \cdot 10^{-11} Tu^{7/4} \tag{3.7}$$

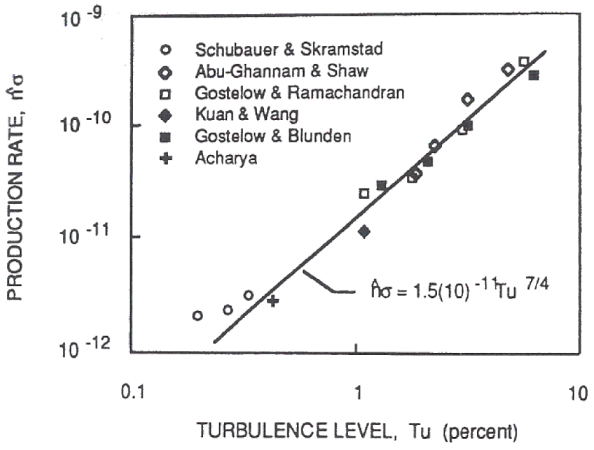

Figure 3.4: Spot production rate as a function of the free-stream turbulence level for zero pressure gradient flows [Mayle, 1991]

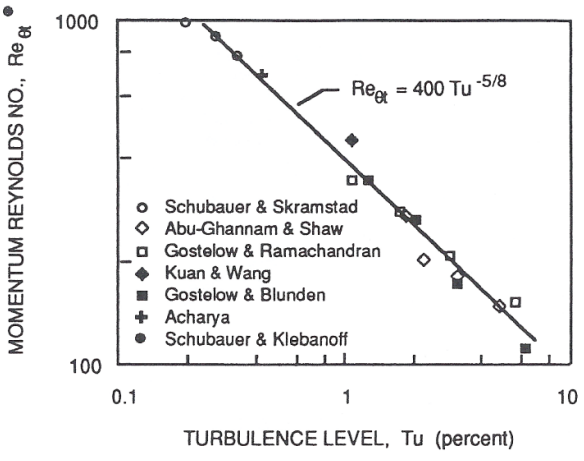

Figure 3.5: Momentum thickness Reynolds number at the onset of transition as a function of the free-stream turbulence level for zero pressure gradient flows [Mayle, 1991]

Now, to calculate Re_{xt}, the location of the transition onset is needed. Mayle [1991] found,

that the transition starts when the momentum thickness reaches a critical value, dependent on the turbulence intensity Tu. From the collected data (see figure 3.5) Mayle derived the following correlation:

$$Re_{\theta t} = 400 Tu^{-5/8} \tag{3.8}$$

In order to get the location of transition onset, the momentum thickness θ must be computed. From this, the momentum Reynolds number is calculated and compared to the critical momentum Reynolds number $Re_{\theta t}$. This procedure however becomes a problem in a computational environment, since, in order to get the momentum thickness θ an integral over the boundary layer height must be solved. This involves search algorithms to obtain the border of the boundary layer and a criterion to distinguish between boundary layer and free stream, which is a complex computational task and involves the use of nonlocal variables, which should be avoided in modern CFD environments.
These algebraic models are one dimensional. Implementing them into a three dimensional CFD environment leads to some issues. One issue is that boundary layer effects normal to the wall can not be resolved, e.g. the γ distribution normal to the wall (see figure 3.6). To simulate this, additional functions would have to be used to take the distance to the wall into account. Another problem is, that effects of the free stream turbulence on laminar boundary layer are not considered. Due to these facts, these models become unusable when multiple walls appear.

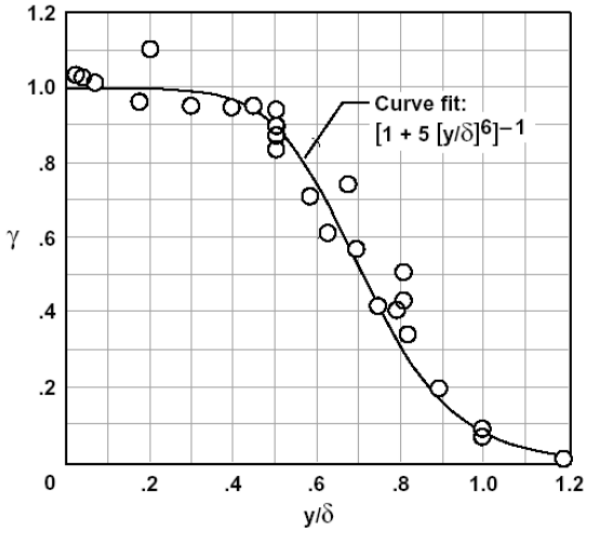

Figure 3.6: Distribution of γ normal to wall [Klebanoff, 1955]

Another problem is, that γ is set to zero at $x < x_{tr}$ and is therefore not able to take into account turbulent spots in that region which do affect the transitional process.

Algebraic Transition Model by Abu-Ghannam and Shaw [1980]

A very popular algebraic transition model was developed by Abu-Ghannam and Shaw [1980]. Instead of being concerned about the physics of the transition process, their approach was to relate boundary-layer quantities to external parameters. Resultant correlations were determined experimentally.
Abu-Ghannam and Shaw [1980] related the start of transition $Re_{\theta S}$ to the turbulence intensity Tu and the pressure gradient parameter λ_θ.

$$Re_{\theta S} = f(Tu, \lambda_\theta) \tag{3.9}$$

Relating the end of transition $Re_{\theta E}$ to the same parameters is not possible due to scatter of results. Instead the end of transition is related to the start by a transition length Reynolds number $Re_{L\gamma}$ as

$$Re_{xE} = Re_{xS} + Re_L \tag{3.10}$$

$$\text{where} \qquad Re_L = 3.36 Re_{L\gamma} \tag{3.11}$$

$Re_{L\gamma}$ is based on L_γ, which is the length of the transition region over which the intermittency factor γ increases from 0.25 to 0.75.
The boundary layer parameters momentum thickness θ, shape factor H, skin friction coefficient c_f and intermittency γ during transition are related to a non dimensional distance from start to end of transition η.

$$\eta = \frac{Re_x - Re_{xS}}{Re_{xE} - Re_{xS}} \tag{3.12}$$

To calibrate the system, Abu-Ghannam and Shaw [1980] did experiments on a flat plate with six turbulence levels from 0.5 to 5 % and five different pressure gradients (one ZPG, two FPG and two APG test cases).
The following correlation was found for the start of transition $Re_{\theta S}$:

$$Re_{\theta S} = 163 + exp(F(\lambda_\theta) - \frac{F(\lambda_\theta)}{6.91} Tu) \tag{3.13}$$

where

$$F(\lambda_\theta) = \begin{cases} 6.91 + 12.75\lambda_\theta + 63.64\lambda_\theta^2 & \lambda_\theta \leq 0 \\ 6.91 + 2.48\lambda_\theta - 12.27\lambda_\theta^2 & \lambda_\theta > 0 \end{cases} \tag{3.14}$$

Abu-Ghannam and Shaw [1980] found, that the transition length Reynolds number $Re_{L\gamma}$

can be related to the Reynolds number at start of transition Re_{xS} by

$$Re_{L\gamma} = 5Re_{xS}^{0.8} \tag{3.15}$$

so that equation 3.10 can be rewritten as

$$Re_{xE} = Re_{xS} + 16.8Re_{xS}^{0.8} \tag{3.16}$$

The following correlations were found for the boundary Layer parameters during transition. A visualization of these correlations is shown in figure 3.7

$$\theta' = \eta^{1.35} \qquad \theta' = \frac{\theta - \theta_S}{\theta_E - \theta_S} \tag{3.17}$$

$$H' = \sin(\frac{\pi}{2} \cdot \eta) \qquad H' = \frac{H_S - H}{H_S - H_E} \tag{3.18}$$

$$\gamma = 1 - \exp(-5\eta^3) \tag{3.19}$$

$$c_f' = 1 - \exp(-5.645\eta^2) \qquad c_f' = \frac{c_f - c_{fS}}{c_{fE} - c_{fS}} \tag{3.20}$$

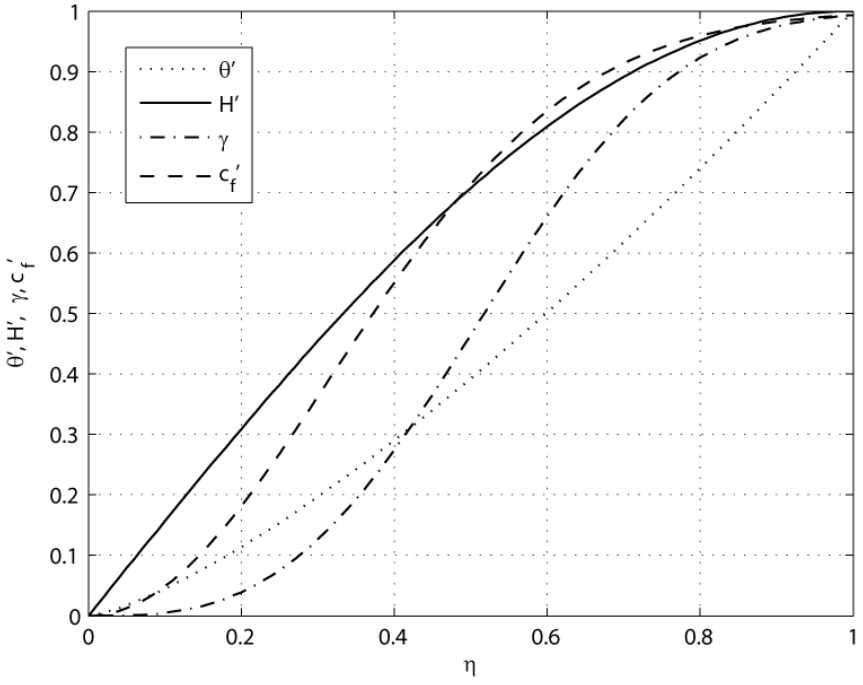

Figure 3.7: Visualization of the boundary layer parameters of the algebraic transition model by Abu-Ghannam and Shaw [1980]

3.2.2 Transition Modelling using Intermittency Transport Equation

The development of an intermittency transport equation to model the transitional process addresses some of the the issues that arise in the algebraic transition model. The main enhancements are the ability of implementing the transport equation in a three dimensional environment and of using it uniformly in the whole flow field.
Steelant and Dick [1996] derived the intermittency transport equation. The first step is to differentiate the algebraic intermittency equation 3.6 with respect to x.

$$\frac{d\gamma}{dx} = 2(1-\gamma)\underbrace{\hat{n}\sigma_{ZPG}\frac{U_\infty^2}{\nu^2}(x-x_{tr})}_{\beta(x)} \tag{3.21}$$

Multiplying this equation with ρu_s, u_s is the velocity along a streamline in the boundary layer leads to a one dimensional transport equation for γ.

$$\rho u_s \frac{d\gamma}{dx} = 2(1-\gamma)\beta(x)\rho u_s \tag{3.22}$$

From this equation, a two dimensional, unsteady transport equation can be obtained.

$$\frac{d\rho\gamma}{dt} + \frac{d\rho\gamma}{dx} + \frac{d\rho\gamma}{dy} = \underbrace{2(1-\gamma)\beta(x)\rho\sqrt{u^2+v^2}}_{P_\gamma} \tag{3.23}$$

Equation 3.23 is the basis for further developments by many authors allowing them to take into account effects of the pressure gradient, distributed breakdown, compressibility and to simulate the γ distribution normal to the wall (see figure 3.6).

Effect of Pressure Gradient

In thermal turbomachines, the blades are almost always exposed to a pressure gradient. This leads to an acceleration/deceleration of the flow. To analyze those flows, a dimensionless acceleration parameter was defined as

$$K = \frac{\nu}{U^2}\frac{dU}{dx} \tag{3.24}$$

Mayle [1991] shows, that the pressure gradient has a great influence on both the turbulent spot production rate $\hat{n}\sigma$ (see figure 3.8) as well as the location of transition onset (see figure 3.9). It is shown, that the turbulent spot production rate is extremely sensitive to the turbulence intensity Tu at adverse pressure gradients. Figure 3.9 shows also the influence of the turbulence intensity and the acceleration parameter on the mode of transition. The dotted lines represent the stability criterion. The region between the two dotted lines represents the zone of natural transition. To the right is the region of bypass transition and

to the left is the region of separation-induced transition.

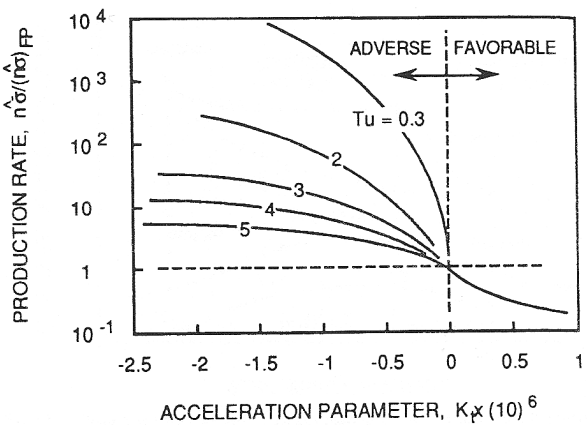

Figure 3.8: Suggested correlation of the spot production rate with the acceleration parameter at transition [Mayle, 1991]

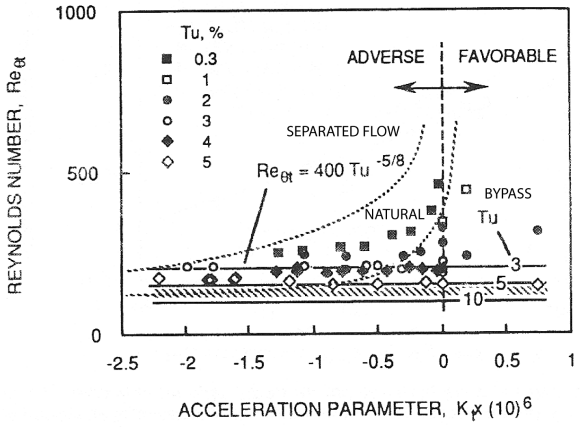

Figure 3.9: The Reynolds number of transition as a function of the acceleration parameter at transition for various free-stream turbulence levels [Mayle, 1991]

3.3 The $\gamma - Re_\theta$ Transition Model

The $\gamma - Re_\theta$ transition model is able to predict all transition modes. It is designed to meet the requirements of modern CFD codes and thus only uses local information of the flow. Menter et al. [2004] gives the framework of how to implement such a model, but did not publish all the correlations in his original work due to proprietary reasons. The proposed transport equations do not attempt to model the physics of the transition process. The physics of the transition process is contained entirely in the experimental correlations.
The $\gamma - Re_\theta$ transition model uses two transport equations, one for the intermittency γ, which triggers the transition process ($\gamma = 0$ fully laminar, $\gamma = 1$ fully turbulent) and one for the transition momentum thickness Reynolds number $\tilde{Re}_{\theta t}$.The intermittency is linked to the turbulence model and is used to turn on the production of the turbulent kinetic energy ($P_k = P_{kTurbModell} \cdot \gamma_{TransitionModell}$) downstream of the onset of transition.
The transport equation for the intermittency is formulated as:

$$\frac{\partial(\rho\gamma)}{\partial t} + \frac{\partial(\rho U_j \gamma)}{\partial x_j} = P_\gamma - E_\gamma + \frac{\partial}{\partial x_j}\left[\left(\mu + \frac{\mu_t}{\sigma_f}\right)\frac{\partial \gamma}{\partial x_j}\right] \tag{3.25}$$

In the case of a separation of the laminar boundary layer, γ is also allowed to become higher than one, leading to fast production of turbulence and hence a rapid reattachment.
The transport equation for the transition momentum thickness Reynolds number is needed to capture non local influences of the turbulence. It links the empirical correlations to the onset criteria of the intermittency equation and is needed in order to enable for this model

to be used in general geometries and over multiple blades. It is defined as:

$$\frac{\partial(\rho\tilde{Re}_{\theta t})}{\partial t} + \frac{\partial(\rho U_j \tilde{Re}_{\theta t})}{\partial x_j} = P_{\theta t} + \frac{\partial}{\partial x_j}\left[\sigma_{\theta t}(\mu + \mu_t)\frac{\partial \tilde{Re}_{\theta t}}{\partial x_j}\right] \tag{3.26}$$

where

$$P_\gamma = f(F_{length}, F_{onset}) \tag{3.27}$$
$$E_\gamma = f(F_{length}, F_{onset}) \tag{3.28}$$
$$P_{\theta t} = f(Re_{\theta t}) \tag{3.29}$$

The parameter F_{onset} controls the start of transition, F_{length} the length of the transition zone and $Re_{\theta t}$ is the local momentum thickness Reynolds number at onset of transition. F_{onset} itself is a function of the vorticity Reynolds number Re_v and the transition Reynolds number $Re_{\theta c}$ $F_{onset} = f(Re_v, Re_{\theta c})$, so that in the end three correlations must be found to close the system.

$$Re_{\theta c} = f(\tilde{Re}_{\theta t}) \tag{3.30}$$
$$F_{length} = f(\tilde{Re}_{\theta t}) \tag{3.31}$$
$$Re_{\theta t} = f(Tu, ...) \tag{3.32}$$

Menter et al. [2004] proposes to link the momentum thickness Reynolds number Re_θ to the vorticity Reynolds number Re_ν. Normally, the momentum thickness Reynolds number Re_θ is calculated as a function of the momentum thickness θ. The momentum thickness θ is calculated by an integral over the height of the boundary layer. This procedure is unfeasible, because it would not agree with the requirements of modern CFD codes to use only local parameters. The momentum thickness Reynolds number Re_θ is linked to the vorticity Reynolds number Re_ν as

$$Re_\theta = \frac{Re_{\nu\,max}}{2.193} \tag{3.33}$$

Model Calibration for $Re_{\theta c}$ and F_{length}

Malan et al. [2009] described the calibration process as follows. The development of plausible forms for $Re_{\theta c}$ and $Re_{\theta t}$ is relied on both physical intuition and numerical experiments. $Re_{\theta c}$ is the critical momentum thickness Reynolds number at which intermittency first starts to grow. $\tilde{Re}_{\theta t}$ is the momentum thickness Reynolds number at which the skin friction coefficient starts to increase. Since the production of γ starts before a rise of the skin

friction coefficient can be noticed $Re_{\theta c} \leq \tilde{Re}_{\theta t}$. The simplest mathematical relationship between $Re_{\theta c}$ and $\tilde{Re}_{\theta t}$ is a linear one $Re_{\theta c} = a\tilde{Re}_{\theta t} + b$ where $a < 1$.
To obtain a viable form for F_{length} the following numerical experiment was done:

1. Use equation 3.34 or 3.38 to obtain $Re_{\theta t}$.
2. Assume that $Re_{\theta c} = Re_{\theta t}$.
3. Adjust F_{length} to fit the experimental skin friction data.

From this numerical experiment an inverse relationship between F_{length} and $\tilde{Re}_{\theta t}$ becomes clear. Since large values of $\tilde{Re}_{\theta t}$ correspond to very small values of F_{length}, a logarithmic relationship of the form $F_{length} = A \exp(B - C\tilde{Re}_{\theta t})$ is suggested by Malan et al. [2009]. The unknown constants a, b, A, B and C are varied to get the best curve fit for a series of test cases. Every test case corresponds to one calibration point. It is suggested to use test cases where different modes of transition (natural, bypass and separation induced) occur.

Correlations by Menter

Menter et al. [2004] was the first to formulate a $Re_{\theta t}$ correlation for the $\gamma - Re_\theta$ transition model. He derived this correlation by curve fitting existing correlations, e.g. the correlation by Abu-Ghannam and Shaw [1980] which is known to behave well for zero and adverse pressure gradients.

$$Re_{\theta t} = 803.73[Tu + 0.6067]^{-1.027} F(\lambda_\theta, K) \tag{3.34}$$

$$F(\lambda_\theta, K) = \begin{cases} 1 - [-10.32\lambda_\theta - 89.47\lambda_\theta^2 - 265.51\lambda_\theta^3]e^{[-Tu/3]} & \lambda_\theta \leq 0 \\ 1 + [0.0962[K\,10^6] + 0.148[K\,10^6]^2 + 0.0141[K\,10^6]^3] & \\ \quad \times(1 - e^{-Tu/1.5}) + 0.556[1 - e^{-23.9\lambda_\theta}]e^{-Tu/1.5} & \lambda_\theta > 0 \end{cases} \tag{3.35}$$

To obtain correlations for $Re_{\theta c}$ and F_{length}, Menter et al. [2004] used nine flat plate test cases. T3A, T3A-, T3B, S&K (Schubauer and Klebanof), T3C2, T3C3, T3C4, T3C5 and a relaminarization test case. The T3A, T3A- and T3B test cases are zero pressure gradient flat plate test cases. The Schubauer and Klebanof (S&K) test case has a low freestream turbulence intensity and corresponds to natural transition. The T3C2, T3C3, T3C4 and T3C5 flat plate test cases feature a pressure gradient. The geometry for the T3C* test cases is the same. The wind-tunnel Reynolds number was varied for the four cases. Thus, the location of transition moves from the beginning of the plate (favorable pressure gradient) to the end of the plate (adverse pressure gradient). For the relaminarization test case, the opposite converging wall imposes a strong favorable pressure gradient that can relaminarize a turbulent boundary layer.

Due to proprietary reasons Menter's correlations for $Re_{\theta c}$ and F_{length} were published later than his correlation for $Re_{\theta t}$. [Langtry and Menter, 2009]

$$Re_{\theta c} = \begin{cases} \tilde{Re}_{\theta t} - (396.035 \cdot 10^{-2} + (-120.656 \cdot 10^{-4})\tilde{Re}_{\theta t} \\ \quad +(868.23 \cdot 10^{-6})\tilde{Re}_{\theta t}^{2} - 696.506\tilde{Re}_{\theta t}^{3} \\ \quad +174.105 \cdot 10^{-12}\tilde{Re}_{\theta t}^{4}) & \tilde{Re}_{\theta t} \leq 1870 \\ \tilde{Re}_{\theta t} - (593.11 + 0.482(\tilde{Re}_{\theta t} - 1870)) & \tilde{Re}_{\theta t} > 1870 \end{cases} \tag{3.36}$$

$$F_{length} = \begin{cases} 398.189 \cdot 10^{-1} - 119.270 \cdot 10^{-4}\tilde{Re}_{\theta t} \\ \quad -132.567 \cdot 10^{-6}\tilde{Re}_{\theta t}^{2} & \tilde{Re}_{\theta t} < 400 \\ 263.404 - 123.939 \cdot 10^{-2}\tilde{Re}_{\theta t} + (194.548 \cdot 10^{-5})\tilde{Re}_{\theta t}^{2} \\ \quad -101.695 \cdot 10^{-8}\tilde{Re}_{\theta t}^{3} & 400 \leq \tilde{Re}_{\theta t} < 596 \\ 0.5 - 3.0\tilde{Re}_{\theta t} - 596.0 \cdot 10^{-4} & 596 \leq \tilde{Re}_{\theta t} < 1200 \\ 0.3188 & 1200 \leq \tilde{Re}_{\theta t} \end{cases} \tag{3.37}$$

Correlations by Langtry

Langtry and Menter [2009] revised Menters correlation for $Re_{\theta t}$. The main difference is, that the revised correlation does not take into account the flow acceleration parameter K.

$$Re_{\theta t} = \begin{cases} \left[1173.51 - 589.428Tu + \frac{0.2196}{Tu^2}\right] F(\lambda_\theta) & Tu \leq 1.3 \\ 331.5\left[Tu - 0.5658\right]^{-0.671} F(\lambda_\theta) & Tu > 1.3 \end{cases} \tag{3.38}$$

where

$$F(\lambda_\theta) = \begin{cases} 1 - [-12.986\lambda_\theta - 123.66\lambda_\theta^2 - 405.689\lambda_\theta^3]e^{-[Tu/1.5]^{1.5}} & \lambda_\theta \leq 0 \\ 1 + 0.275[1 - e^{0.35\lambda_\theta}]e^{-Tu/0.5} & \lambda_\theta > 0 \end{cases} \tag{3.39}$$

Correlations by Malan

To find suitable correlations for $Re_{\theta c}$ and F_{length}, Malan et al. [2009] used four flat plate zero pressure gradient test cases (T3B, T3A, T3AM and S&K) and five flat plate test cases with pressure gradient (T3C1, T3C2, T3C3, T3C4, T3C5).

$$Re_{\theta c} = min\left(0.615\tilde{Re}_{\theta t} + 61.5, \tilde{Re}_{\theta t}\right) \tag{3.40}$$

$$F_{length} = min\left(exp\left(7.168 - 0.01173\tilde{Re}_{\theta t}\right) + 0.5, 300\right) \tag{3.41}$$

Correlations by Kelterer

The following correlations for $Re_{\theta c}$ and F_{length} were developed by Kelterer et al. [2010], using the flat plate test cases T3A, T3B, T3C1, T3C2 and T3C4. The calibration procedure is similar to that proposed by Malan et al. [2009].

$$Re_{\theta c} = \begin{cases} 1.02\tilde{Re}_{\theta t} - 35 + 36 \cdot tanh\left(-\frac{\tilde{Re}_{\theta t}-138}{54}\right) & \tilde{Re}_{\theta t} \leq 215 \\ 45 \cdot tanh\left(\frac{\tilde{Re}_{\theta t}-215}{15}\right) + 155 & \tilde{Re}_{\theta t} > 215 \end{cases} \tag{3.42}$$

$$F_{length} = min\left(250 \cdot exp\left[-\left(\frac{\tilde{Re}_{\theta t}}{130}\right)^{1.7}\right] + 10, 40\right) \tag{3.43}$$

In figure 3.10 a visualization of the correlations is shown. While for $Re_{\theta c}$ the correlations of Malan and Menter are very similar, the Kelterer correlation differs as it is limited. For the correlation of F_{length}, all three authors found somewhat different formulations.

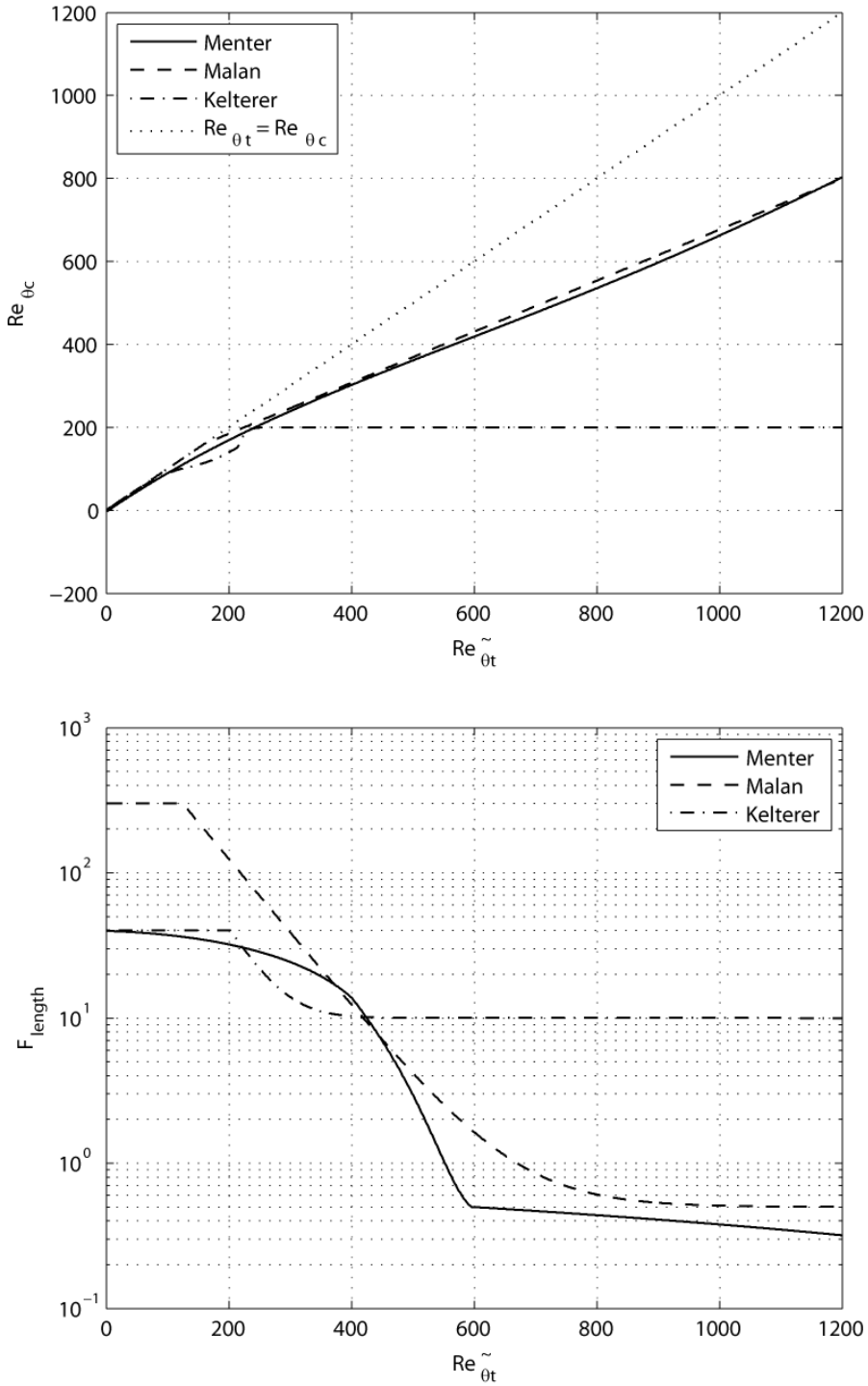

Figure 3.10: Visualization of the correlations for $Re_{\theta c}$ and F_{length}

4 LINARS and TRACE CFD Codes

In this work, the LINARS and TRACE CFD codes are used to calculate transitional flows.

LINARS Inhouse code of the Institute for Thermal Turbomachinery and Machine Dynamics of Graz University of Technology.

TRACE CFD code developed by the German Aerospace Center (DLR) in cooperation with MTU - Aero Engines.

LINARS uses the $k-\omega$ and SST turbulence models, while TRACE only uses the $k-\omega$ turbulence model. Both codes use the previously mentioned $\gamma - Re_\theta$ model to simulate transition. In LINARS various correlations can be used to solve transitional flows. An overview of the models used is given in table 4.1.

	Code	Turbulence model	$Re_{\theta t}$	$Re_{\theta c}$	F_{length}
LINARS corr Kelteer	LINARS	SST	Menter	Kelterer	Kelterer
	LINARS	$k-\omega$	Menter	Kelterer	Kelterer
LINARS corr DLR	LINARS	SST	Menter	Malan	Malan
	LINARS	$k-\omega$	Menter	Malan	Malan
LINARS corr Malan	LINARS	SST	Langtry	Malan	Malan
	LINARS	$k-\omega$	Langtry	Malan	Malan
TRACE	TRACE	$k-\omega$	Menter	Malan	Malan

Table 4.1: CFD codes implied models

4.1 Numerical Method

In the LINARS code, the compressible Reynolds/Favre-averaged Navier-Stokes (RANS) equations are solved in conservative form by means of a fully-implicit finite-volume method on structured curvilinear grids. The inviscid (Euler) fluxes are discretized with the upwind flux-difference splitting method by Roe. In order to achieve a high order of spatial accuracy a total variation diminishing (TVD) scheme with third-order interpolation was applied to obtain the state vector at each cell interface. The viscid flux vector at the cell interfaces is constructed with a second-order accurate central-differencing scheme. To obtain a linear set of the governing equations the Newton-Raphson procedure is applied for the discretization

in time.

The TRACE code is a density-based Navier-Stokes solver, developed especially for turbomachinery use. TRACE is a hybrid solver using structured as well as unstructured grids and allows the running a parallel simulation using multiple processors. It features a second-order-accurate upwind spatial discretization by Roe with the MUSCL or linear reconstruction approach. Another feature is the first- or second-order accurate implicit predictor corrector formulation. TRACE has adopted a wide range of models for turbomachinery flows. Some are

- Implicit steady and unsteady nonlinear solvers
- Implicit nonreflecting boundary conditions
- Higher Order discretization schemes

4.2 Usability

The LINARS code uses three text files as input files. The main file is the control file, which specifies the models used and their parameters. The second, known as the faces file specifies the boundary conditions and the geometry file the geometric coordinates. The output files are a Tecplot file, which allows the easy visualization of the flow field, as well as several ASCII data files, containing flow parameters at given domains, as specified in the faces file. The ASCII data files are especially useful in analyzing the data in MatLab.

In TRACE, the complete simulation process chain is integrated, including the pre- and post-processing tools, with a standard interface (CGNS). The pre-processing tool used is called GMC. GMC provides a graphical user interface that enables the user to assign boundary conditions to specified interfaces and to set up the solver properties. It allows the use of input files to initialize values for interfaces as well as for the whole flow field. GMC allows the import of a grid from Tecplot, which is useful for the easy application of the same grid in LINARS and TRACE. GMC stores the grid data, boundary settings and solver settings in a CGNS file, which is the input file for the TRACE solver. The output file is a CGNS file as well, which can be imported to Tecplot. The post-processing tool, called POST45, was not used to analyze the data, instead a MatLab routine was programmed that allows the visualization of both, LINARS and TRACE results.

4.3 Sutherland Law

Temperature has an effect on the viscosity of a gas. The viscosity increases along with temperature. While the TRACE code always calculates the viscosity with the Sutherland

Law, LINARS allows the manual setting of a global viscosity. The Sutherland Law reads as follows:

$$\mu = \mu_{ref} \left(\frac{T}{T_{ref}} \right)^{3/2} \frac{T_{ref} + S}{T + S} \tag{4.1}$$

where the reference viscosity μ_{ref} is the measured viscosity at the reference temperature T_{ref}. The constants differ in LINARS and TRACE (see table 4.2).

	$\mu_{ref}[\frac{Ns}{m^2}]$	$T_{ref}[K]$	S
LINARS	1.876e-5	303.15 K	110.4
TRACE	1.7198e-5	273	110.4

Table 4.2: Constants of Sutherland Law in LINARS and TRACE

5 Ercoftac Flat Plate Test Cases

The main part of this work was to apply the LINARS and TRACE CFD codes to find a solution for a number of test cases.
The results are compared to experimental data and analytical solutions. Since the two codes run on the same machine, the performance of the two codes, e.g. number of iterations to converge, is compared.
Since the turbulent intensity and the turbulence length scale are unknown in our models, they have to be given as input parameters. The approach in the flat plate test cases was to determine these parameters by fitting the free stream turbulence of the simulation into the measured data points. Our system is then calibrated and we can proceed with calculating the distribution of the skin friction coefficient over the plate length. The results are then compared to experimental data.

Overview of the test cases

Table 5.1 gives an overview of the test cases and the applied transition models.

	T3A	T3C2	T3C4
LINARS SST corr Kelteer	x	x	x
LINARS $k-\omega$ corr Kelteer	x	x	x
LINARS SST corr DLR	x	x	x
LINARS $k-\omega$ corr DLR	x	x	x
LINARS SST corr Malan	x	x	x
LINARS $k-\omega$ corr Malan	x	x	x
TRACE	x	x	x

Table 5.1: Flat plate test case overview of the test cases and applied transition models

Figure 5.1 shows a definition of the 2D flat plate test cases with boundary conditions.

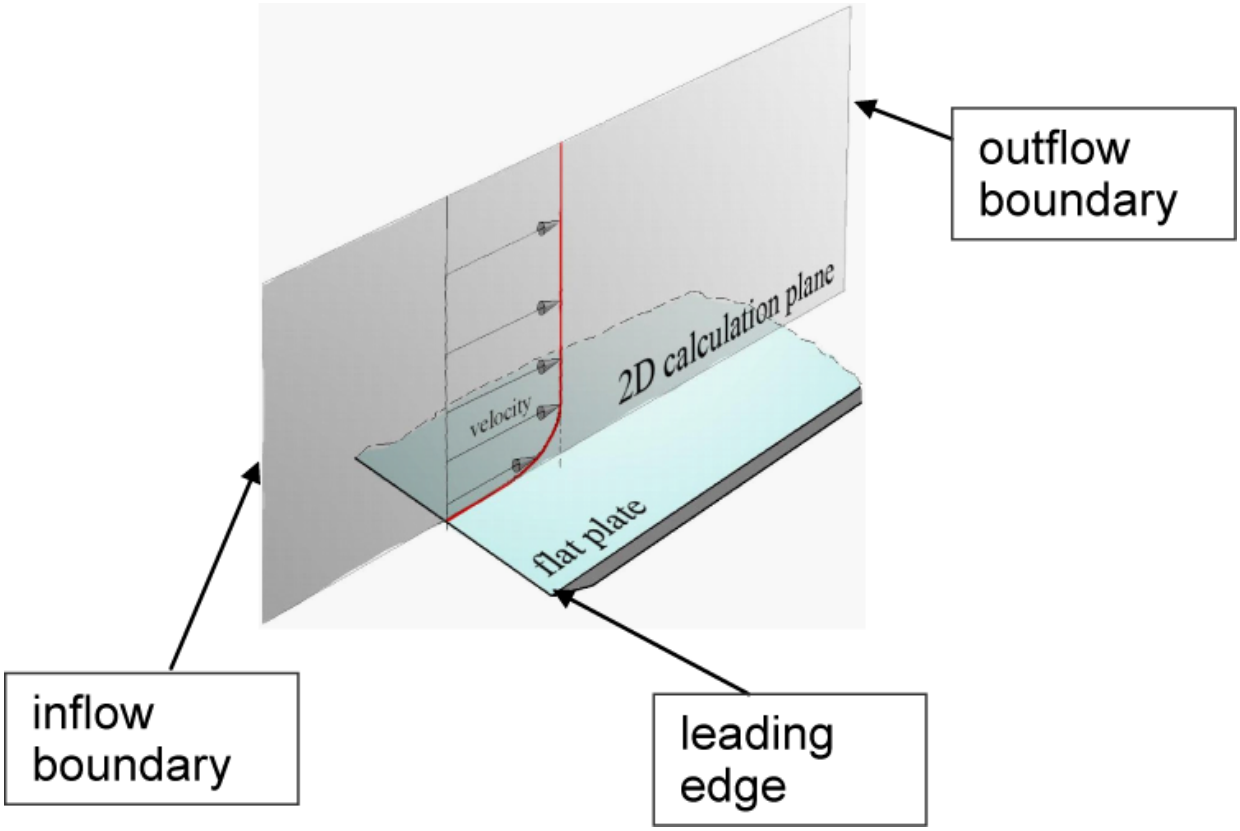

Figure 5.1: Definition of the flat plate test case [Pecnik, 2007]

5.1 T3A Test Case

The first test case is the T3A flat plate test without imposed pressure gradient. The Reynolds number for this case is $Re_L = 527300$. Measurements were done with air as the fluid on a plate with the length of $l = 1.5\ m$ and an inlet velocity of $U_{inlet} = 5.2\ m/s$.

5.1.1 T3A Test Case with LINARS

Since the LINARS code is optimized for compressible flows, the inlet velocity is adjusted so that the Mach number becomes $Ma = 0.3$, hence treating the flow as compressible. In order to achieve the same Reynolds number as in the experiments, the molecular viscosity is adjusted to $\mu = 6.743e-05\ \frac{kg}{s \cdot m}$. In the simulation, the plate length is $l_{Plate} = 0.3\ m$. The grid is shown in figure 5.2. The length is $l_{Grid} = 0.33\ m$ and the height is $h_{Grid} = 0.11\ m$, split in 80 and 64 cells respectively. Thus the start-up length is $l_s = 0.03\ m$.

The boundary conditions for the inlet and outlet are shown in table 5.2.
In order to ensure for LINARS converges, the simulation starts with a very stable turbulence model, the Spalat Allmaras One-Equation Model. During this step, the inlet boundary conditions for turbulence intensity and integral turbulent length scale are calibrated, so that the free stream turbulence distribution fits to experimental data. The result is used

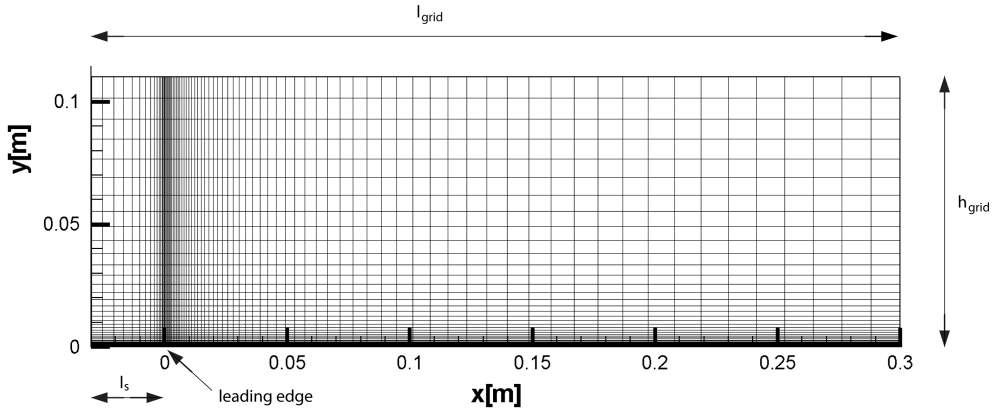

Figure 5.2: Grid of T3A test case

Inlet	Outlet
$p_{tot} = 1.01633932e5\ Pa$ $T_{tot} = 293.15\ K$	$p_{stat} = 0.953e5\ Pa$

Table 5.2: T3A boundary conditions

as the initial value for the turbulence models. The final calculation is done with enabled γ-Re$_\theta$ transition model.
In order to fit the distribution of the turbulence intensity to the experimental data, turbulent boundary conditions as given in table 5.3 are used.

Inlet	
Turbulence Intensity = 0.057	Integral Turbulent Length Scale = 2.05e-04 m

Table 5.3: T3A LINARS inlet turbulence boundary conditions

In the following diagrams, the turbulence intensity Tu and the skin friction coefficient c_f are defined as

$$Tu = \frac{\sqrt{\frac{2}{3}k}}{U_\infty} \cdot 100\ [\%] \tag{5.1}$$

$$c_f = \frac{2\tau_W}{\rho U_\infty^2} \tag{5.2}$$

Figure 5.3 shows the distribution of the turbulence intensity on the left hand side and the skin friction coefficient on the right hand side. All models match the experimental data quite well. While the correlation of Kelterer predicts the occurrence of transition somewhat prematurely, the correlation of the DLR with the SST turbulence model matches the measured data almost perfectly. Generally, we can see that the transitional zone with the $k-\omega$ turbulence model is shorter than with the SST model.

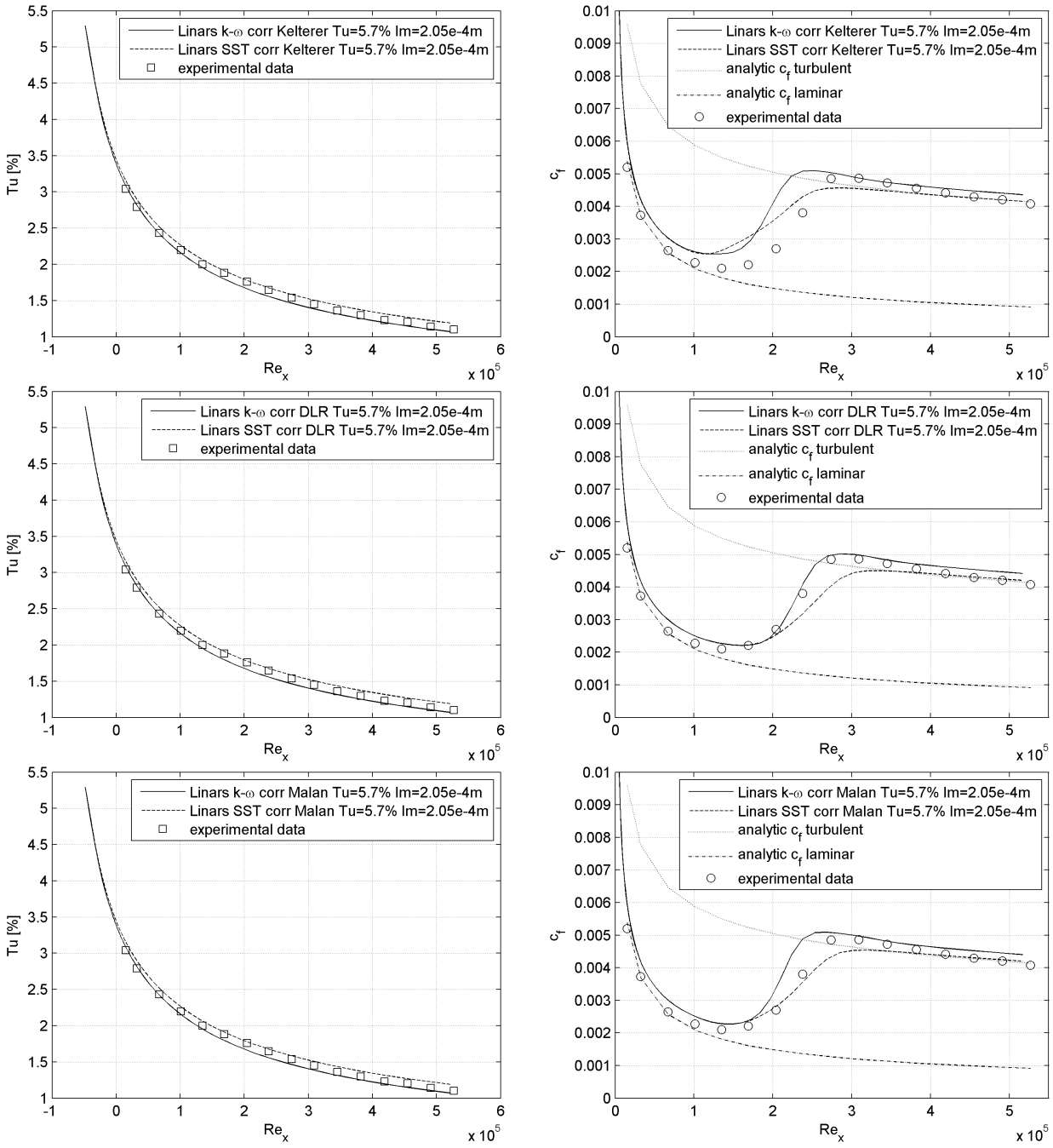

Figure 5.3: T3A: Free stream turbulence and skin friction coefficient with various correlations of the transition model (LINARS)

5.1.2 T3A Test Case with TRACE

When solving the T3A test case with TRACE, adjusting the boundary conditions to achieve Reynolds similarity is more complex than in LINARS. This is due to the fact that it is not possible to change the viscosity of the fluid manually in TRACE, but to calculate it with the Sutherland Law. In order to get the same Reynolds number other parameters had to be adjusted. These parameters were the velocity, thus changing the total pressure at inlet and the static pressure at outlet, and the length of the plate.

Inlet	Outlet
$p_{tot} = 101634\ Pa$	$p_{stat} = 100690\ Pa$
Global	
$l_{plate} = 0.2\ m$	

Table 5.4: T3A TRACE parameters

The pressure difference between inlet and outlet results in a velocity of $U_\infty = 39.3 m/s$. Thus the Reynolds number for the simulation $Re_L = 527300$ stays the same. The Mach number drops to $Ma = 0.12$, anyway, it turns out that Mach number similarity is negligible for this test.

To obtain a solution for this case, TRACE converges after 5000 iterations, with k-ω turbulence and PDE (γ-Re$_\theta$) transition mode enabled with no preiterations needed. So the computational effort drops significantly compared to the LINARS code. However, our approach to calibrate the inlet turbulence parameters fails for these kinds of problems in TRACE.

When calibrating the inlet turbulence parameters to fit the experimental data (see table 5.5), the calculated skin friction coefficient diverges from the measured data significantly (see figure 5.4). The onset of transition occurs too early. To fit the calculated transition onset to the measured data, the integral turbulent length scale must be adjusted. As derived from theory a smaller integral turbulent length scale moves the transition onset more downstream (see equation 5.3).

$$l_m \propto \frac{k^{3/2}}{\epsilon} \tag{5.3a}$$

$$k \propto \frac{1}{Re_{\theta t}} \tag{5.3b}$$

The effect of turbulence is an earlier transition onset. This tendency is predicted correctly in TRACE, as shown later (see figure 5.6).

We were unable to find settings to fit both, the freestream turbulent intensity and the skin

Inlet		
Tu fit	Turbulence Intensity = 0.052	Integral Turbulent Length Scale = 8e-05 m
c_f fit	Turbulence Intensity = 0.052	Integral Turbulent Length Scale = 1.8e-05 m

Table 5.5: T3A TRACE inlet turbulence boundary conditions to fit Tu and c_f distribution

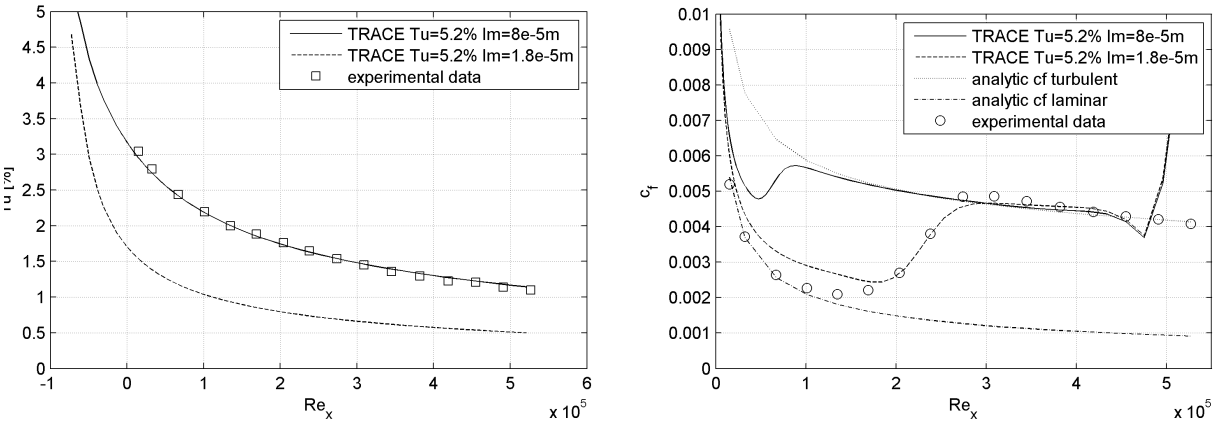

Figure 5.4: T3A: Free stream turbulence and skin friction coefficient to fit Tu,c_f distribution, boundary conditions as in table 5.5 (TRACE)

friction coefficient. The rise of the skin friction coefficient at the end of the plate (see 5.4) is probably related to the implementation of the boundary conditions. To ensure, we had made no mistakes with any of the settings in TRACE, the next step was to compare our results to the results of DLR.

DLR results

Edmund Kügeler, head of the Institute of Numerical Methods at DLR in Cologne, kindly provided us with his institute's calculation results for this test case. They achieved Reynolds number similarity on the original grid by dropping the total inlet pressure (see table 5.6) and thus the density, as predicted by the general gas equation.

Inlet	Outlet
$p_{tot} = 25408.5\ Pa$ $Tu_\infty = 5.7\ \%$ $l_m = 2.25e-05\ m$	$p_{stat} = 23825\ Pa$
Global	
$l_{Plate} = 0.3\ m$	

Table 5.6: T3A TRACE parameters used by DLR

With these settings the inlet velocity $U_\infty = 102.9\ m/s$ and the mach number $Ma = 0.3$ remain the same as in the LINARS tests. The Reynolds number $Re_L = 527300$ also stays the same.

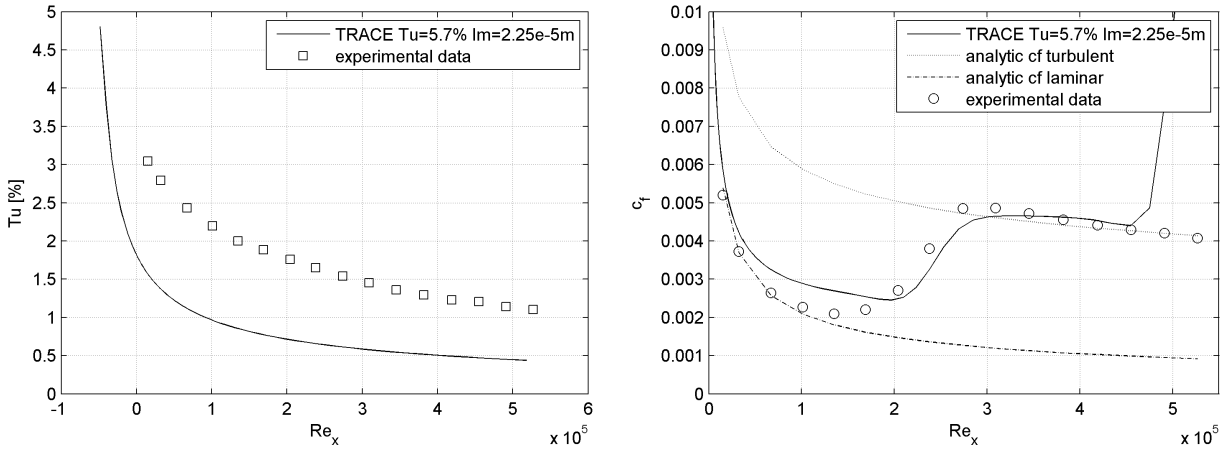

Figure 5.5: T3A: Free stream turbulence and skin friction coefficient results provided by DLR, with boundary conditions as in table 5.6 (TRACE)

Their results, as shown in figure 5.5, are very similar to our results. The DLR too was unable to fit both, the distribution of the skin friction coefficient and the free stream turbulence intensity. Also the rise of the skin friction coefficient at the end of the plate can be seen.

Transition onset sensitivity

The next test shows the transition onset sensitivity to the inlet turbulent length scale in TRACE. As predicted by equation 5.3, a smaller turbulent length scale leads to a later transition onset.

Inlet		
Test (1)	Turbulence Intensity = 0.052	l_m = 2.2e-05 m
Test (2)	Turbulence Intensity = 0.052	l_m = 1.6e-05 m

Table 5.7: T3A TRACE inlet turbulence boundary conditions for transition onset sensitivity study

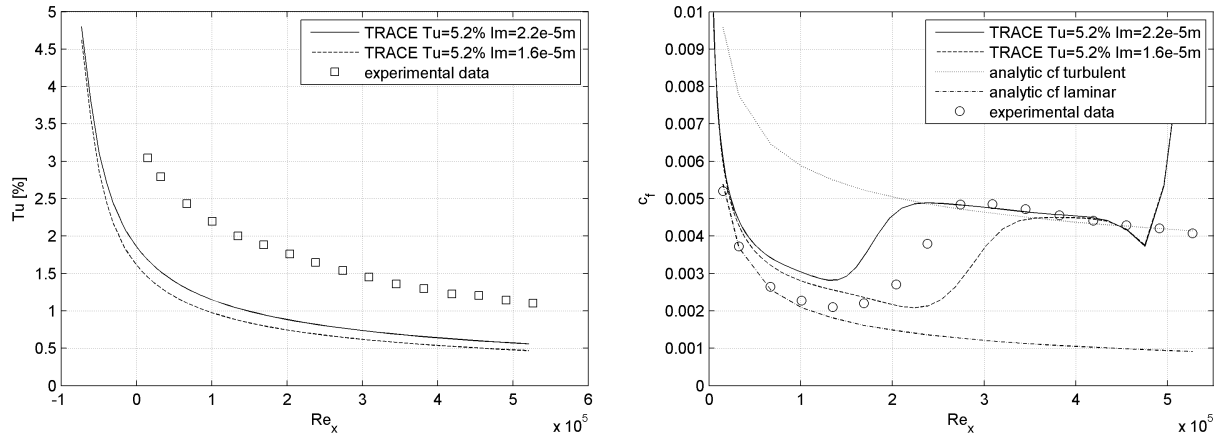

Figure 5.6: T3A: Free stream turbulence and skin friction coefficient with boundary conditions as in table 5.7 (TRACE)

5.1.3 TRACE and LINARS k-ω with identical turbulence boundary conditions

Since the LINARS and the TRACE code delivered different results for the T3A test case with enabled transition model, we were interested in the results of both codes for the same implied boundary conditions only with the k-ω turbulence model enabled and the transition model disabled.

The turbulence boundary conditions used are the same as the ones found to fit the skin friction coefficient in TRACE (Test(1)) and LINARS (Test(2)) and are stated in table 5.8.

Inlet		
Test (1)	Turbulence Intensity = 0.052	l_m = 1.8e-05 m
Test (2)	Turbulence Intensity = 0.057	l_m = 2.05e-04 m

Table 5.8: T3A TRACE and LINARS turbulence boundary conditions to compare k-ω turbulence model

In test(1) (figure 5.7) we can see that in LINARS the free stream turbulence decreases more sharply than in TRACE shortly after the inlet. However, the skin friction coefficient matches over a wide range. The bend at the beginning of the plate in the LINARS results can be explained by the sharp drop of the free stream turbulence in that region.

In test(2) (figure 5.8) the skin friction coefficient of the two codes again match very well, even though the free stream turbulence, as before, in LINARS drops more sharply than in TRACE.

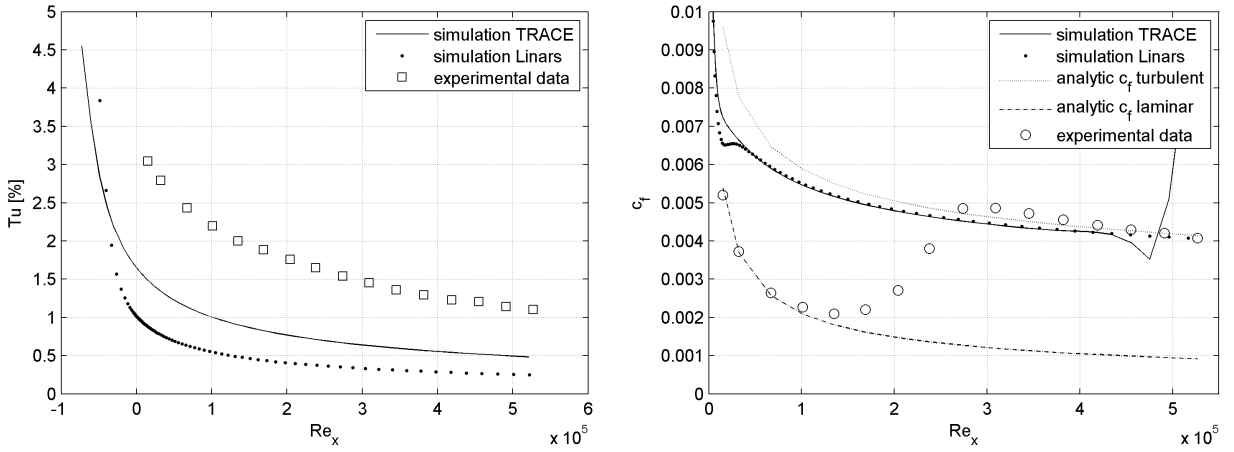

Figure 5.7: T3A: Free stream turbulence and skin friction coefficient with k-ω turbulence model, boundary conditions of test(1) in table 5.8 (TRACE and LINARS)

Figure 5.9 and 5.10 show the distribution of the turbulent kinetic energy for TRACE with boundary conditions as given in table 5.8 (1) and 5.8 (2) respectively. While analyzing these

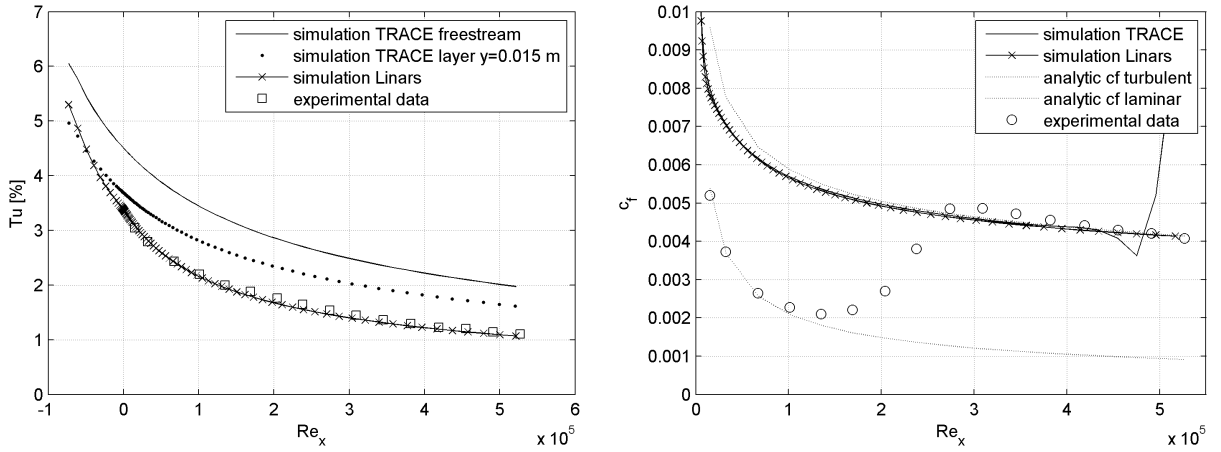

Figure 5.8: T3A: Free stream turbulence and skin friction coefficient with k-ω turbulence model, boundary conditions of test(2) in table 5.8 (TRACE and LINARS)

TRACE results, we noticed that the distribution of the turbulent kinetic energy varies over the height of the flow region (especially in figure 5.10). This behavior is realistic in the boundary layer, but in a region outside of the boundary layer, this behavior can not be explained physically.

Since the cause of this behavior was unknown, another test was done in which the plate was removed. The other boundary conditions were unchanged. This test brought the same result (see figure 5.11). The cause of this behavior is unknown, but we assume that the problem is related to the implementation of the boundary conditions. The DLR was contacted about this problem. While for turbo engines the preferred method to imply the boundary conditions is Fourier, they recommended that we use Non-reflecting boundary conditions for this kind of problem. All in all, this brought the same result. We also tried to fix the boundary conditions along the inlet, which can be achieved by providing an inlet boundary condition file in TRACE, but that, too, brought the same unphysical result.

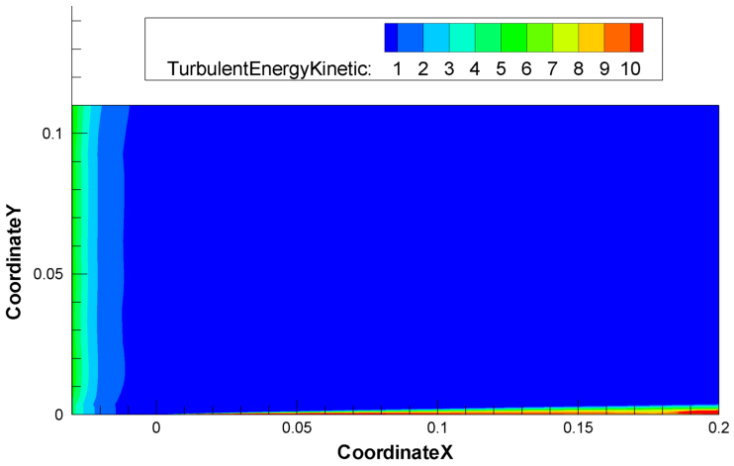

Figure 5.9: T3A: Turbulent kinetic energy distribution with k-ω turbulence model, with plate and boundary conditions of test(1) in table 5.8 (TRACE)

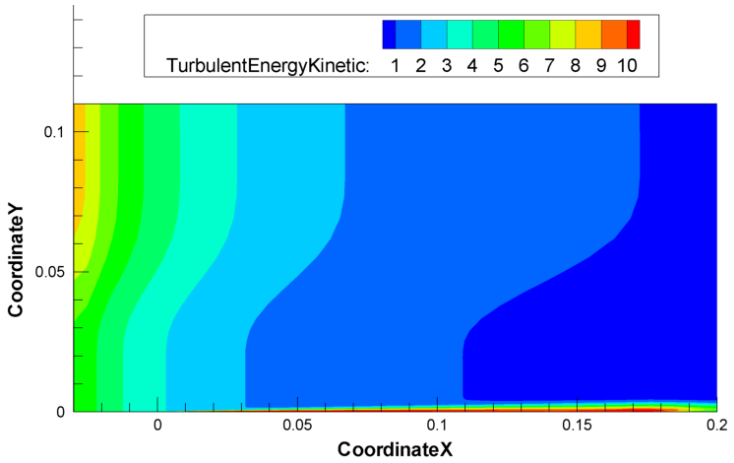

Figure 5.10: T3A: Turbulent kinetic energy distribution with k-ω turbulence model, with plate and boundary conditions of test(2) in table 5.8 (TRACE)

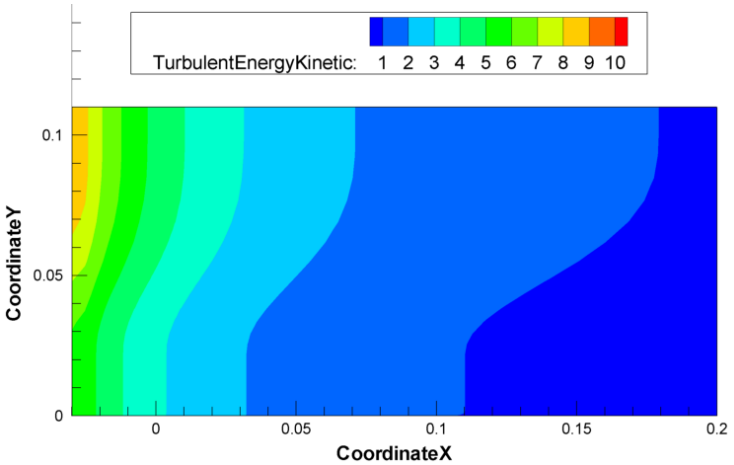

Figure 5.11: T3A: Turbulent kinetic energy distribution for a flow without plate and with k-ω turbulence model, boundary conditions of test(2) in table 5.8 (TRACE)

5.1.4 T3A Test Case Comparison LINARS and Fluent

Since both codes, LINARS and TRACE, produced such different results for the decay of the free stream turbulence intensity, we wanted to compare our results with those of another code. So a Fluent simulation was carried out. The Menter SST turbulence model and $\gamma - Re_\theta$ transition model with correlations by Langtry and Menter [2009] were used in the Fluent simulation. As shown in figure 5.12 Fluent confirms the distribution of the free stream turbulence as predicted by LINARS. It is interesting to see that the calculated skin friction coefficient in Fluent is very similar to the result of the LINARS code.

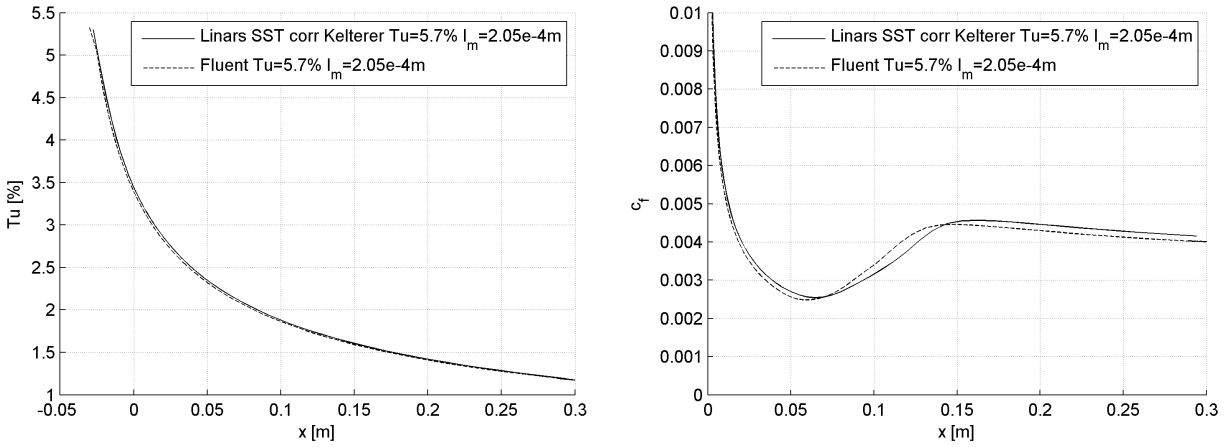

Figure 5.12: T3A: Free stream turbulence and skin friction coefficient with boundary conditions as in table 5.8 (2) (LINARS and Fluent)

5.1.5 T3A summary

The LINARS code produced good results for all correlations. It was only the Kelterer correlation that predicted the start of transition a bit too early. Generally we can say that correlations coupled with the $k-\omega$ turbulence model produce a shorter transition zone than those coupled with the Menter SST turbulence model. We were unable to fit the turbulence free stream intensity and the skin friction coefficient at the same time with TRACE. For some turbulence boundary conditions, TRACE produces an unrealistic distribution of the turbulent energy. It would appear that TRACE calculates the decay of turbulence differently than LINARS does. To validate the decay of the turbulence, a Fluent simulation was done, which gives similar results to that of the LINARS code.

5.2 T3C2 Test Case

The T3C2 test case is a flat plate test with an imposed pressure gradient. The Reynolds number for this test is $Re_l = 656000$. The characteristic length, the plate length, is $p_{plate} = 1.5\ m$. The start up length is $l_s = 0.2\ m$, the height reduces from $h_{gridmax} = 0.22\ m$ to $h_{gridmin} = 0.144\ m$ and enlarges up to $h_{gridout} = 0.177\ m$ to the outlet. The flow field is split in 260×80 cells. The density of the cells is highest near the wall in the boundary layer, at the transition zone between start up length and the beginning of the plate and also at the contour boundary for producing the pressure gradient.

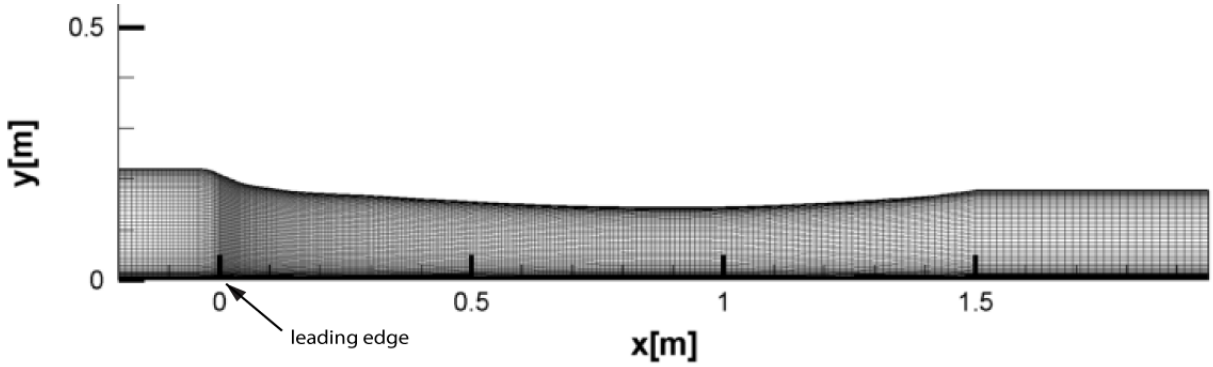

Figure 5.13: Grid of T3C2 test case

Measurements have shown that bypass transition occurs in a transition zone from $x_{trans} \approx 1 \div 1.3\ m$ or at a local Reynolds number between $Re_x \approx 500000 \div 620000$.

5.2.1 T3C2 Test Case with LINARS

To fit the Reynolds number in the LINARS calculation boundary conditions as given in table 5.9 were used. In order to fit the free stream turbulence to the measured data, turbulent boundary conditions as stated in table 5.10 were used.

Inlet	Outlet
$p_{tot} = 101634\ Pa$ $T_{tot} = 293.15\ K$	$p_{stat} = 95400\ Pa$
Global	
$l_{Plate} = 1.5\ m$ $\mu_{ref} = 2.69\ e-04\ kg/(s \cdot m)$	

Table 5.9: T3C2 LINARS parameters

Figure 5.14 shows the distribution of the turbulence intensity on the left hand side and the skin friction coefficient on the right hand side predicted by LINARS with all available models as given in table 4.1.

Inlet	
Turbulence Intensity = 0.06	Integral Turbulent Length Scale = 6.5e-04 m

Table 5.10: T3C2 LINARS inlet turbulence boundary conditions

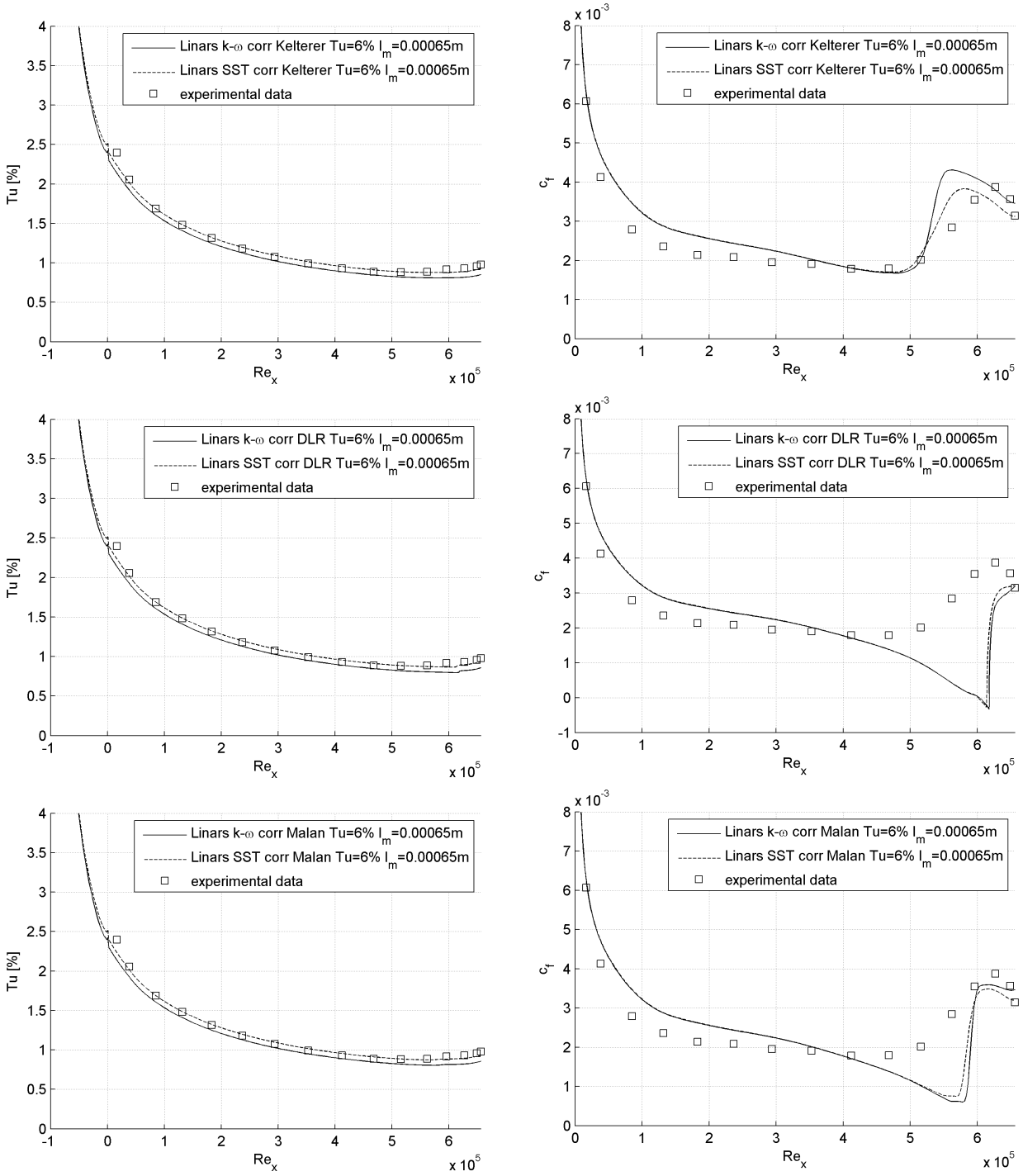

Figure 5.14: T3C2: Free stream turbulence and skin friction coefficient with different correlations of the transition model (LINARS)

The best results are achieved by LINARS with the SST turbulence model and the $\gamma - Re_\theta$ transition model with the correlations found by Kelterer. Here the transitional zone starts at $Re_x \approx 500000$, as expected, but fully developed turbulent flow is reached too early, at $Re_x \approx 580000$.
LINARS with DLR correlation predicts a separation bubble at the plate end ($c_f < 0$) and undergoes separation-induced transition. The results obtained with the Malan correlation are very similar to the results published by Malan et al. [2009]. Here, the transitional zone starts too late at $Re_x \approx 550000$ and the transitional zone is too short, but fully developed turbulent flow is reached at $Re_x \approx 600000$ as obtained from the experimental data.

5.2.2 T3C2 Test Case with TRACE

To fit the Reynolds number in the TRACE simulation the inlet and outlet pressure had to be adjusted. The boundary conditions used are given in table 5.11. Turbulent boundary conditions for this test are given in table 5.12. Since transition occurred too early, we varied the integral turbulent length scale.

Inlet	Outlet
$p_{tot} = 6980\ Pa$ $T_{tot} = 293.15\ K$	$p_{stat} = 6500\ Pa$
Global	
$l_{Plate} = 1.5\ m$	

Table 5.11: T3C2 TRACE parameters

Inlet	
Turbulence Intensity = 0.06	Integral Turbulent Length Scale = 6.5e-04 m
Turbulence Intensity = 0.06	Integral Turbulent Length Scale = 4.5e-04 m
Turbulence Intensity = 0.06	Integral Turbulent Length Scale = 1.0e-04 m

Table 5.12: T3C2 TRACE inlet turbulence boundary conditions

Figure 5.15 shows the free stream turbulence intensity on the left hand side and the skin friction coefficient on the right hand side calculated by TRACE with varying turbulent boundary conditions. For $l_m = 6.5e-4m$ and $l_m = 4.5e-4m$ the distribution of the free stream turbulence agrees with the experimental data but the transition happens too early. For $l_m = 1e-4m$ the turbulence intensity is too low and onset of transition is a little bit too late, the flow undergoes separation induced transition.

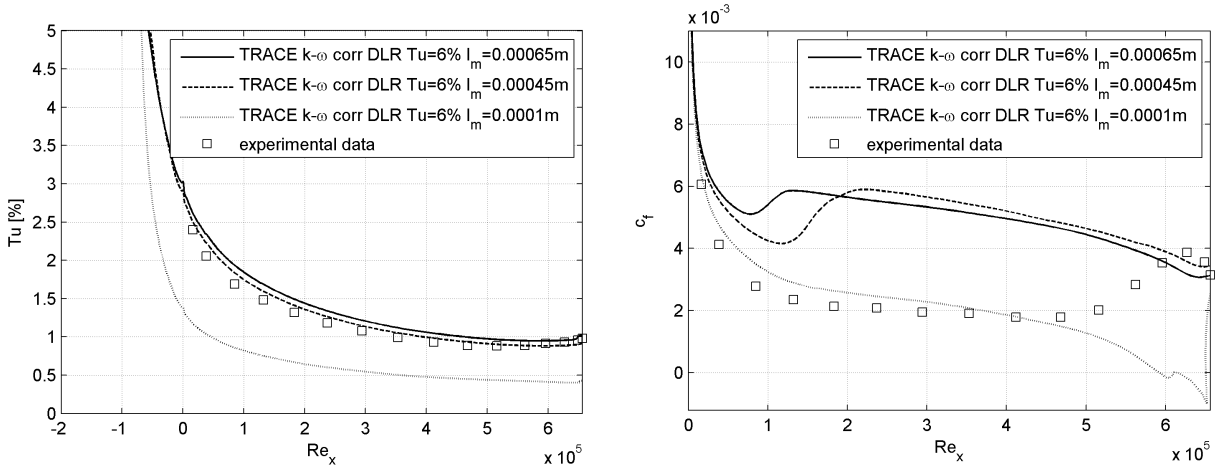

Figure 5.15: T3C2: Free stream turbulence and skin friction coefficient (TRACE)

5.2.3 T3C2 Summary

For this test case the best results are achieved by LINARS with the Kelterer correlation and SST turbulence model. The Malan and DLR correlations predict the onset of transition too far downstream. The DLR correlation even predicts separation-induced transition. With TRACE it was not possible to get a good match. Similar to the T3A test case, we were unable to fit both, the distribution of the turbulent intensity and the skin friction coefficient.

5.3 T3C4 Test Case

This test case uses the same grid as the T3C2 test case but with a lower Reynolds number, which leads to the development of a separation bubble at $x/l \approx 0.9$ or $Re_x \approx 170000$. The Reynolds number for this test case is $Re_l = 183800$.

5.3.1 T3C4 Test Case with LINARS

Table 5.13 states the parameter, found to fit the Reynolds number. In Table 5.14 the turbulent boundary conditions to match the free stream turbulence intensity to the experimental data are given.

Inlet	Outlet
$p_{tot} = 101634\ Pa$ $T_{tot} = 293.15\ K$	$p_{stat} = 95400\ Pa$
Global	
$l_{Plate} = 1.5\ m$ $\mu_{ref} = 9.7e-04\ kg/(s \cdot m)$	

Table 5.13: T3C4 LINARS parameters

Inlet	
Turbulence Intensity = 0.035	Integral Turbulent Length Scale = 1e-03 m

Table 5.14: T3C4 LINARS inlet turbulence boundary conditions

As seen in figure 5.16, where the free stream turbulence (left hand side) and the skin friction coefficient (right hand side) for several models are plotted, the LINARS code produced good results with the Kelterer and Malan correlation. Both predicted a separation bubble as expected. The separation bubble with the Malan correlation is slightly longer than the one calculated with the Kelterer correlation.
LINARS with DLR correlation did not fully converge. As a result, the distribution of the skin friction coefficient and the turbulence intensity at the end of the plate is unphysical. This is an indicator that the DLR correlation does not work very well in combination with the LINARS code.

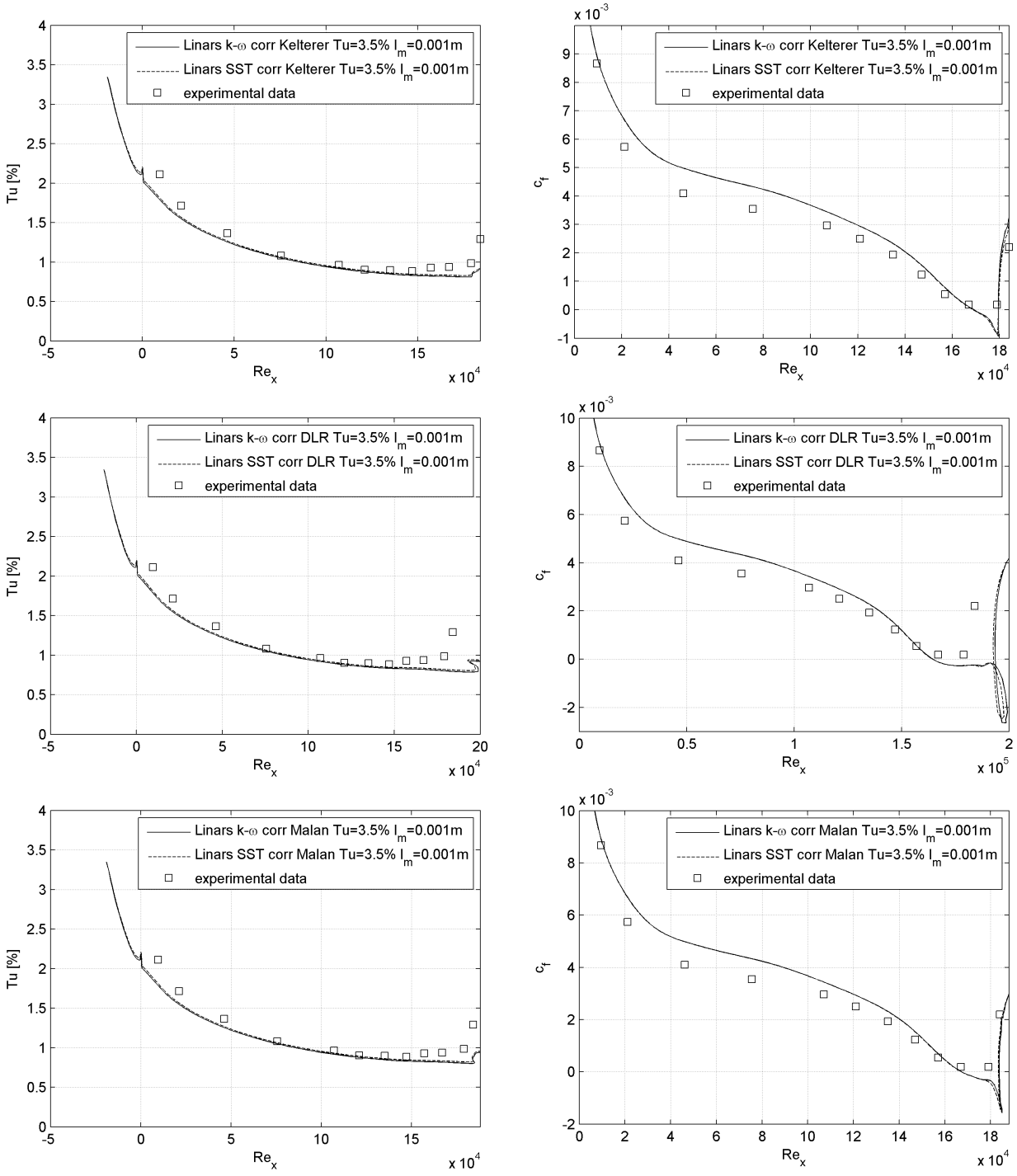

Figure 5.16: T3C4: Free stream turbulence and skin friction coefficient with various correlations of the transition model (LINARS)

5.3.2 T3C4 Test Case with TRACE

To fit the Reynolds number in the TRACE calculation, parameters as given in table 5.15 are used. The turbulent boundary conditions (see table 5.16) are the same as the ones used in LINARS.

Inlet	Outlet
$p_{tot} = 1940\ Pa$ $T_{tot} = 293.15\ K$	$p_{stat} = 1800\ Pa$
Global	
$l_{Plate} = 1.5\ m$	

Table 5.15: T3C4 TRACE parameters

Inlet	
Turbulence Intensity = 0.035	Integral Turbulent Length Scale = 1e-03 m

Table 5.16: T3C4 TRACE inlet turbulence boundary conditions

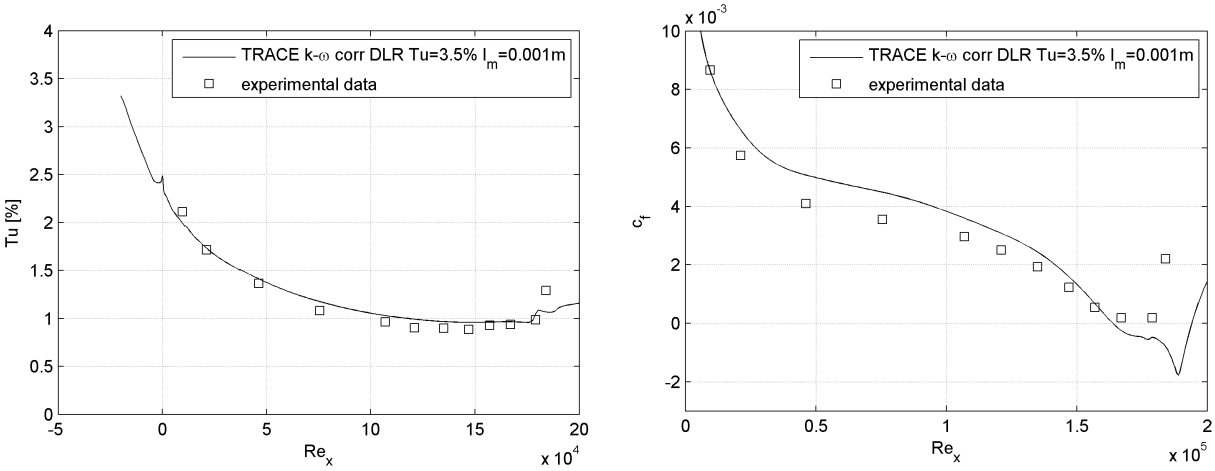

Figure 5.17: T3C4: Free stream turbulence and skin friction coefficient (TRACE)

As seen in figure 5.17, in this test case the free stream turbulence (left hand side) obtained from the simulation shows a good agreement with the experimental data. The skin friction coefficient (right hand side) is, as calculated by LINARS, slightly too high over a wide range. A separation bubble occurs, starting at $Re_x \approx 160000$ as expected, but the length of the bubble is about twice as long as estimated by experimental data.

5.3.3 T3C4 Summary

As in the T3C2 test case, the best results were obtained by LINARS with the Kelterer correlation, where the separation bubble shows a very good agreement with the experimental

data. The Malan correlation also produced good results, with a separation bubble that is slightly too long. For this test case, the DLR correlation did not work well with the LINARS code, giving unphysical results.
With TRACE this was the only test case in which it was possible to match the distribution of the turbulent intensity and the skin friction coefficient well. The predicted separation bubble is about twice as long as expected.

6 Cascade Test Cases

The correlations used in the LINARS code were obtained from flat plate test cases, so that it was unsurprising that the LINARS code produced better results for these test cases. Since the TRACE code is tuned for turbomachines, it is interesting to see its performance on cascade test cases.

Overview of the test cases

Table 6.1 gives an overview of the test cases and the applied transition models.

	T160				T106		
Reynolds number	90k	120k	200k	200k (3D)	150k	300k	500k
LINARS SST corr Kelteer LINARS $k-\omega$ corr Kelteer	x	x	x		x	x	x
LINARS SST corr DLR LINARS $k-\omega$ corr DLR	x	x	x		x	x	x
LINARS SST corr Malan LINARS $k-\omega$ corr Malan	x	x	x		x	x	x
TRACE	x	x	x	x			

Table 6.1: Cascade test overview of the test cases and applied transition models

6.1 T160 Test Case

The T160 turbine cascade represents a section of a low pressure turbine blade and was developed by the MTU Aero Engines GmbH. This profile features a strong fluid deflection, a moderate acceleration and a high blade pitch and is regularly used to validate Navier-Stokes calculations in order to enhance transition models.
The MTU kindly provided us with the mesh of this test case. In figure 6.1 the profile and grid is shown. Table 6.2 gives the design parameters. A definition of the geometrical dimensions is stated in figure 6.2.
In the experimental work, test series were carried out with different Mach and Reynolds numbers. [Staudacher and Homeier, 2003]
For the validation of our CFD codes, reference conditions of the test case as given in table 6.3 are used.

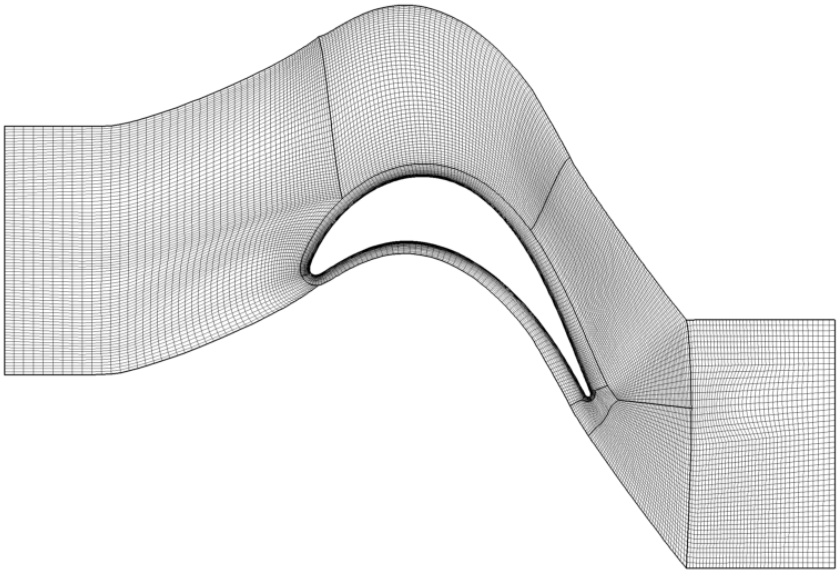

Figure 6.1: Grid of the T160 test case from MTU

T160 turbine cascade			
	t/l	=	0.8
angle of attack	β_1	=	131°
downstream flow angle	β_2	=	25°

Table 6.2: T160 design parameters

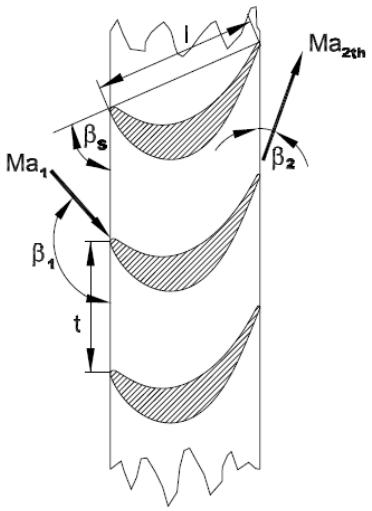

Figure 6.2: Definitions of the grid geometry [Staudacher and Homeier, 2003]

T160 steady references			
Reynolds number	Re_L	=	200000
Mach number	Ma_2	=	0.6

Table 6.3: T160 reference conditions for respective test case

In this test case two separation bubbles occur, one on the suction side between $x_{ax}/l_{ax} = 0.85 \div 0.92$ and one on the pressure side between $x_{ax}/l_{ax} = 0.05 \div 0.2$.
Figure 6.3 shows the definition of the measurement layer, e.g. index $_2$ corresponds to the measurement layer ME0.4 (see figure 6.3), where most measurements were done. The

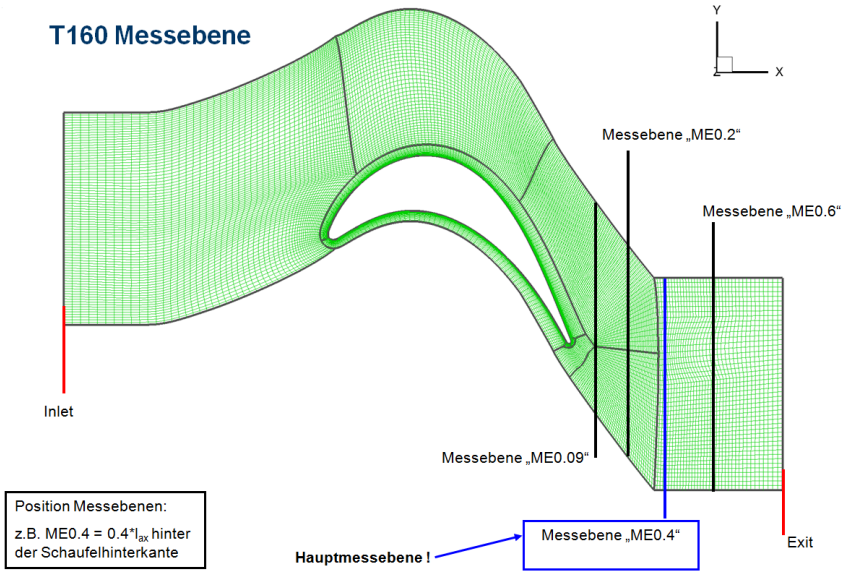

Figure 6.3: T160 definition of the measurement planes [Staudacher and Homeier, 2003]

simulations with LINARS and TRACE were done with the fluid conditions of table 6.3. The turbulent boundary conditions of test(2) in table 6.4 are used by the DLR for this test case. Varying turbulent inlet boundary conditions are used to study the sensitivity of the transition models.

Inlet turbulent boundary conditions					
Test (1)	T_u	=	1.5 %	l_m	= 0.00018 m
Test (2)	T_u	=	3.7 %	l_m	= 0.00018 m
Test (3)	T_u	=	8.0 %	l_m	= 0.00018 m
Test (4)	T_u	=	3.7 %	l_m	= 0.00005 m
Test (5)	T_u	=	3.7 %	l_m	= 0.0005 m
Test (6)	T_u	=	3.7 %	l_m	= 0.001 m
Test (7)	T_u	=	3.7 %	l_m	= 0.002 m

Table 6.4: T160 varying turbulent inlet boundary conditions

Since the T160 test case is very demanding in terms of computational effort, a detailed study with all variations of the turbulent boundary conditions is only made for LINARS with the Kelterer correlation and for TRACE.
Here, the pressure coefficient is defined as

$$c_p = \frac{p_{wall\ local} - p_2}{p_{tot\ inlet} - p_2} \tag{6.1}$$

where the subscript $_2$ stands for the averaged value at the measurement layer ME0.4. To analyze the wake effect a local pressure loss coefficient is calculated as

$$\zeta_l = \frac{p_{tot1} - p_{tot2}}{q_2} \tag{6.2}$$

$$q_2 = p_{tot1} - (p_{2\ local} - p_{2\ min}) \tag{6.3}$$

where $p_{2\ min}$ is the minimum pressure in the measurement layer ME0.4. A maximum of the local pressure loss coefficient is reached when the local pressure in measurement layer ME0.4 $p_{2\ local}$ reaches the minimum (where $p_{2\ local} = p_{2\ min}$).
The total pressure loss coefficient is given as

$$\zeta = \frac{p_{tot1} - p_{tot2}}{\overline{q_2}} \tag{6.4}$$

where $\overline{q_2}$ is the averaged value of q_2.

6.1.1 T160 Test Case with LINARS, Kelterer correlation

In order to obtain the same Reynolds and Mach number, the boundary conditions had to be adjusted to match the conditions as given in table 6.3.

Inlet	Outlet
$p_{tot} = 27041\ Pa$ $T_{tot} = 303.15\ K$	$p_{stat} = 21192.9\ Pa$
Global	
$\mu = 1.7269e-05\ kg/(s \cdot m)$	

Table 6.5: T160 LINARS parameters

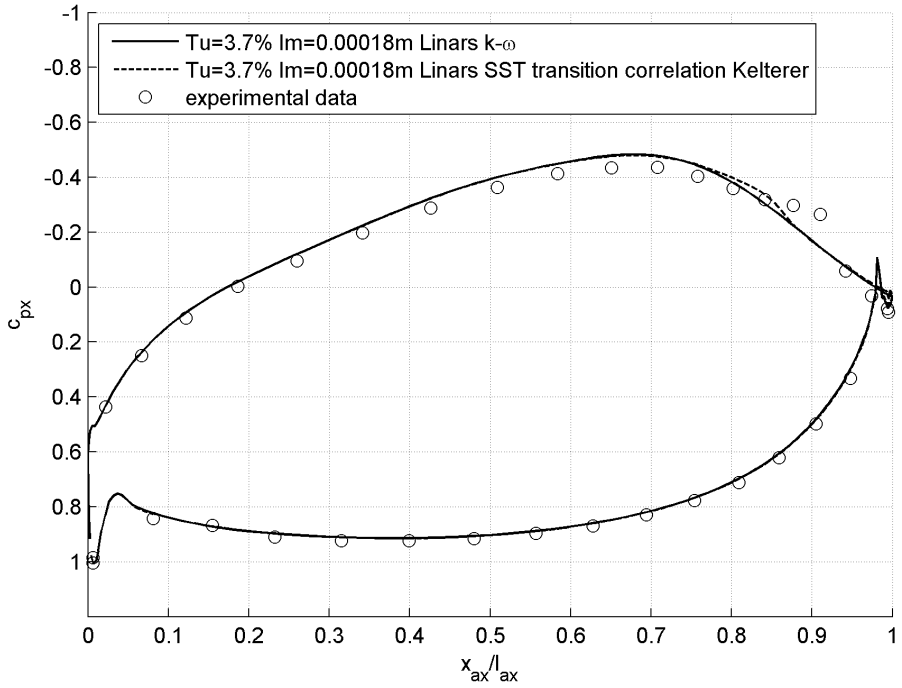

Figure 6.4: T160: Pressure coefficient comparison between pure turbulence model and transition model with Kelterer correlation (LINARS)

Figure 6.4 shows the difference of the pressure coefficient between a calculating with a pure turbulence model and with transition model. The results of both models match, except for the region of transition on the suction side. For the skin friction coefficient, see figure 6.5, the difference between pure turbulent and transition model is sigificant on the suction side. Transition onset occurs at $x_{ax}/l_{ax} \approx 0.85$ and undergoes bypass transition. The flow becomes fully turbulent and thus the skin friction coefficient of the turbulent and the transition model match. On the pressure side, the skin friction coefficient for both models becomes $c_f < 0$ at $x_{ax}/l_{ax} = 0.05 \div 0.2$, which indicates a separation bubble (see figure 6.5). Figure 6.6 shows the wake. Here, u is a coordinate parallel to the outlet in the measurement layer ME0.4. On the pressure side, the wake develops too late and increases sharper than measured. The overshoot of the wake is more significant for the pure turbulence model.

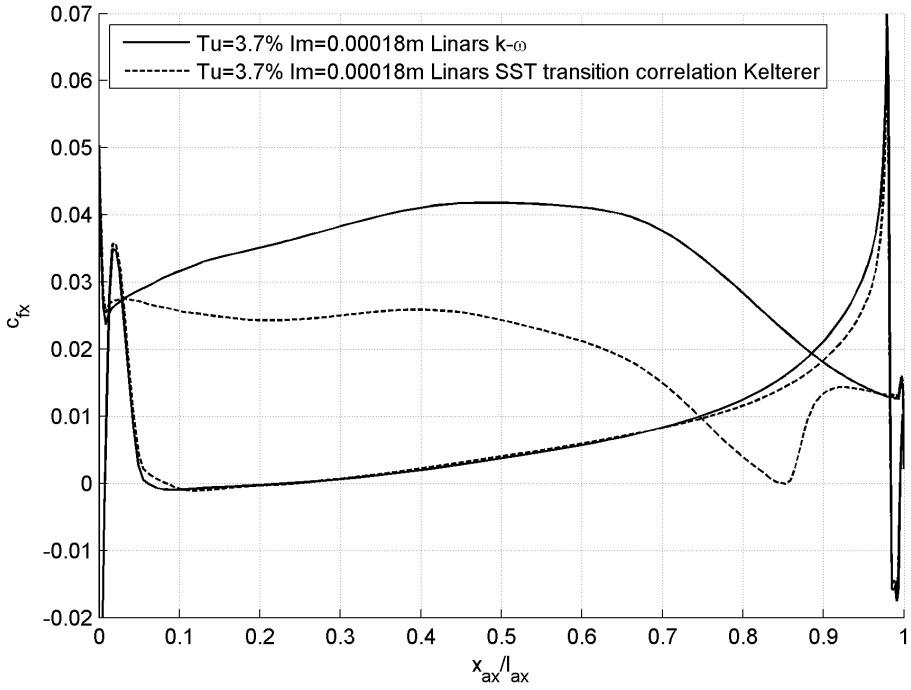

Figure 6.5: T160: Skin friction coefficient comparison between pure turbulence model and transition model with Kelterer correlation (LINARS)

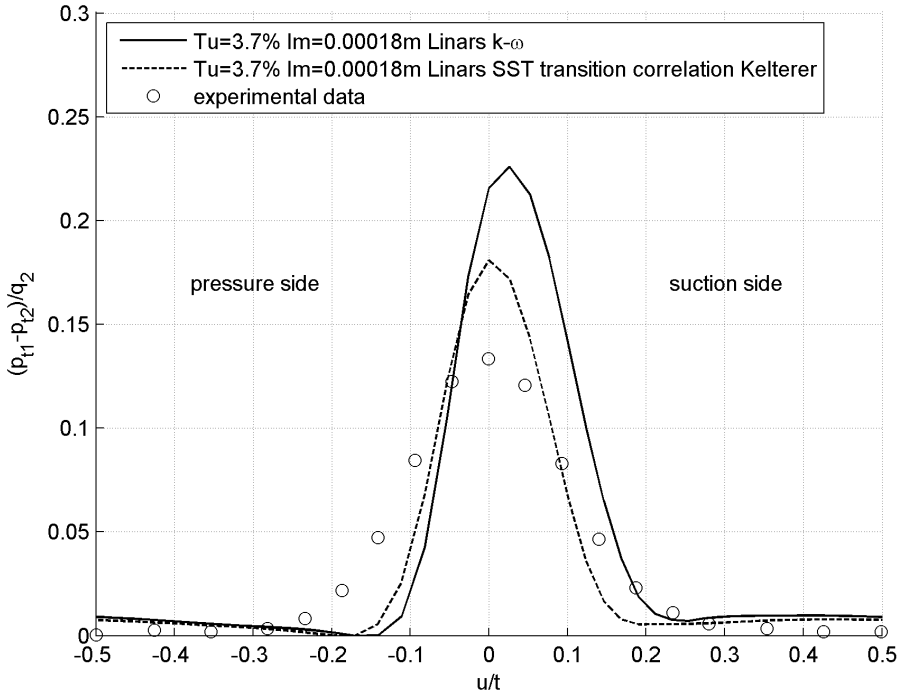

Figure 6.6: T160: Local pressure loss coefficient in measurement layer ME0.4, comparison between pure turbulence model and transition model with Kelterer correlation (LINARS)

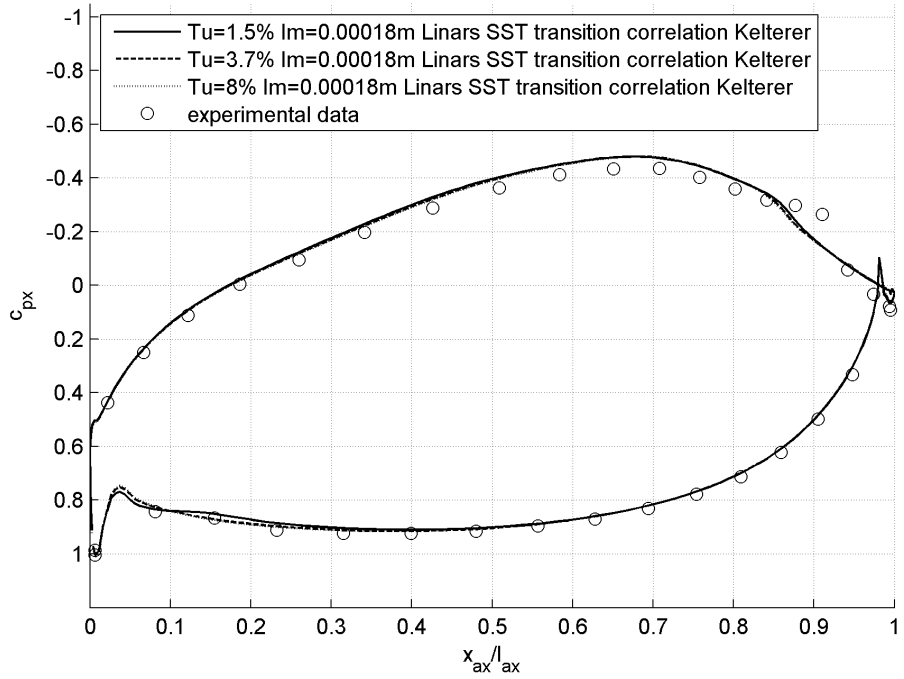

Figure 6.7: T160: Pressure coefficient for various Tu levels and fixed l_m with Kelterer correlation (LINARS)

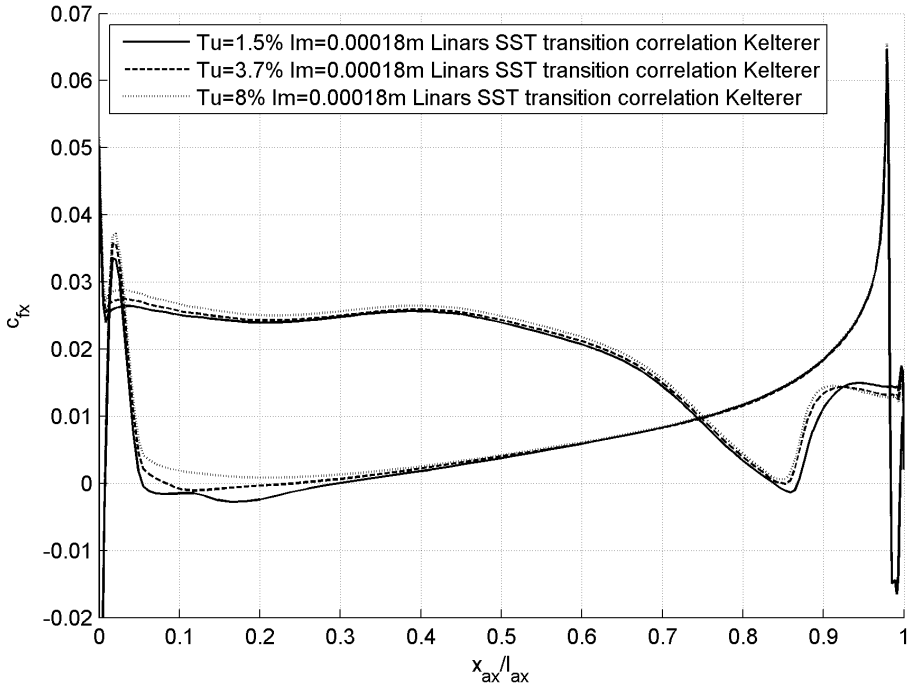

Figure 6.8: T160: Skin friction coefficient for various Tu levels and fixed l_m with Kelterer correlation (LINARS)

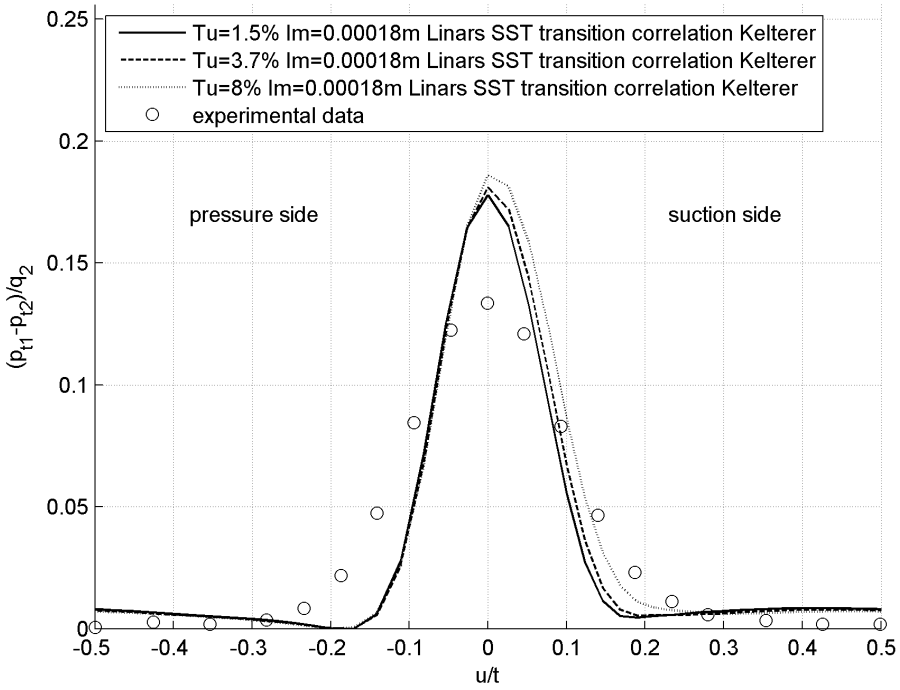

Figure 6.9: T160: Local pressure loss coefficient in measurement layer ME0.4 for various Tu levels and fixed l_m with Kelterer correlation (LINARS)

When varying the turbulence intensity we expect a change of the transition onset location on the suction side. A lower turbulence intensity should lead to a shift downstream (see equation 5.3). Although the onset of transition changed only marginally, this physical relation is shown correctly. With the lowest inlet turbulence intensity $T_u = 1.5\%$ a separation bubble is predicted on the suction side. On the pressure side a small separation bubble with $T_u = 3.7\%$ and a larger separation bubble with $T_u = 1.5\%$ developed (see figure 6.8). The wake grows slightly with a higher turbulence intensity (see figure 6.9).

Also, when varying the mixing length, the change in the transition onset is minimal. Only with the smallest imposed mixing length $l_m = 5e-5\ m$ a separation bubble developed at the suction and pressure side (see figure 6.11). The distribution of the pressure coefficient hardly changes when varying the turbulence intensity or mixing length (see figure 6.7 and 6.10). Here, the most significant change is the lower pressure coefficient along the suction side with a rising mixing length. However the wake and thus the local pressure loss in the measurement layer spreads as the mixing length grows (see figure 6.12), which has a significant influence on the total pressure loss. The total pressure loss of all the test cases is given in table 6.7.

The spread of the wake grows towards the suction side. It is interesting to discuss the reason for this behavior. Our first guess was that the boundary layer grows as the mixing length increases. As can be seen in figure 6.13, this is not the case, but what happens is, that a larger mixing length leads to higher losses and thus a lower velocity on the suction side, causing the wake spread towards the suction side.

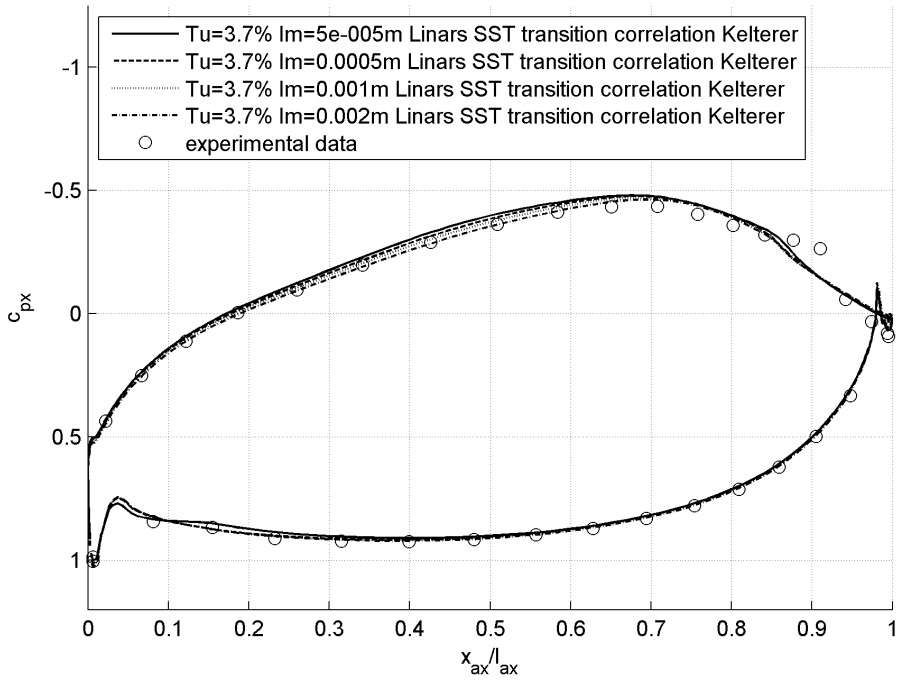

Figure 6.10: T160: Pressure coefficient for various l_m levels and fixed Tu with Kelterer correlation (LINARS)

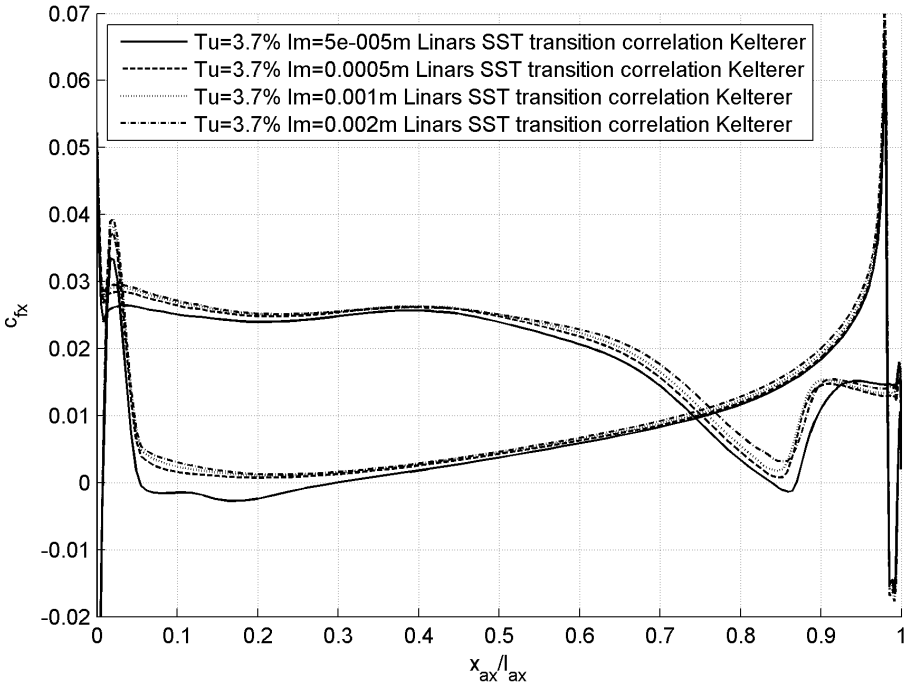

Figure 6.11: T160: Skin friction coefficient for various l_m levels and fixed Tu with Kelterer correlation (LINARS)

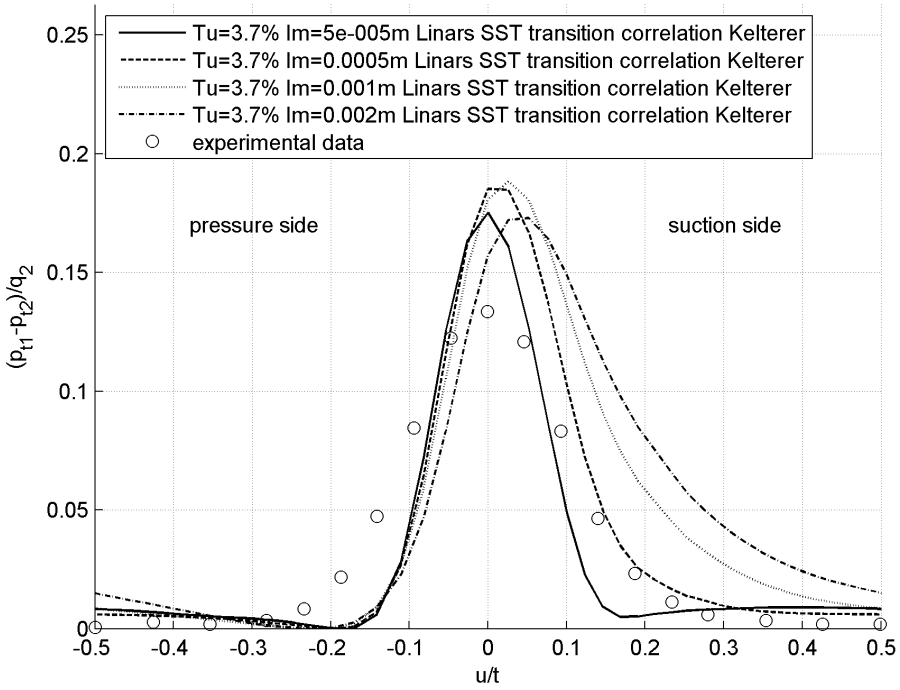

Figure 6.12: T160: Local pressure loss coefficient in measurement layer ME0.4 for various l_m levels and fixed Tu with Kelterer correlation (LINARS)

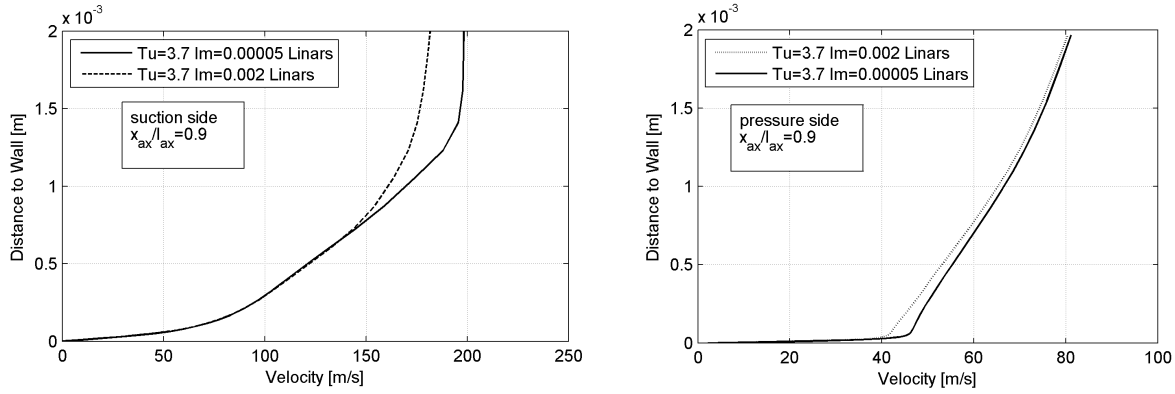

Figure 6.13: T160: Velocity in boundary layer for test(4) and test(7) with Kelterer correlation (LINARS)

6.1.2 T160 Test Case with LINARS, DLR correlation

LINARS with DLR correlation produces very good results for the pressure coefficient distribution with boundary conditions as given in table 6.4 test(2). The flow undergoes a separation-induced transition, with a separation bubble starting at $x_{ax}/l_{ax} \approx 0.82$ and disappears at $x_{ax}/l_{ax} \approx 0.91$. The pressure coefficient drops at $x_{ax}/l_{ax} \approx 0.88$, which is slightly too early, but still corresponds with the experimental data (see figure 6.14 and 6.15).
The peak in the pressure coefficient distribution in the measurement layer is slightly higher than expected with a delayed but sharper rise on the pressure side and still agrees with the experimental data (see figure 6.16).

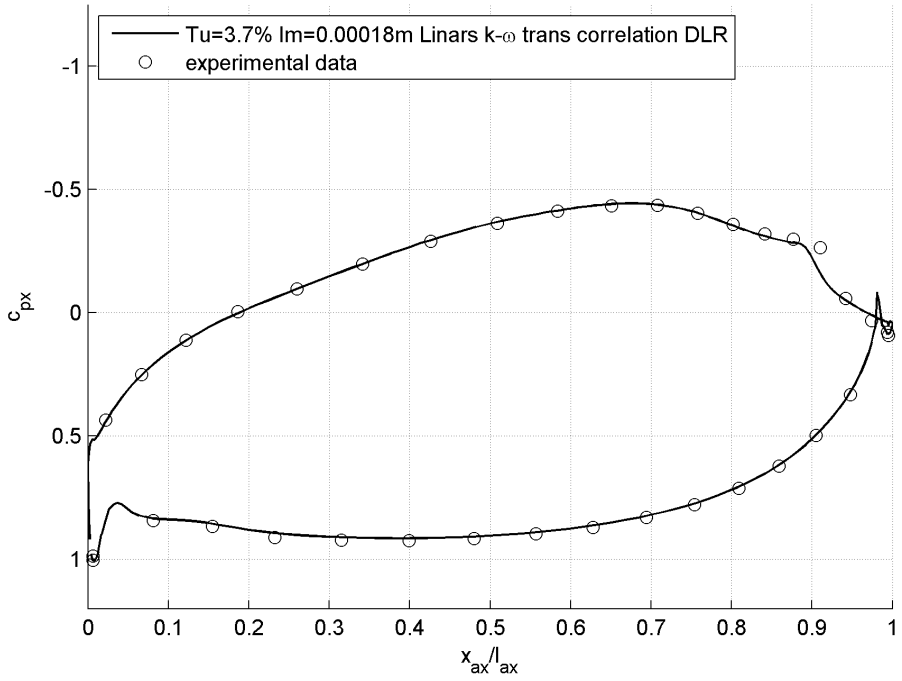

Figure 6.14: T160: Pressure coefficient with DLR correlation (LINARS)

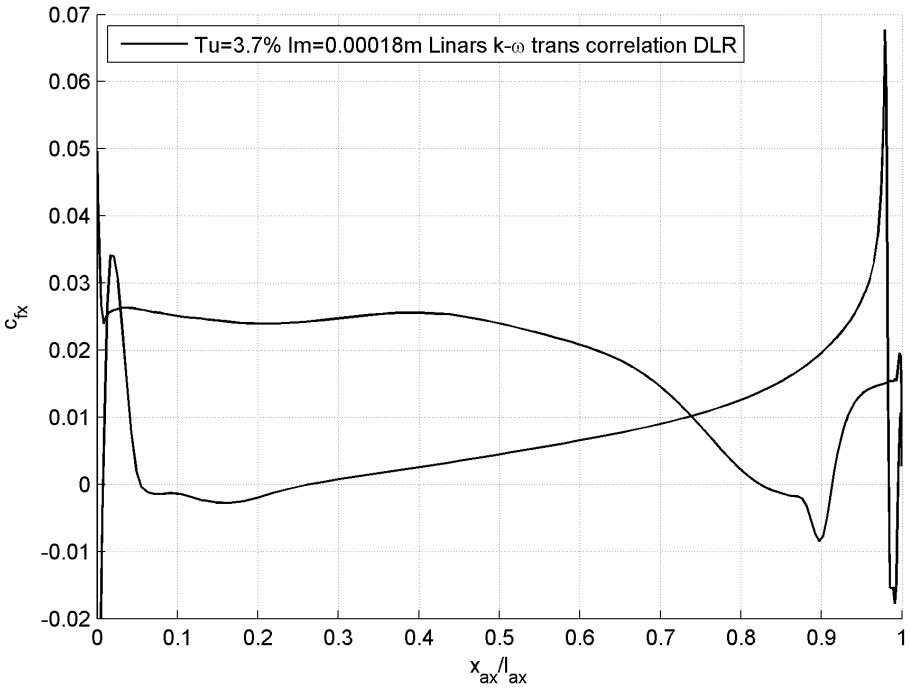

Figure 6.15: T160: Skin friction coefficient with DLR correlation (LINARS)

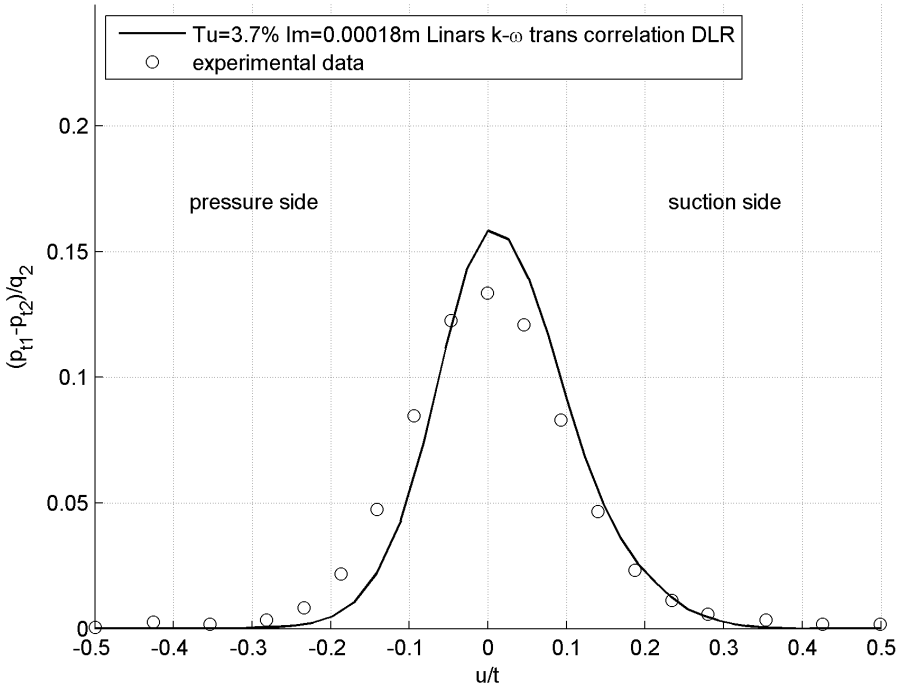

Figure 6.16: T160: Local pressure loss coefficient in measurement layer ME0.4 with DLR correlation (LINARS)

6.1.3 T160 Test Case with LINARS, Malan correlation

In order to get a separation bubble with this configuration a very small mixing length had to be set. When comparing the results of the pressure coefficient and skin friction coefficient in figure 6.17 and 6.18 with turbulent boundary conditions as in table 6.4 test(2) and test(4) we can see that the sensitivity to the mixing length is higher than for the Kelterer correlation. The pressure drop though occurs too early, thus the separation bubble is too short.

The peak of the pressure coefficient distribution in the measurement layer ME0.4 is higher than measured (figure 6.19) with a sharper rise on the pressure and suction side.

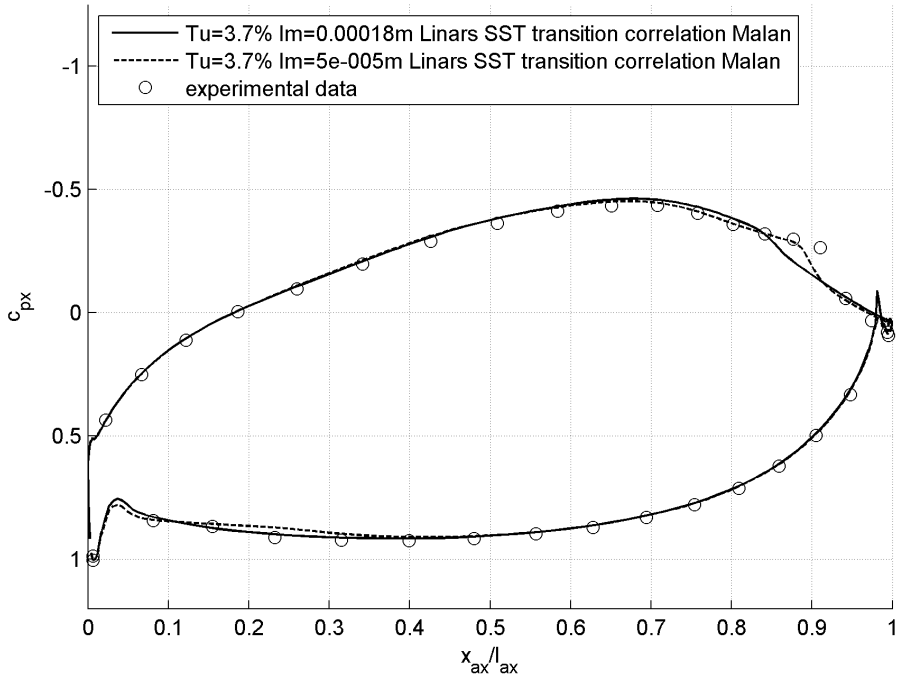

Figure 6.17: T160: Pressure coefficient with Malan correlation (LINARS)

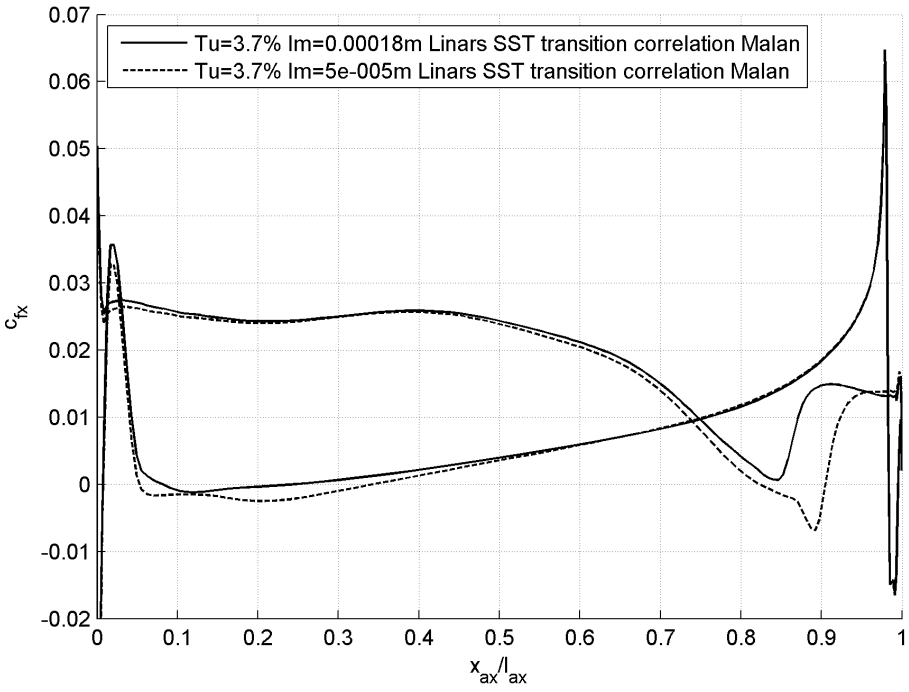

Figure 6.18: T160: Skin friction coefficient with Malan correlation (LINARS)

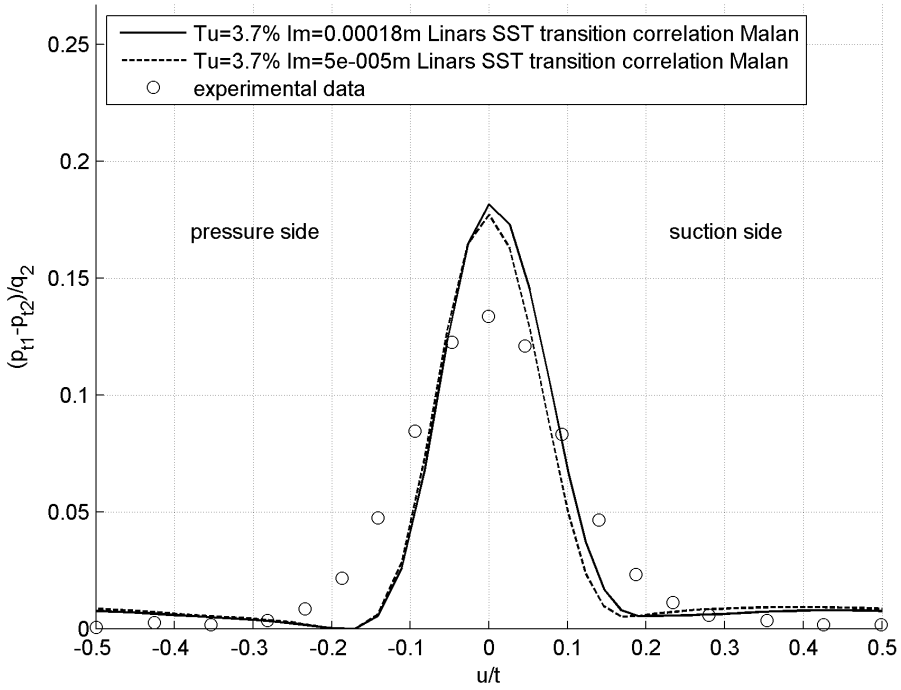

Figure 6.19: T160: Local pressure loss coefficient in measurement layer ME0.4 with Malan correlation (LINARS)

6.1.4 T160 Test Case with TRACE

To achieve Reynolds and Mach number similarity in TRACE, boundary conditions as given in Table 6.6 are used.

Inlet	Outlet
$p_{tot} = 27041\ Pa$ $T_{tot} = 303.15\ K$	$p_{stat} = 21197\ Pa$

Table 6.6: T160 TRACE parameters

With the enabled transition model in TRACE the pressure coefficient corresponds well with the experimental data. The onset of transition is correctly predicted. A flat pressure profile indicates a separation bubble in figure 6.20 at $x_{ax}/l_{ax} = 0.85 \div 0.92$. The distribution of the skin friction coefficient as given in figure 6.21 shows a distinct difference between pure turbulence and transition model on the suction side. The skin friction coefficient, thus the predicted pressure losses of the blades are much higher with the pure turbulence model. This shows, once again, the importance of a good transition model for turbomachines. With the enabled transition model a separation bubble also occurs on the pressure side (see figure 6.21). The overshoot of the wake depression as seen in figure 6.22 is less distinct than with the pure turbulence model and corresponds well with the experimental data.
A decreased turbulence intensity leads to a downstream shift of the transition onset as expected. This trend is more distinctive in TRACE than in LINARS. A high turbulence intensity leads to a much earlier onset of transition and thus suppresses the formation of a

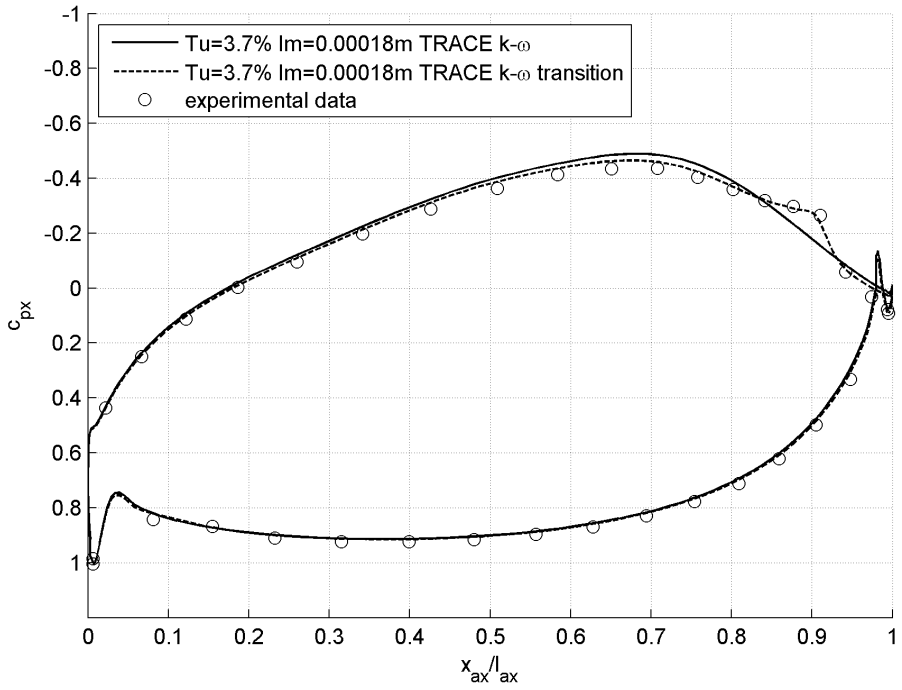

Figure 6.20: T160: Pressure coefficient comparison between pure turbulence model and transition model (TRACE)

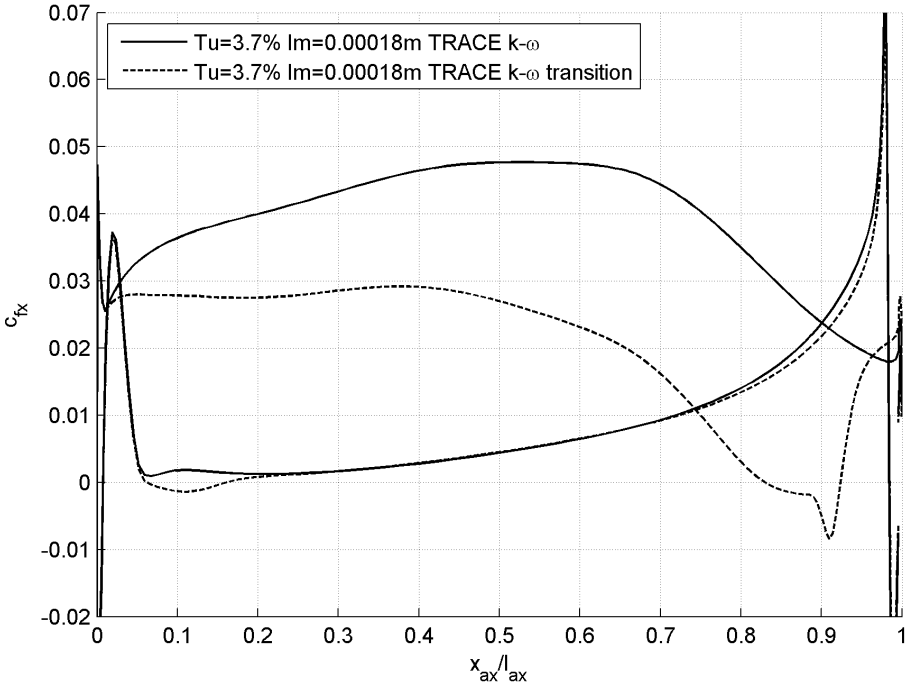

Figure 6.21: T160: Skin friction coefficient comparison between pure turbulence model and transition model (TRACE)

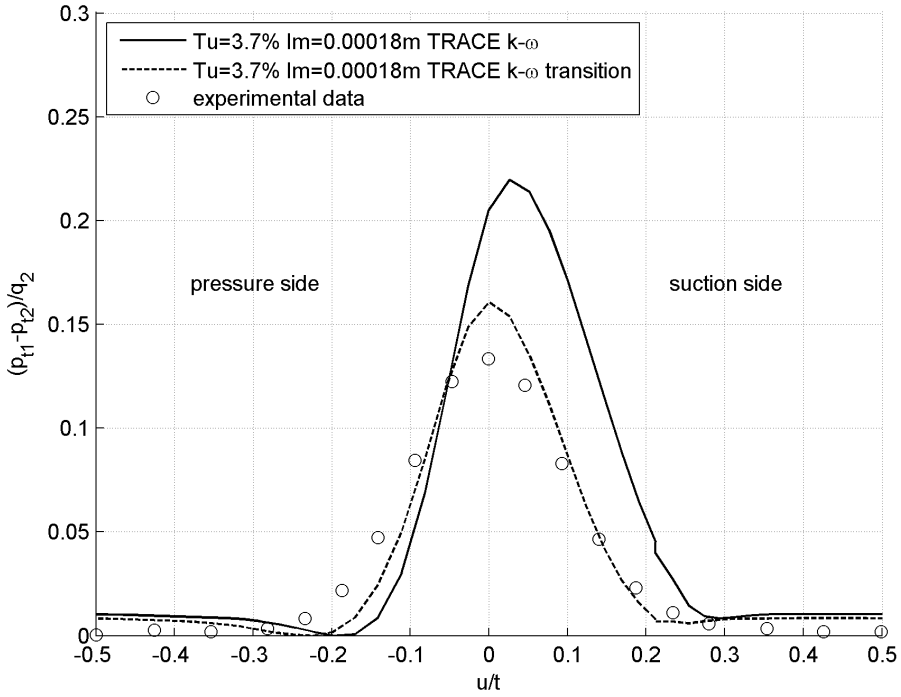

Figure 6.22: T160: Local pressure loss coefficient in measurement layer ME0.4, comparison between pure turbulence model and transition model (TRACE)

bubble (see figure 6.24). This can also be seen in figure 6.23, where the pressure coefficient distribution for a higher inlet turbulence intensity does not form a plateau. Also, the wake is more distinctive at a high turbulence intensity (see figure 6.25), which leads to higher losses (see table 6.7).

Varying the mixing length brings almost the same results. A smaller mixing length delays the transition onset as expected (see figure 6.26). For higher values, the transition onset occurs much earlier, leading to an increased skin friction coefficient on the suction side (see figure 6.27) and greater losses, as can be seen in the rise of the pressure coefficient distribution in the measurement layer (see figure 6.28) and total pressure loss (table 6.7).

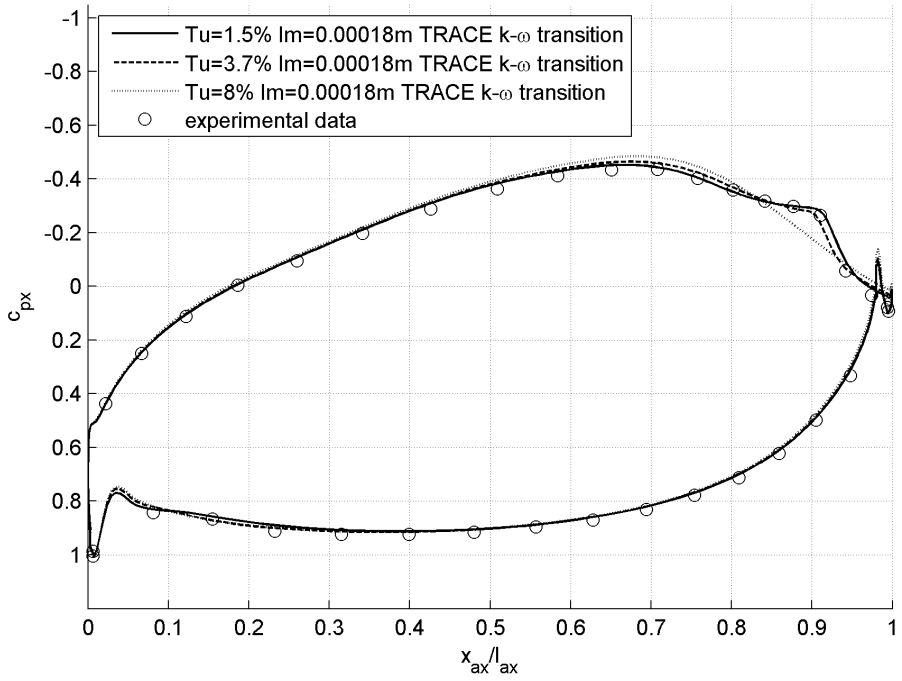

Figure 6.23: T160: Pressure coefficient for various Tu levels and fixed l_m (TRACE)

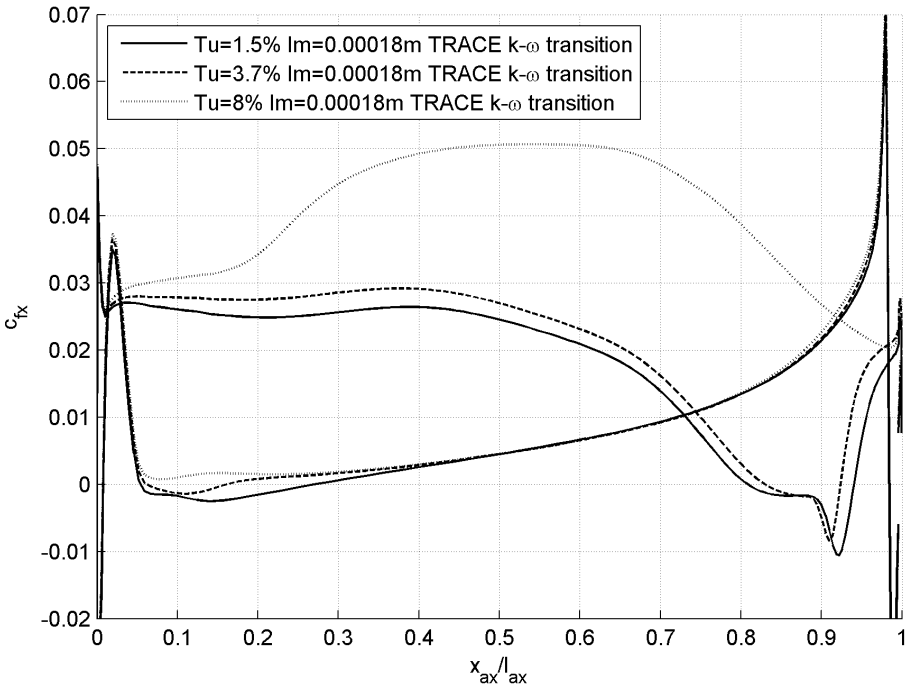

Figure 6.24: T160: Skin friction coefficient for various Tu levels and fixed l_m (TRACE)

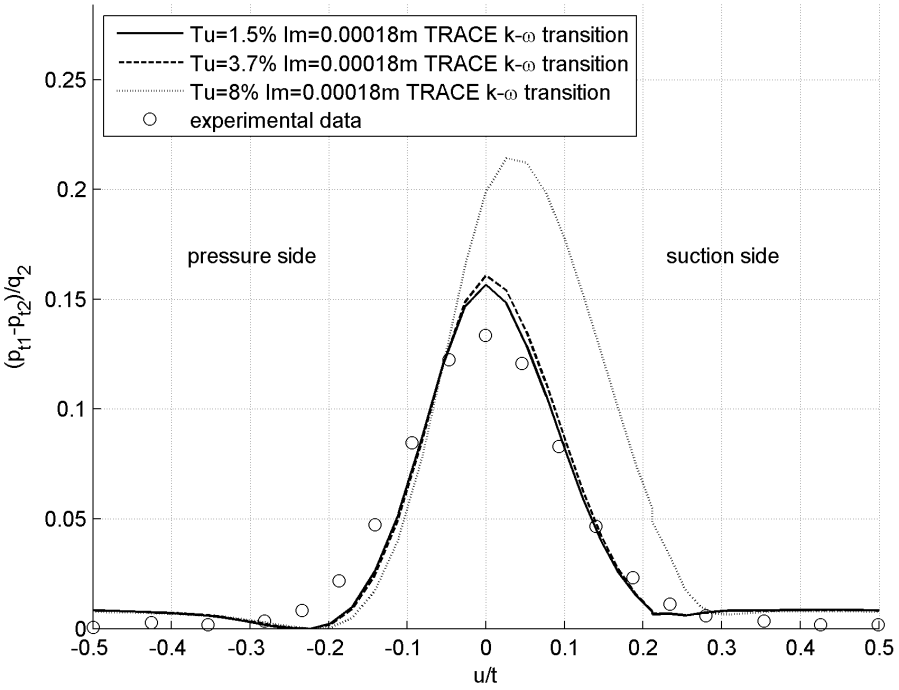

Figure 6.25: T160: Local pressure loss coefficient in measurement layer ME0.4 for various Tu levels and fixed l_m (TRACE)

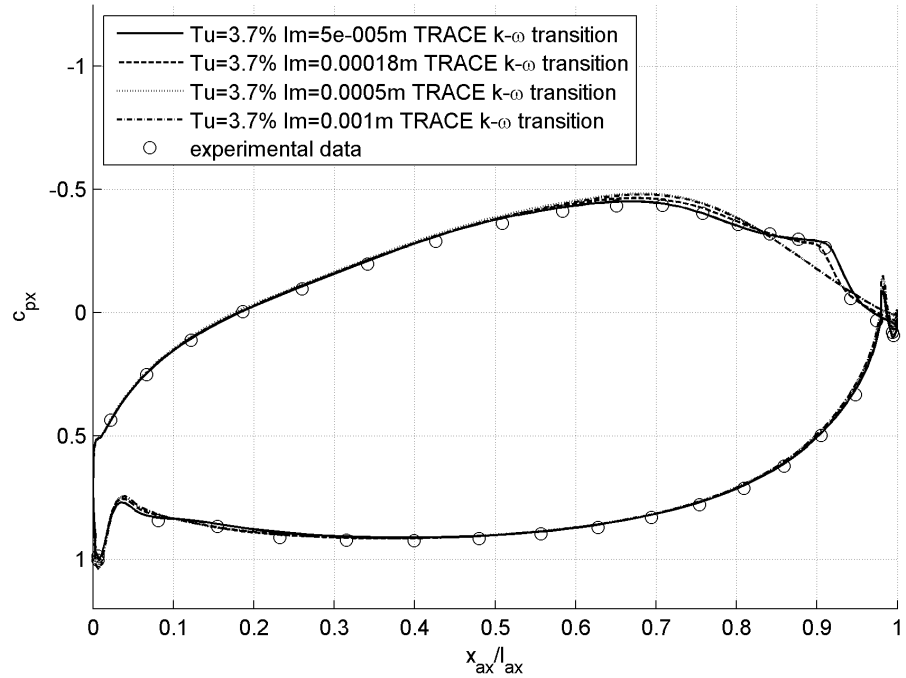

Figure 6.26: T160: Pressure coefficient for various l_m levels and fixed Tu (TRACE)

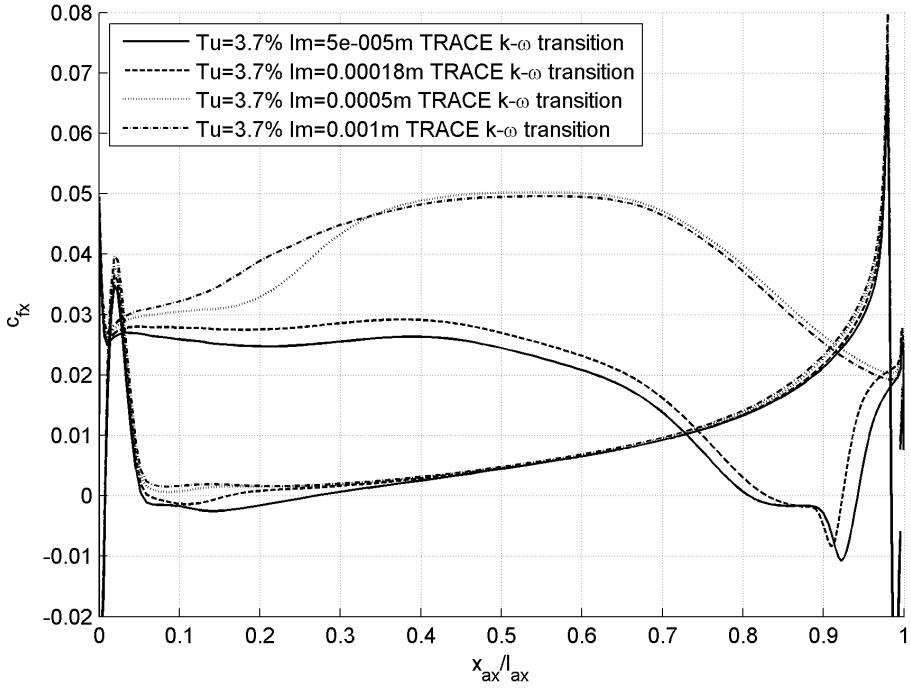

Figure 6.27: T160: Skin friction coefficient for various l_m levels and fixed Tu (TRACE)

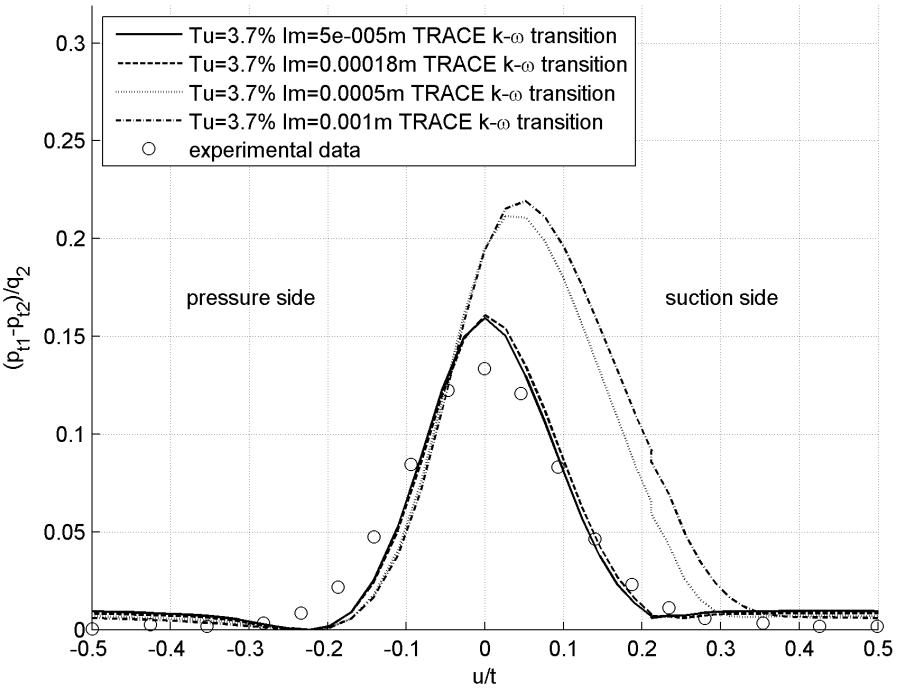

Figure 6.28: T160: Local pressure loss coefficient in measurement layer ME0.4 for various l_m levels and fixed Tu (TRACE)

The total pressure loss of LINARS with Kelterer correlation and TRACE (tabe 6.7) shows a high bandwidth for different turbulent boundary conditions (table 6.4). In general, the losses for TRACE are higher. That is because TRACE predicts a larger separation bubble which leads to higher losses. It can be seen, that a larger separation bubble leads to higher losses. The measurements of the MTU were done with a inlet turbulence intensity of 4.2 %, but the mixing length is not know, so that it is not possible to argue which model performs better.

			LINARS trans corr Kelterer	TRACE trans corr Malan
	Tu	lm [m]	ζ [%]	
Test (1)	1.5	1.8e-4	2.55	2.92
Test (2)	3.7	1.8e-4	2.64	2.99
Test (3)	8.0	1.8e-4	2.89	4.63
Test (4)	3.7	5e-5	2.52	2.97
Test (5)	3.7	5e-4	3.2	4.72
Test (6)	3.7	1e-3	4.2	5.26
Test (7)	3.7	2e-3	4.73	6.4
Measurement MTU			3.2	

Table 6.7: T160 comparison of the total pressure loss coefficient ζ

6.1.5 Reynolds number variation

In the following section the different models are compared directly for the same turbulent boundary conditions and varying Reynolds numbers ($Re = 120000$ and $Re = 90000$).
We will see that both LINARS transition models based on the SST turbulence model (correlation Kelterer and Malan) produce similar results of the pressure and skin friction coefficient distribution while the LINARS transition model based on the $k - \omega$ turbulence model (correlation DLR) produces results similar to the TRACE code, which also uses a transition model based on the $k - \omega$ turbulence model. Please note, the overview of the implied models and their underlying correlations in table 4.1 and notice that TRACE uses the same models as LINARS with DLR transition correlation.
In light of the above, one should not be surprised to obtain similar results with TRACE and LINARS for the DLR transition correlations. But considering that the main conclusion of the T3A test case, which is that the TRACE code calculates the decay of turbulence intensity more differently than the LINARS code (even with the same turbulence model), this result is remarkable.

Re 120000

Figure 6.29 shows the distribution of the pressure coefficient. In figure 6.30 the transitional zone on the suction side is shown in detail. As stated previously, the same combination of turbulence and transition model gives similar results. This also holds true for the distribution of the skin friction coefficient, shown in figure 6.31. The details in the transitional zone are shown in figure 6.32. The wake depression (see figure 6.33) is similar for all LINARS calculations. The overshoot is more distinct for this code and less distinct in the TRACE code. All codes predict a late and sharp rise of the wake depression on the pressure side.

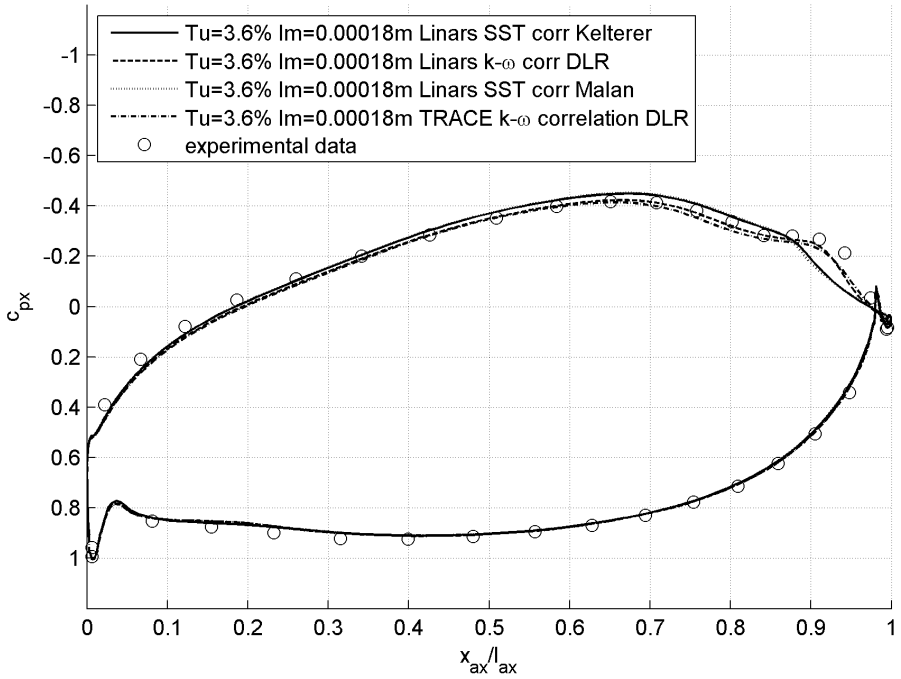

Figure 6.29: T160: Pressure coefficient comparison between different correlations for Re = 120000 (LINARS and TRACE)

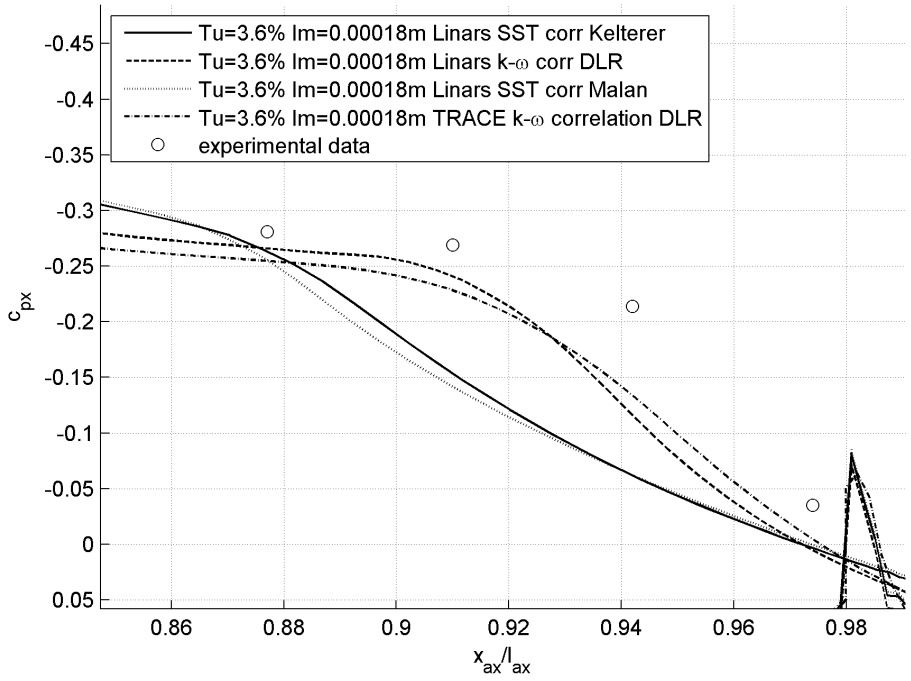

Figure 6.30: T160: Pressure coefficient comparison between different correlations for Re = 120000 (LINARS and TRACE) (zoomed)

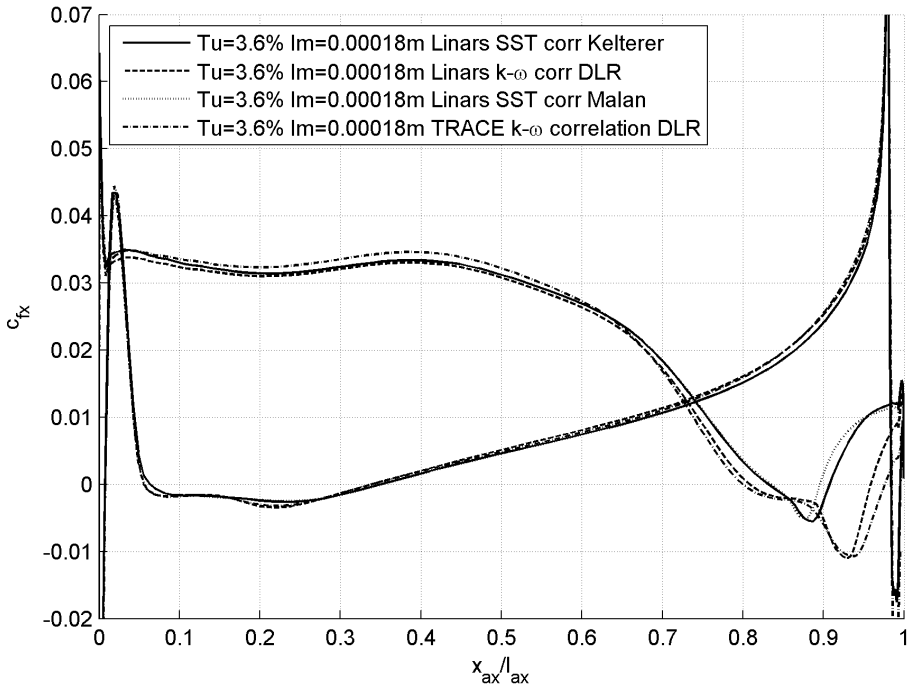

Figure 6.31: T160: Skin friction coefficient comparison between different correlations for Re = 120000 (LINARS and TRACE)

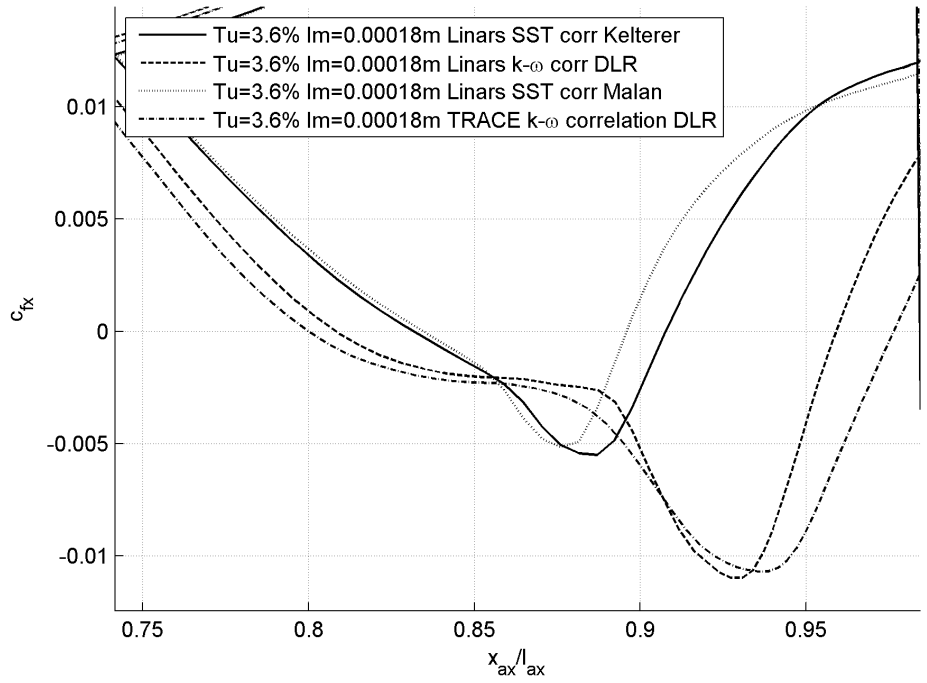

Figure 6.32: T160: Skin friction coefficient comparison between different correlations for Re = 120000 (LINARS and TRACE) (zoomed)

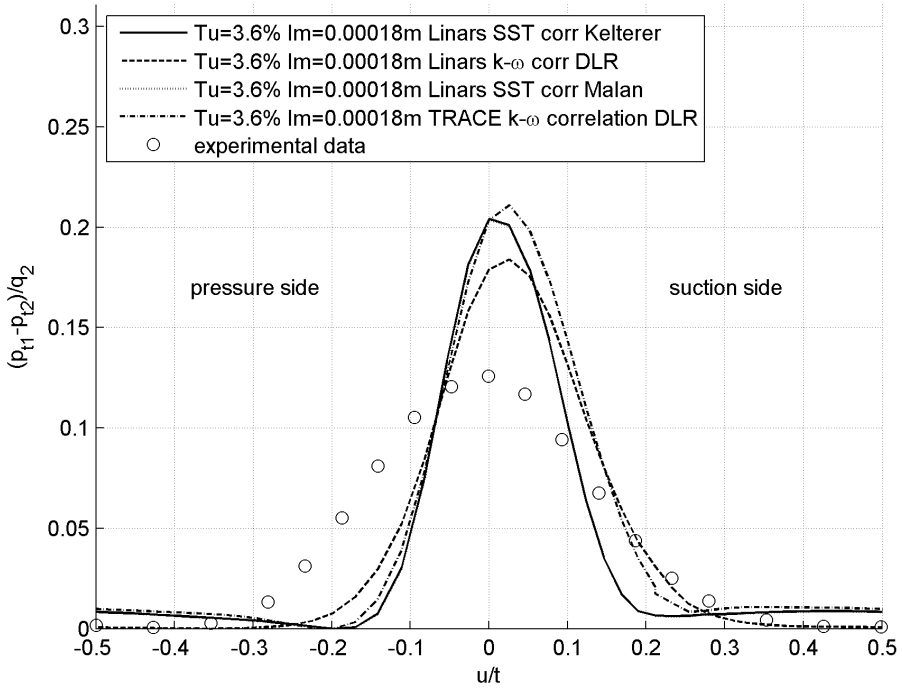

Figure 6.33: T160: Local pressure loss coefficient comparison between different correlations for Re = 120000 (LINARS and TRACE)

Re 90000

As previously stated, the direct comparison of different codes shows that *LINARS SST corr Kelterer* and *Linars SST corr Malan* as well as *LINARS $k-\omega$ corr DLR* and *TRACE* obtain similar results considering the beginning and length of the transition zone (similar pressure plateau and pressure drop in figure 6.34 and more detailed figure 6.35) as well as similar skin friction distribution in figure 6.36 and more detailed figure 6.37.

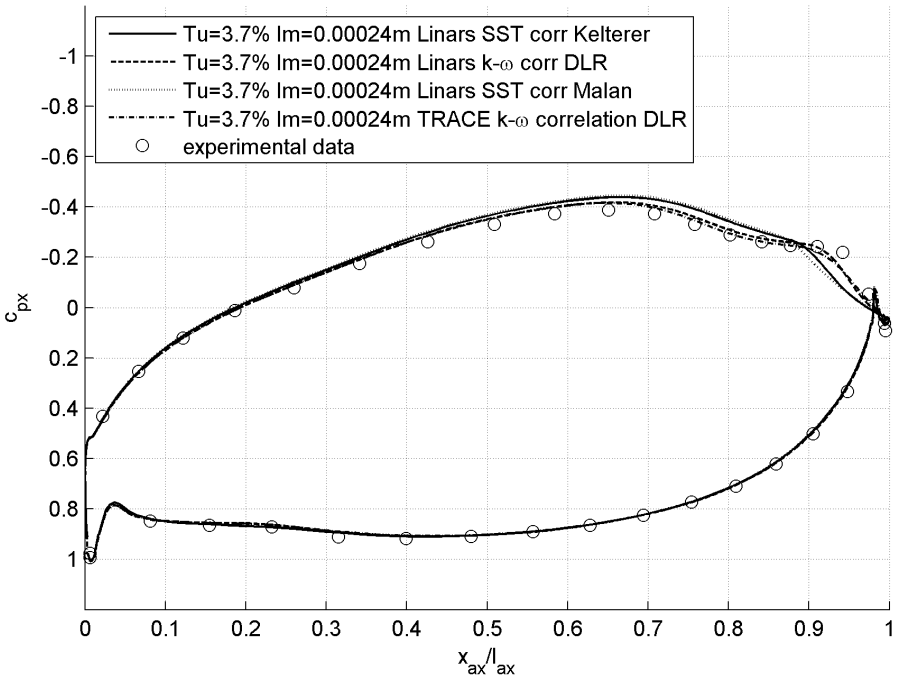

Figure 6.34: T160: Pressure coefficient comparison between different correlations for Re = 90000 (LINARS and TRACE)

The difference between *LINARS SST corr Kelterer* and *Linars SST corr Malan* is that the Malan correlation is more sensitive to turbulent boundary conditions. Therefore it's possible to match the pressure coefficient distribution by varying the inlet turbulence boundary conditions to develop a separation bubble as predicted by *LINARS $k-\omega$ corr DLR* and *TRACE*.

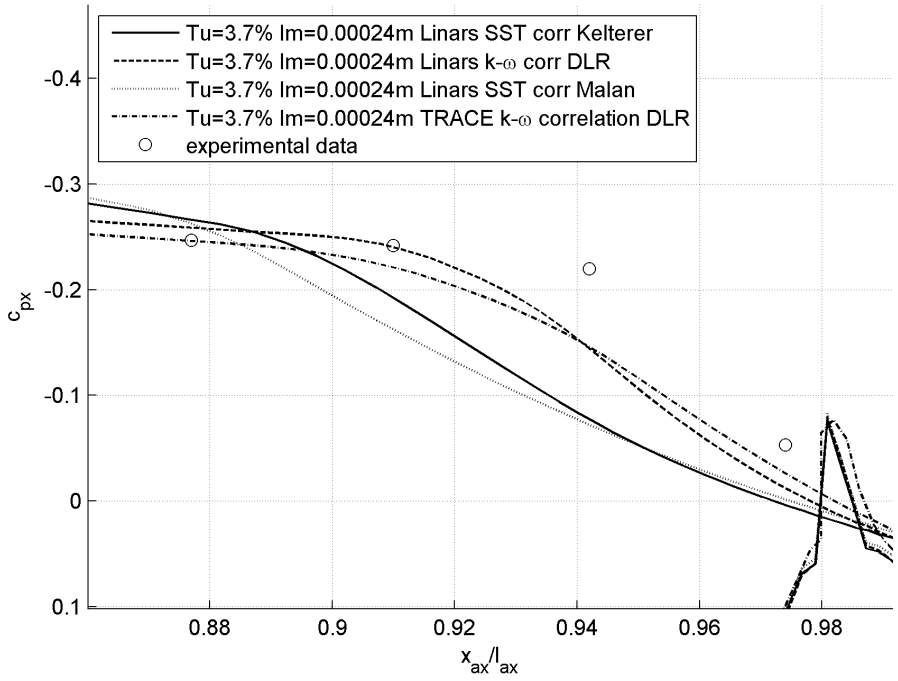

Figure 6.35: T160: Pressure coefficient comparison between different correlations for Re = 90000 (LINARS and TRACE) (zoomed)

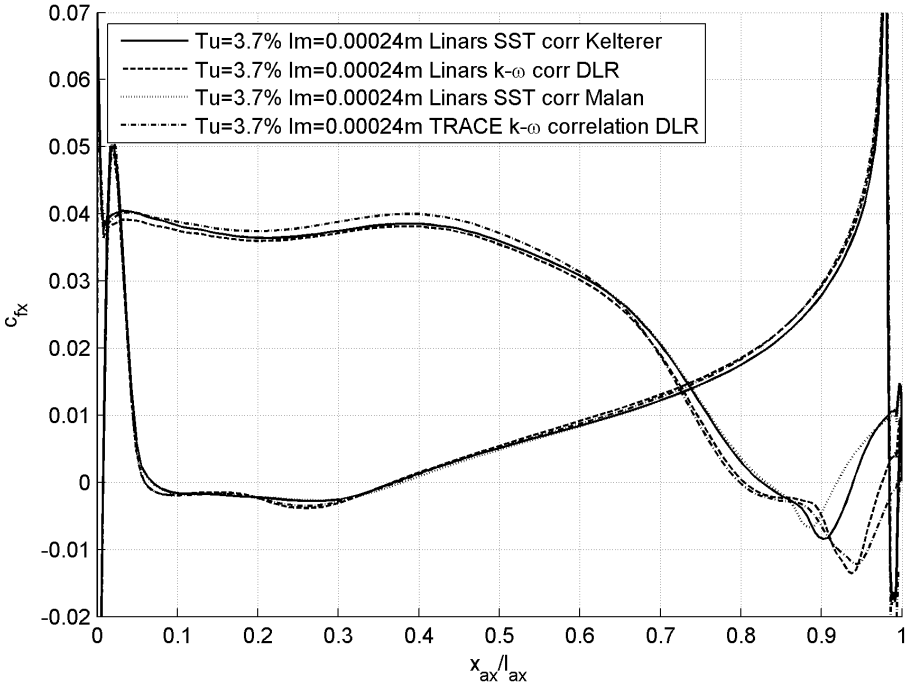

Figure 6.36: T160: Skin friction coefficient comparison between different correlations for Re = 90000 (LINARS and TRACE)

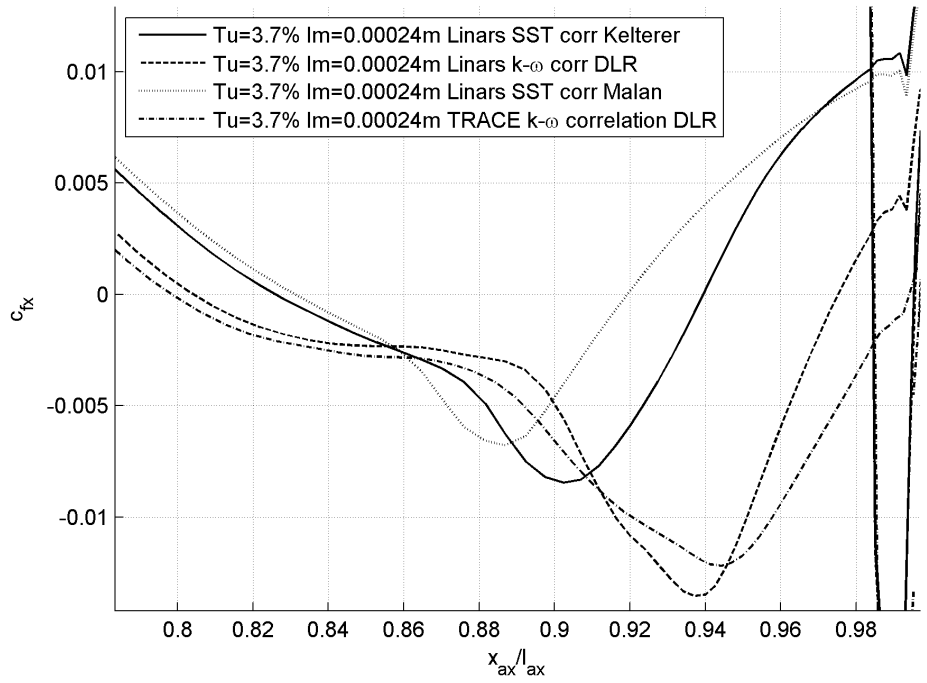

Figure 6.37: T160: Skin friction coefficient comparison between different correlations for Re = 90000 (LINARS and TRACE) (zoomed)

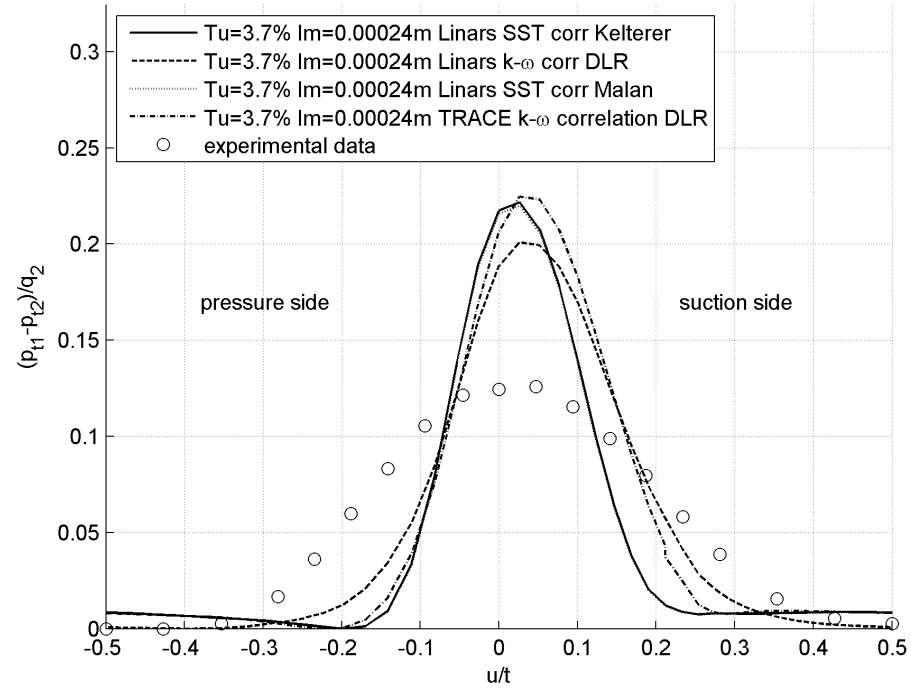

Figure 6.38: T160: Local pressure loss coefficient comparison between different correlations for Re = 90000 (LINARS and TRACE)

6.1.6 TRACE 3D

So far we have only considered 2D flows due to computational performance issues. As we experienced the TRACE code to be very fast (see section 6.1.8: Performance comparison of LINARS and TRACE), we wanted to test it on the 3D version of the T160 test case. The MTU kindly provided us with the grid (see figure 6.39). As for the 2D test case, the cross section expands in downstream direction.
The pressure coefficient and the skin friction coefficient were analyzed in three sections at 50%, 80% and 95% of the total blade height.

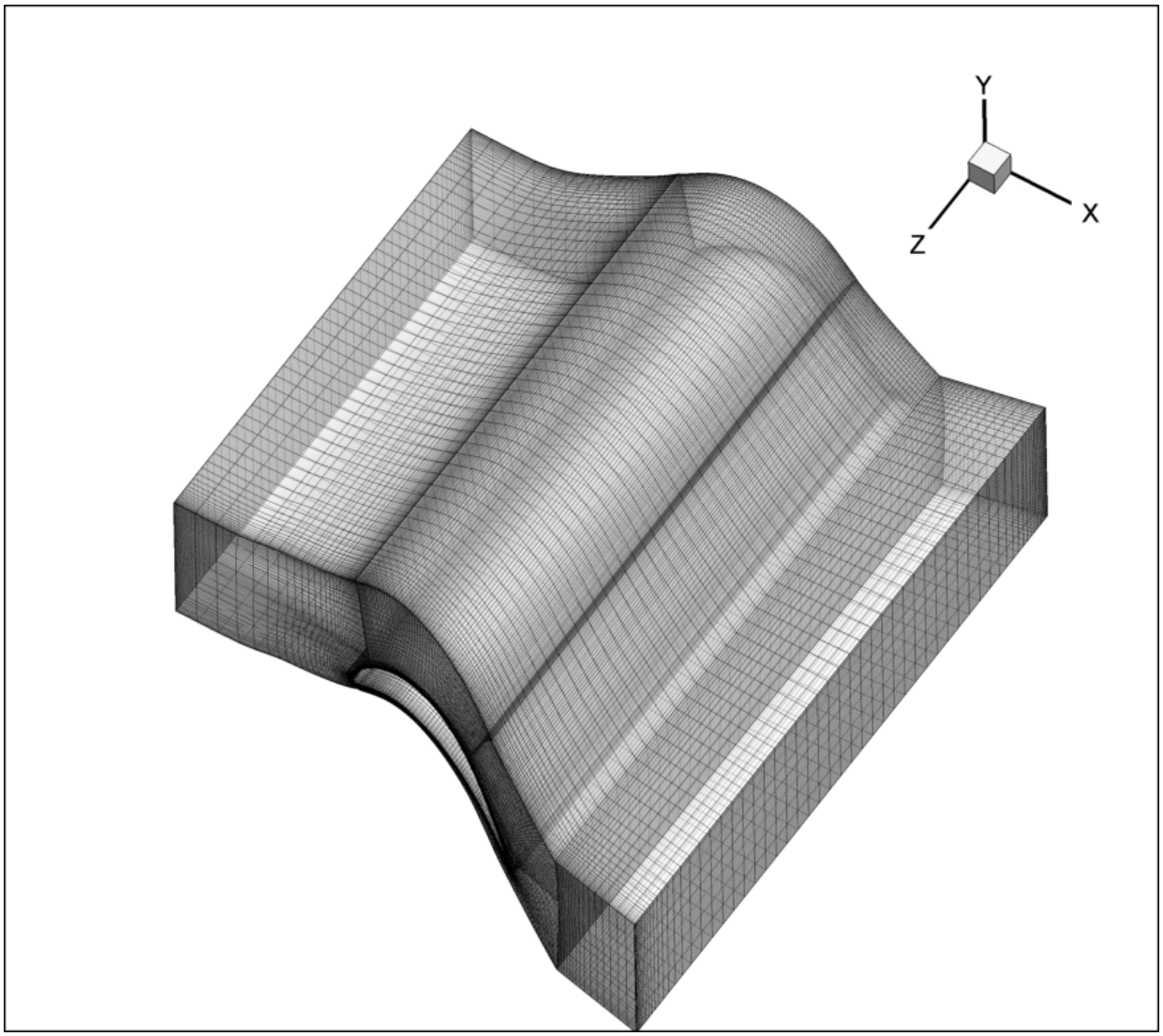

Figure 6.39: T160 3D grid by MTU

Figure 6.40 shows the pressure distribution. At 80% the pressure drop happens earlier, indicating a smaller separation bubble. Near the wall at 95% the pressure rises significantly on the suction side (notice the inverse ordinate). Figure 6.41 shows the skin friction coefficient. It can be seen that the location of transition moves upstream on the suction side as the flow comes closer to the wall. The wake depression is most distinct at 80% of the blade

height (see figure 6.42).

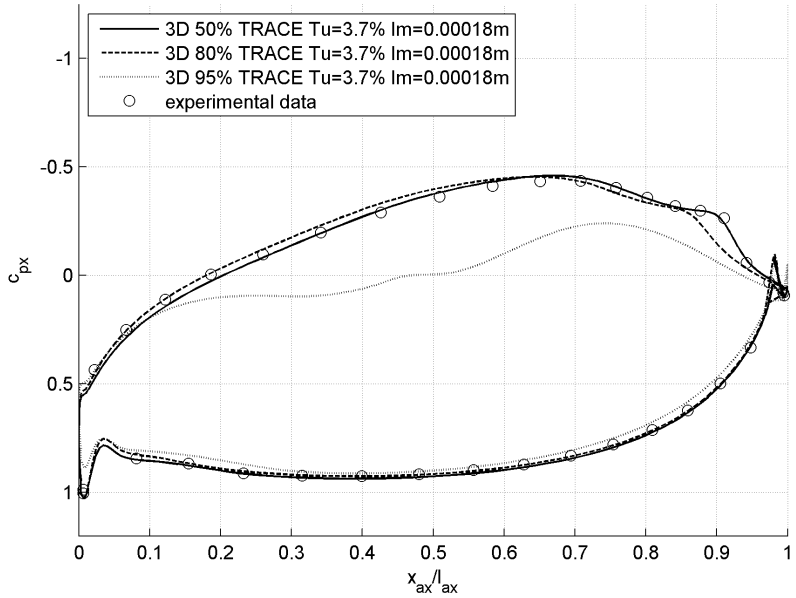

Figure 6.40: T160: Pressure coefficient (TRACE 3D)

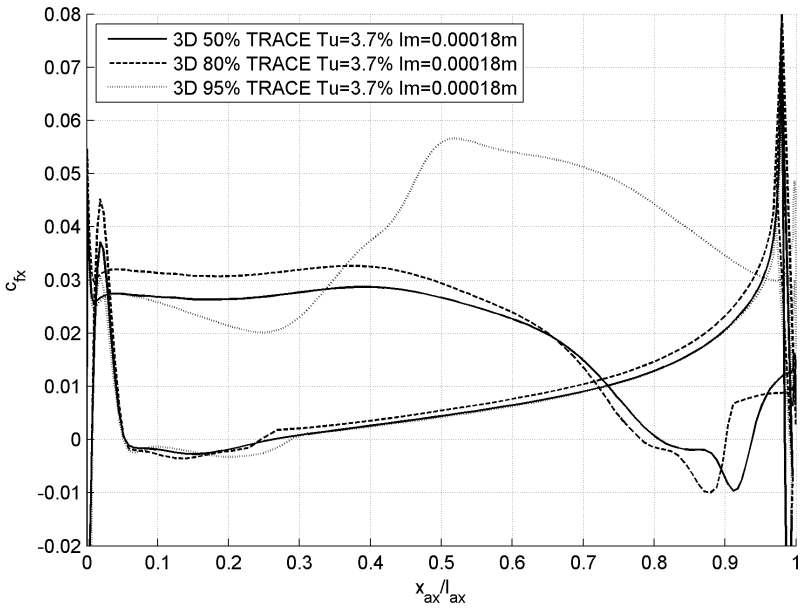

Figure 6.41: T160: Skin friction coefficient (TRACE 3D)

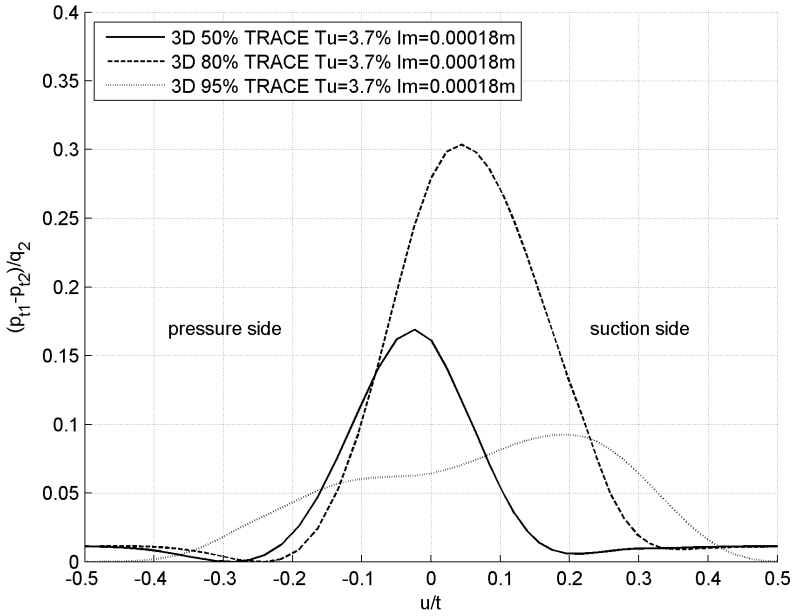

Figure 6.42: T160: Local pressure loss coefficient in measurement Layer ME0.4 (TRACE 3D)

6.1.7 T160 Summary

In the T160 test case, the Kelterer correlation predicted the location of transition too early. The results were barely affected by a change of the turbulent boundary conditions. The Malan correlation also predicted an early transition onset, but is more sensitive to changes of the turbulent boundary conditions. The best results were obtained from LINARS with DLR correlation and TRACE. As seen in the direct comparison, they produced similar results. As previously mentioned, both codes use the same correlations for the $\gamma - Re_\theta$ transition model. Still, this result is remarkable since the TRACE code produces different results for the flat plate test cases. The strength of TRACE lies in its computational efficiency.

6.1.8 Performance comparison of LINARS and TRACE

With this test case a performance comparison was carried out. For both codes, the time was taken to calculate 100 iterations. TRACE performed more than three times faster than LINARS, finishing after 46 seconds while LINARS takes 166 seconds. To discuss these results, the solver settings must be known (see table 6.8).

Solver settings	LINARS	TRACE
	implicit	implicit
Iteration Method	LGS	SSOR
Relaxation Parameter	0.5	0.7

Table 6.8: Solver settings in LINARS and TRACE

LINARS uses the Line Gauß-Seidel (LGS) iteration method, which is expected to take more

time for one iteration than the Symmetric Successive Over Relaxation (SSOR) iteration method. However, the advantage of the LGS method is that it normally takes less iterations until the simulation converges.
In order to compare the number of iterations of the codes to converge, some factors should be noted.
The criterion to consider a simulation as converged is fulfilled, if the residuals don't change anymore. It can be observed that the residuals level out at a value of one in LINARS and 10^{-6} in TRACE.
In LINARS and TRACE different initial values are used. The simulation started with LINARS with the Spalart-Allmaras turbulence model, where no initial values were used. The result was then used as the initial guess for the $k-\omega$ or SST turbulence model. This result was then used as the initial guess for the transition model. This procedure has to be followed in LINARS for stability reasons. In TRACE it is possible to initialize values at inlet and outlet. These values are interpolated over the flow field to obtain a good initial guess. In light of this it seems justified to compare the number of iterations of TRACE to the number of iterations of LINARS with the transition model, where also good initial values are used. Still LINARS needs roughly twice as many iterations to converge as TRACE. The reason for that is a stability problem in LINARS. For the T160 test case, it was not possible to set a higher CFL number than $CFL = 10$ due to stability issues. This led to a slow convergence. Figure 6.43 - 6.45 show the residuals of the LINARS calculation with Spalart-Allmaras turbulence model, $k-\omega$ turbulence model and transition model. Figure 6.46 shows the residuals of the TRACE calculation.

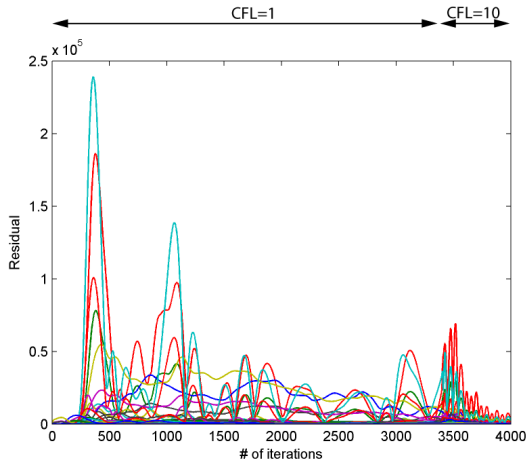

Figure 6.43: Residual of T160 test case with Spalart-Allmaras turbulence model (LINARS)

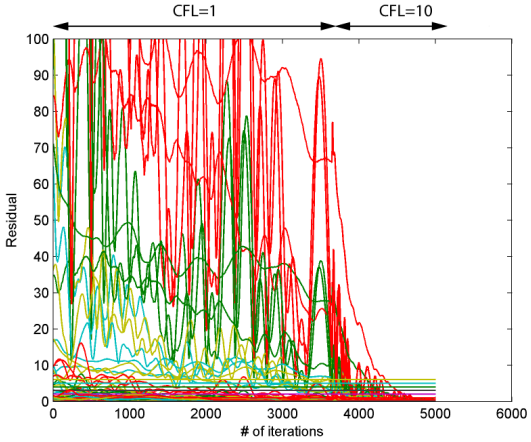

Figure 6.44: Residual of T160 test case with $k-\omega$ turbulence model (LINARS)

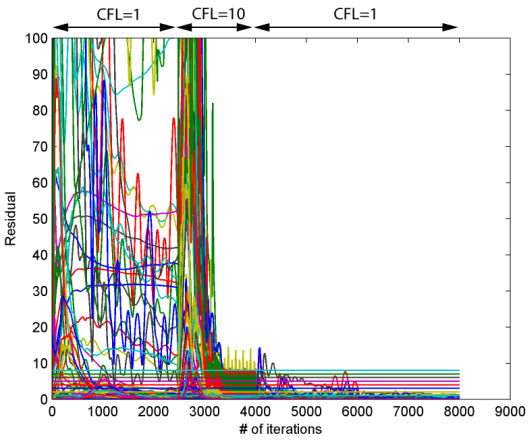

Figure 6.45: Residual of T160 test case with transition model, DLR correlation (LINARS)

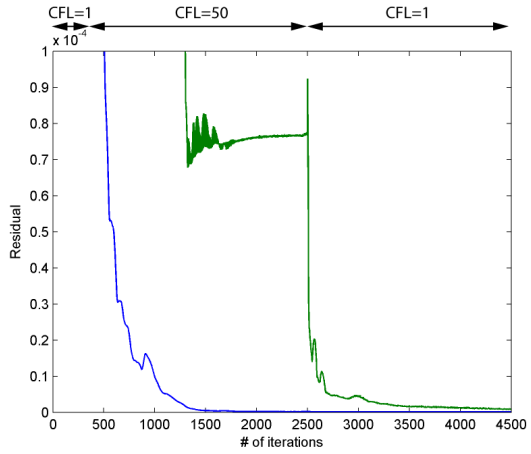

Figure 6.46: Residual of T160 test case with transition model (TRACE)

6.2 T106 Test Case

This test case is used to examine if the tendencies of the LINARS correlations from the T160 test case hold for another cascade test case.
The developer of this test case intended to produce a blade, where the transition occurs as late as possible to reduce losses. Experiments on this geometry were carried out by Hoheisel [1982] with various Reynolds numbers and various inlet turbulent properties. The reference states used in our simulations are given in table 6.9 and 6.10. The turbulent intensity at inlet is given by experimental data. The mixing length is set to a reasonable value.
The grid (see figure 6.47) was generated using the inhouse grid generator 2DAiGrid (Version February 2010). Figure 6.48 gives an overview of the design parameters of this geometry.

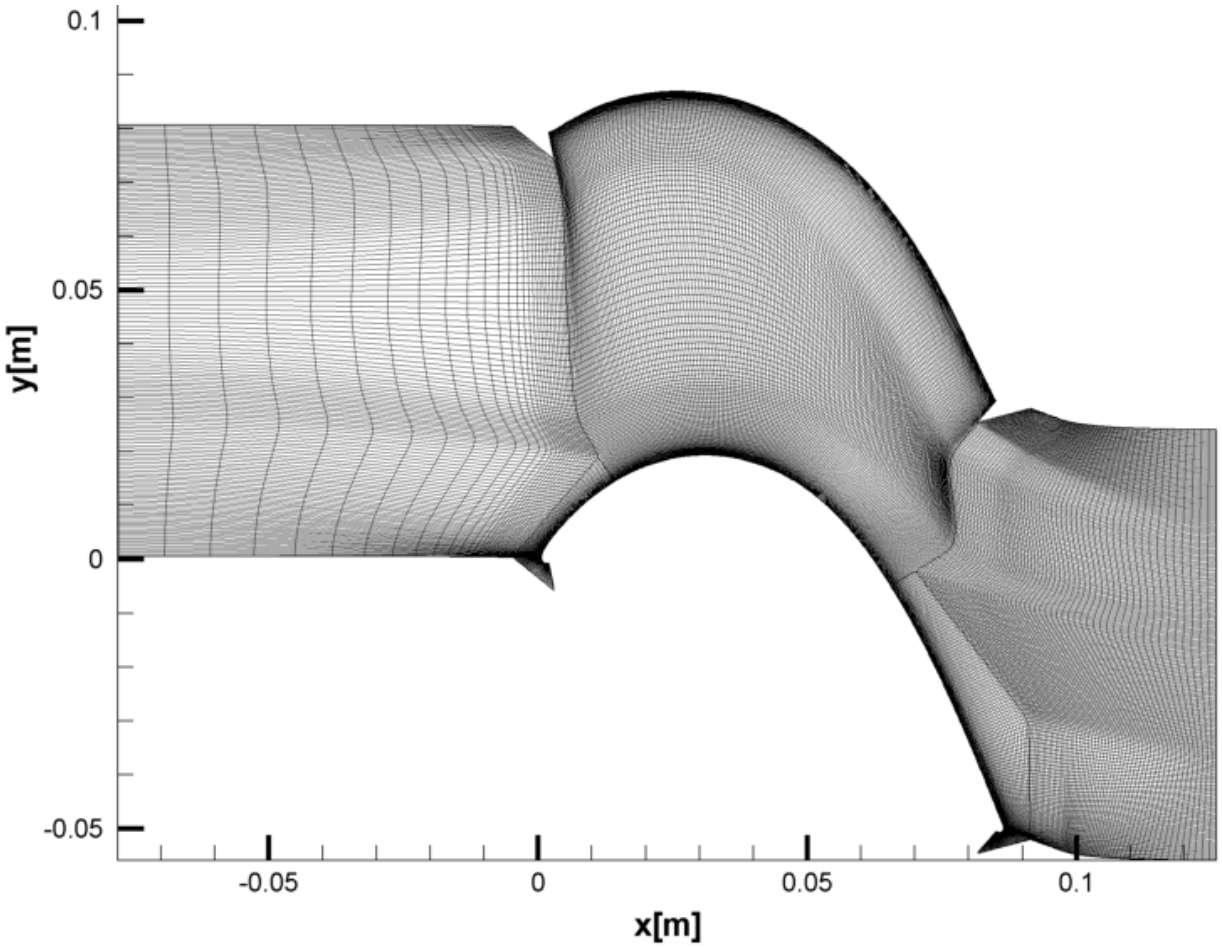

Figure 6.47: Grid of T106 test case

In this test case, the viscosity was calculated with the Sutherland law.
At a low Reynolds number ($Re_l = 150000$) the flow undergoes separation-induced transition. A long separation bubble develops, starting at about $x_{ax}/l_{ax} \approx 0.8$ till $x_{ax}/l_{ax} \approx 0.95$. As shown in the experiments (see 6.49), neither the onset of transition nor the length of the separation bubble changes appreciably with a variation of the inlet turbulence intensity.

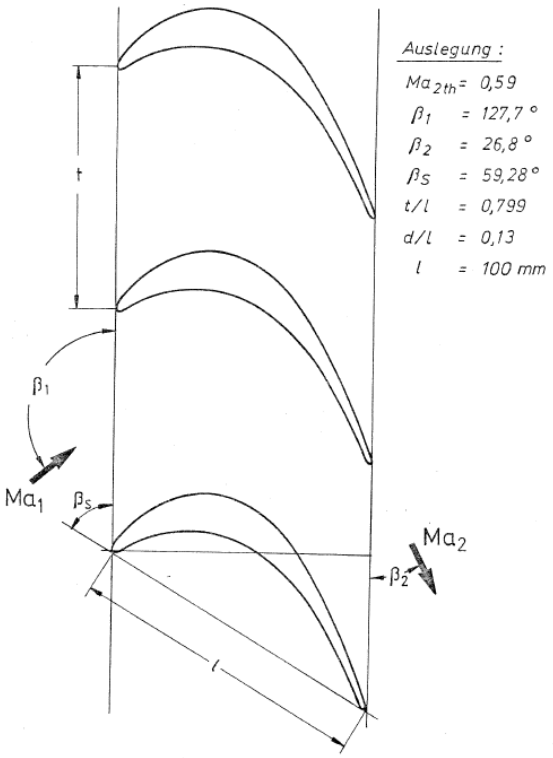

Figure 6.48: Geometry of T106 test case [Hoheisel, 1982]

T106 reference conditions	Re_l		
	150000	300000	500000
$p_{tot\ inlet}$	14405 Pa	28661 Pa	47583 Pa
p_2	11115 Pa	22116 Pa	36717 Pa
T_{tot}		313.25 K	

Table 6.9: Reference conditions of the T106 test case

Figure 6.49 shows the distribution of the pressure coefficient on the left hand side and the distribution of the skin friction coefficient on the right hand side at a low Reynolds number of $Re_l = 150000$. For $Tu = 0.5\%$, the Malan and DLR correlation predict a too early start of the separation bubble ($x_{ax}/l_{ax} \approx 0.7$) but capture the end well, thus the separation bubble is too long. The correlation by Kelterer shows a good agreement of the calculated pressure coefficient with the experimental data on the suction side till the start of the separation bubble. Then the pressure plateau is too short and the pressure drop happens too early, thus only a small separation bubble is predicted. When comparing the results from $Tu = 0.5\%$ to the results from $Tu = 4\%$ it can be seen that the correlations are very sensitive to the turbulent boundary conditions. For $Tu = 4\%$ the Kelterer correlation still predicts a small separation bubble. The flow undergoes bypass transition for the Malan correlation. The separation bubble predicted by the DLR correlation is still distinct.
Figure 6.50 shows the γ distribution in the region of transition near the wall at the grid line $j = 6$. Using the Kelterer correlation, production of turbulence starts up rapidly, shortly

Inlet turbulent boundary conditions								
Test (1)	T_u	=	0.5 %	l_m	=	0.002 m	2 %	chord length
Test (2)	T_u	=	4 %	l_m	=	0.002 m	2 %	chord length

Table 6.10: Turbulent boundary conditions of the T106 test case

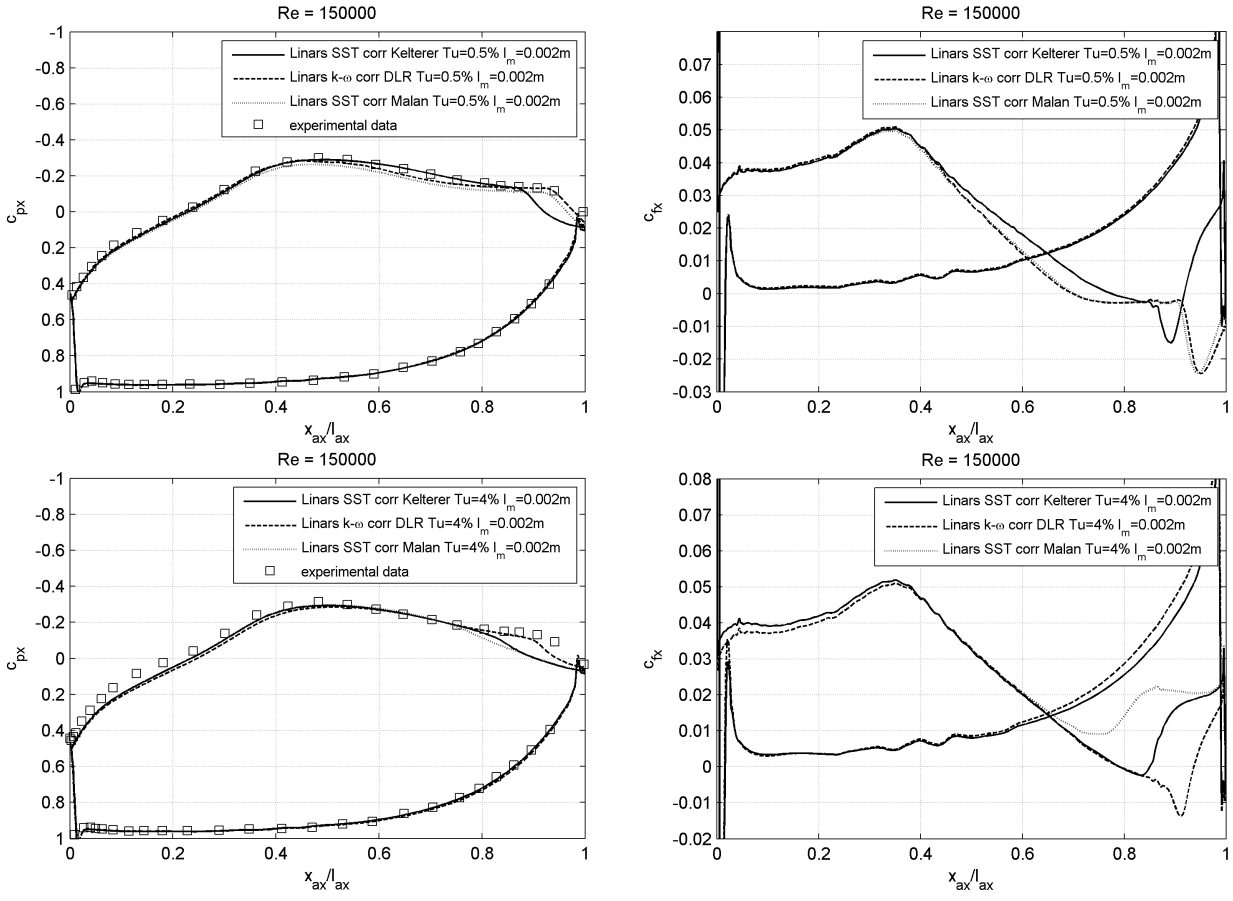

Figure 6.49: T106: Pressure coefficient (LHS) and skin friction coefficient (RHS) comparison between different correlations for $Re_l = 150000$ (LINARS)

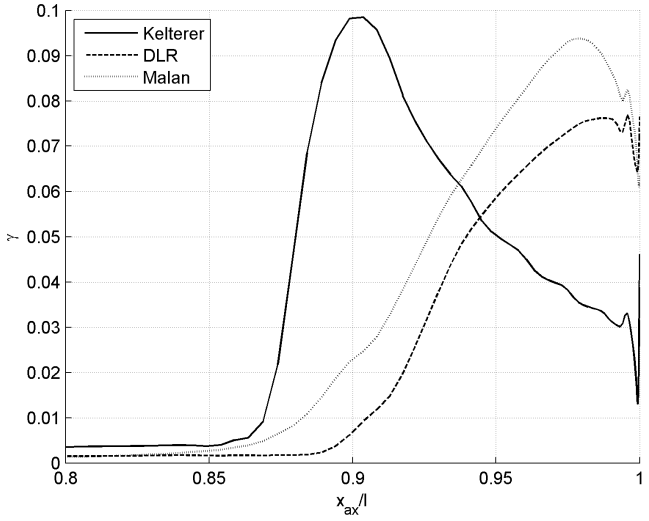

Figure 6.50: γ distribution of different codes near wall at region of transition, $Re_l = 150000$, $Tu = 0.5\%$

after the laminar boundary layer separates. At $x_{ax}/l = 0.9$ the intermittency reaches its peak, which is also the point where turbulent reattachment occurs. So the reason for the short separation bubble predicted by the Kelterer correlation is the sharp increase of γ. As visualized in figure 3.10, $Re_{\theta c}$ is limited to a value of 200 by the Kelterer correlation. $Re_{\theta cmax}$ is reached already at $\tilde{Re}_{\theta t} \approx 230$ leading to a early and rapid transition onset. The transition momentum Reynolds number in the zone of transition is very high with $Re_{\theta t} = 800 \div 1000$, so that we are in a region, where Kelterer correlation differs significantly from the DLR and Malan correlations. In this region, the F_{length} correlation also differs from the other correlations by a factor of 10.

Figures 6.51 and 6.52 show the pressure coefficient (left hand side) and skin friction coefficient (right hand side) for higher Reynolds numbers $Re_l = 300000$ and $Re_l = 500000$ respectively. The correlations are very sensitive to the inlet turbulence intensity. For a low turbulence intensity $Tu = 0.5\%$ the separation bubble produced by the Malan and DLR correlation is too long, while the the flow with the Kelterer correlation undergoes bypass transition. At a higher turbulence intensity all three correlations predict bypass transition. Here it turns out that the Malan correlation is more sensitive to the inlet turbulence intensity than the DLR correlation. All in all, the DLR correlation coupled with the $k - \omega$ turbulence model performed best with this test case.

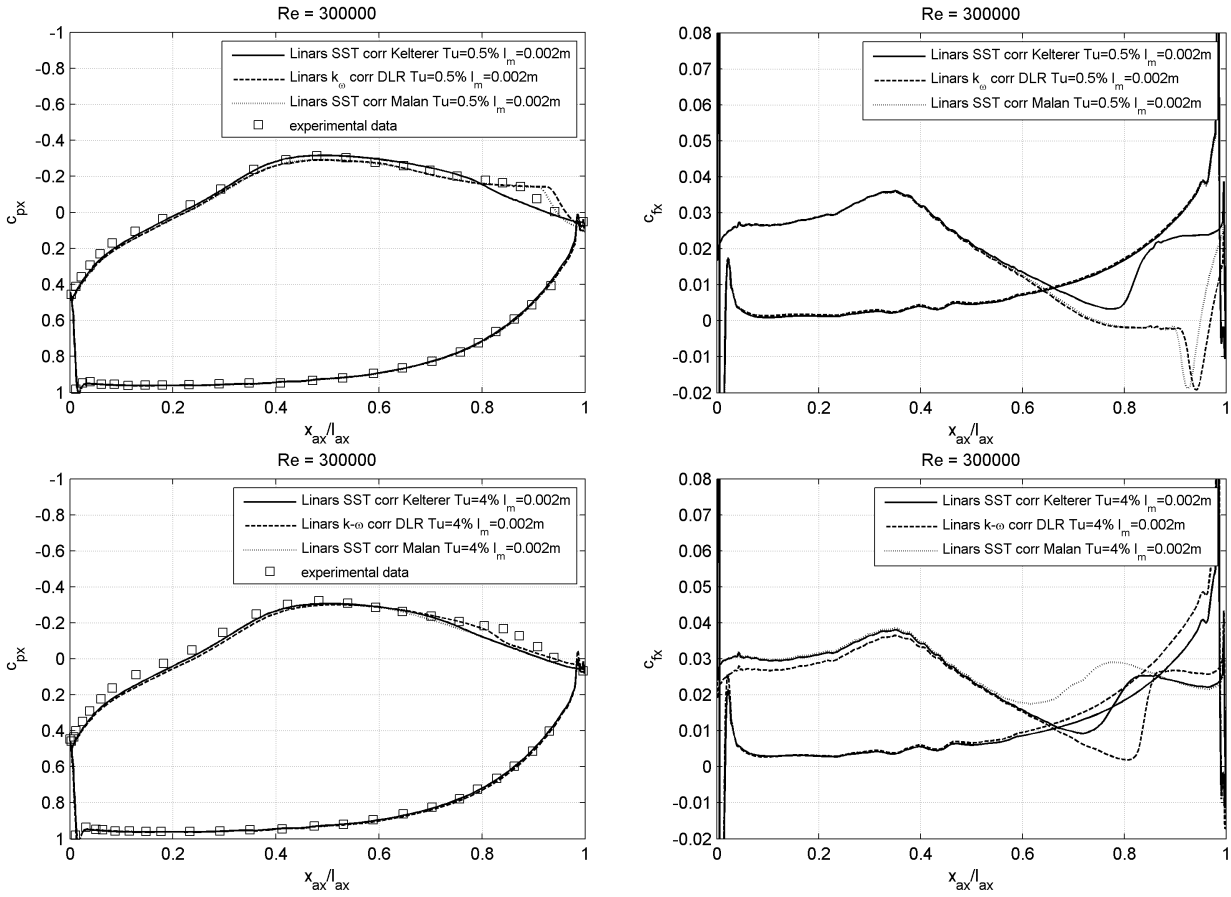

Figure 6.51: T106: Pressure coefficient (LHS) and skin friction coefficient (RHS) comparison between different correlations for $Re_l = 300000$ (LINARS)

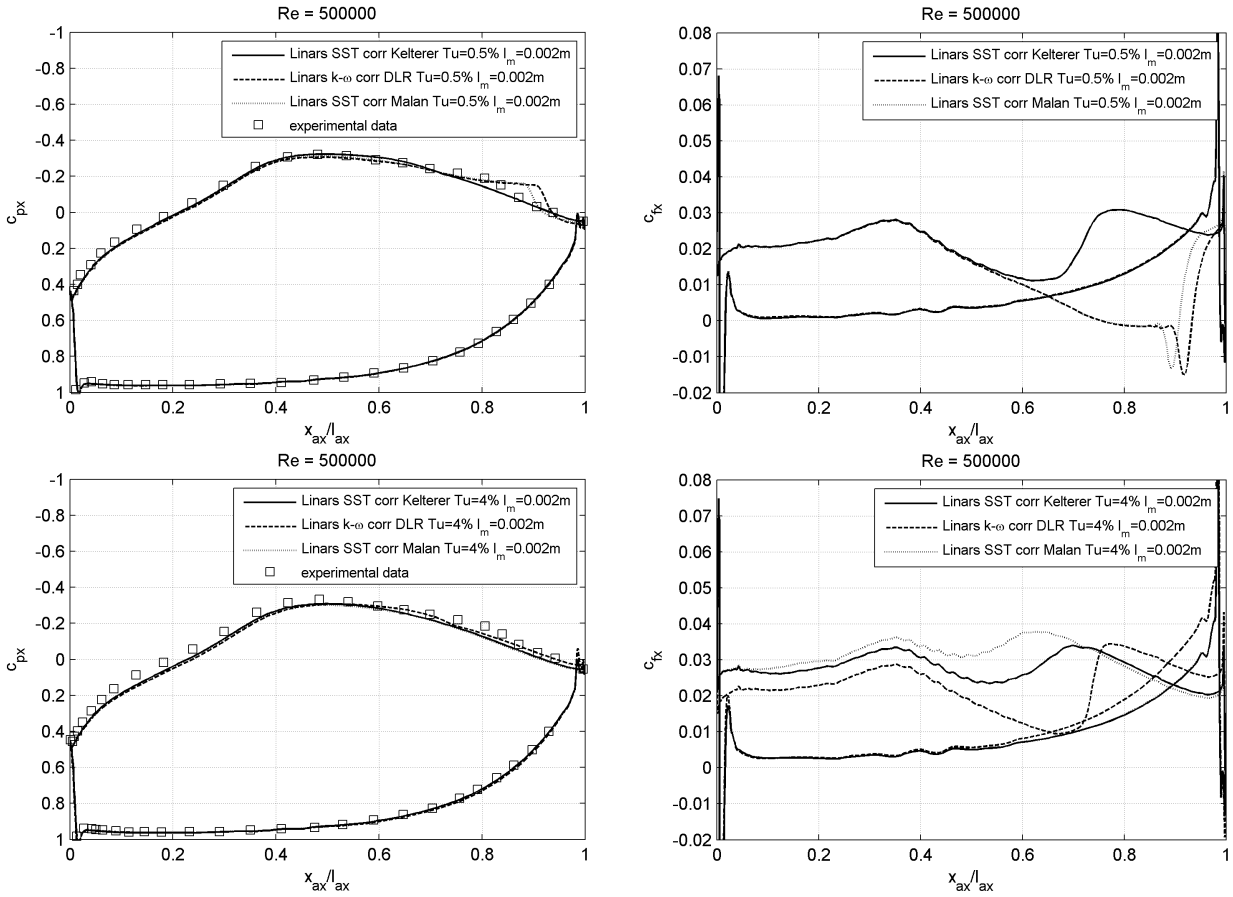

Figure 6.52: T106: Pressure coefficient (LHS) and skin friction coefficient (RHS) comparison between different correlations for $Re_l = 500000$ (LINARS)

6.2.1 T106 Summary

In this test case, too, the DLR correlation coupled with the Wilcox $k-\omega$ turbulence model performed best. The Kelterer correlation predicts a too early onset of transition and the Malan correlation is very sensitive to the turbulent boundary conditions and gave a too early onset of transition at higher inlet turbulence levels. The tendencies of the correlations also hold true for this test case.

7 Summary and Perspectives

In this work a brief introduction to turbulence and transition modelling is given at first. While details of the model formulations can be found in literature, this work points out that three empiric correlations are needed to close the $\gamma - Re_\theta$ transition model. Correlations found by Menter et al. [2004], Malan et al. [2009] and Kelterer et al. [2010] are tested against each other. The CFD codes LINARS (inhouse CFD code of the Institute for Thermal Turbomachinery and Machine Dynamics of Graz University of Technology) and TRACE (CFD code developed by the DLR in cooperation with MTU) are used to carry out the tests.

The main part of this work was to evaluate the results which were obtained by the LINARS and TRACE code. Five test cases, three flat plate (T3A, T3C2, T3C4) and two cascade test cases (T160, T106) were used to validate the different models. While no code is capable of predicting the mode, location and length of transition sufficiently over a wide range of test cases, the codes have their strengths and weaknesses for specific kind of flow problems. The TRACE code gave insufficient results for any flat plate test case, but showed its strengths in the T160 cascade test case, where it corresponds perfectly to the experimental data. This may be a consequence of its usage in industry and at universities for turbine simulations and therefore is tuned for such cases. Also the TRACE code outperforms the LINARS code in terms of computational efficiency as it calculates a given number of iterations up to three times faster than the LINARS code on a single CPU core and only requires approximately half as many iterations to converge. Its ability to run a simulation parallel on multiple cores makes it suitable for 3D and even unsteady simulations.

The LINARS inhouse code on the other hand is very flexible due to its ability to implement various correlations for the transition model and link it to different turbulence models. For the T3A flat plate test, all three correlations (Kelterer correlation, DLR correlation, Malan correlation) produced good results. The Kelterer correlation tends to start the transitional process slightly too far upstream. Generally, we observed that the correlations coupled with the Wilcox $k - \omega$ model produced a shorter transition zone than those coupled with the SST Model.

The Kelterer correlation produces the best results for the T3C2 and T3C4 flat plate test cases where the flow undergoes bypass transition or where the flow undergoes a separation induced transition where only a small separation bubble is developed. This may be due to the tendency of the Kelterer correlation to rapidly start up the production of turbu-

lence shortly after the laminar boundary layer separates and therefore never shows a long separation bubble.
The Malan and DLR correlations produce very similar results for a wide range of test cases. Unlike the Kelterer correlation, they were able to predict a long separation bubble for the T106 test case at low turbulence intensities. For high Reynolds numbers and low inlet turbulence intensities the Malan and DLR correlation both predict a too long separation bubble. It turns out that the Malan correlation is more sensitive to turbulent boundary conditions than the DLR correlation, predicting an even earlier location of transition onset for high turbulence intensities and small mixing lengths than the Kelterer correlation does. As the Malan and DLR correlations use the same correlations for $Re_{\theta c}$ and F_{length} the sensitivity of the Malan correlation to the turbulent boundary conditions might be due to variations in the $Re_{\theta t}$ formulation or the coupling to different turbulence models, as the Malan correlation is intended to be linked to the SST and the DLR correlation linked to the Wilcox $k-\omega$ model.

As stated by Menter et al. [2004] and Langtry and Menter [2009] the $\gamma - Re_\theta$ transition model gives only a framework of how a transition model can be implemented into a modern CFD environment, where only local variables are used. However, as shown in this work, the correlations available yet to close the model are not suitable for a wide range of applications and do not fully utilize the potential of the $\gamma - Re_\theta$ transition model. Also, one must be careful when implementing correlations to the own CFD code. As pointed out by Kelterer et al. [2010], the correlations are influenced by the code which was used to find the correlations and, therefore, there might be a need of adapting a correlation when it is implemented into another code. Future work will be dedicated to refining the correlations of $Re_{\theta t}$, $Re_{\theta c}$, and F_{length} by considering more test cases.

Bibliography

Abu-Ghannam, B. J. and Shaw, R. [1980], 'Natural Transition of Boundary Layer the Effect of Turbulent Pressure Gradient and Flow History', *Journal of Mechanical Engineering Science* **22**.

Dhawan, S. and Narasimha, R. [1958], 'Some Properties of Boundary Layer Flow During Transition from Laminar to Turbulent Motion', *Journal of Fluids Engineering* **3**.

Emmons, R. [1951], 'The Laminar-Turbulent Transition in Boundary Layer-Part I', *Journal of the Aeronautical Sciences* **18**.

Ferziger, J. H. and Peric, M. [2001], *Computational Methods for Fluid Dynamics*, 3rd edn, Springer.

Hoheisel, H. [1982], 'Entwicklung neuer Entwurfskonzepte für zwei Turbinengitter, Teil III, Ergebnisse T106', Institut für Entwicklungsdynamik, Braunschweig.

Kelterer, M., Pecnik, R. and Sanz, W. [2010], Computation of Laminar-Turbulent Transition in Turbomachinery using the Correlation based $\gamma - Re_\theta$ Transition Model, *in* 'ASME Turbo Expo 2009: Power for Land, Sea and Air GT2010 June 14-18, 2010, Glasgow, Scotland, GT2010-22207'.

Klebanoff, P. S. [1955], 'Characteristics of Turbulence in Boundary Layer with Zero Pressure Gradient', *NACA Technical Report* **1247**.

Langtry, R. and Menter, F. [2009], 'Correlation-Based Transition Modeling for Unstructured Parallelized Computational Fluid Dynamics Codes', *AIAA journal* **47**, 12.

Malan, P., Suluksna, K. and Juntasaro, E. [2009], Calibrating the γ-re transition model for commercial cfd, *in* '47th AIAA Aerospace Sciences Meeting including The New Horizons Forum and Aerospace Exposition'.

Marciniak, V., Kügeler, E. and Franke, M. [2010], Predicting Transition on low-Pressure Turbine Profiles, *in* 'V European Conference on Computational Fluid Dynamics ECCOMAS CFD 2010', Lisbon, Portugal.

Mayle, R. E. [1991], 'The 1991 IGTI Scholar Lecture: The Role of Laminar-Turbulent Transition in Gas Turbine Engines', *Journal of Turbomachinery* **113**(4), 509–536.

Menter, F. R., Langtry, R. B., Likki, S. R., Suzen, Y. B., Huang, P. G. and Völker, S. [2004], 'A correlation-based transition model using local variables: Part i model formulation', *ASME Conference Proceedings* **2004**(41693), 57–67.

Pecnik, R. [2007], Transition Modelling in Thermal Turbomachinery, PhD thesis, Graz Unversity of Technology.

Schlichting, H. and Gersten, K. [2000], *Boundary-Layer Theory*, 8th edn, Springer.

Schook, R., Steenhoven, A. and Dongen, M. [2000], Bypass Transition Experiments in Subsonic Boundary Layers, PhD thesis, Technische Universiteit Eindhoven.

Staudacher, W. and Homeier, L. [2003], 'Untersuchungen am Turbinengitter T160 zur Bestimmung der Gittercharakteristik bei homogener stationärer und periodisch instationärer Zuströmung und Anfertigen von Ölanstrichbildern', Universität der Bundeswehr München.

Steelant, J. and Dick, E. [1996], 'Modelling of Bypass Transition with Conditioned Navier-Stokes Equations coupled to an Intermittency Equation', *International Journal for Numerical Methods in Fluids* **23**.

Versteeg, H. and Malalasekra, W. [2007], *An Introduction to Computational Fluid Dynamics: The Finite Volume Method (2nd Edition)*, 2 edn, Prentice Hall.

White, F. M. [2007], *Fluid Mechanics (6th International Edition)*, McGraw-Hill.

Wilcox, D. [2006], *Turbulence modeling for CFD*, DCW industries La Canada, CA.